LBL-8105
c. 2

MOLYBDENUM-SUBSTRATE INTERACTIONS IN NITROGENASE: AN EXAFS STUDY

Joseph Patrick Smith
(Ph.D thesis)

July 1978

Prepared for the U. S. Department of Energy
under Contract W-7405-ENG-48

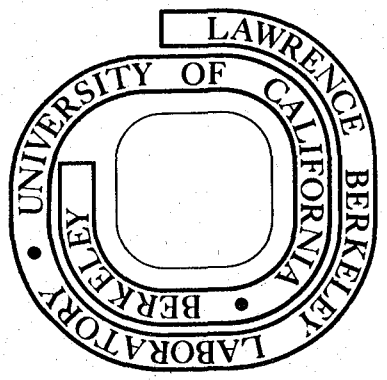

LBL-8105

MOLYBDENUM-SUBSTRATE INTERACTIONS IN NITROGENASE: AN EXAFS STUDY

Joseph Patrick Smith

Lawrence Berkeley Laboratory
University of California
Berkeley, California 94720

This work was done with support from the
U. S. Department of Energy.

Molybdenum-Substrate Interactions in Nitrogenase: An EXAFS Study

Joseph Patrick Smith

B.S. (University of Rochester) 1972

Abstract

The sensitivity of x-ray absorption edge spectra and extended x-ray absorption fine structure (EXAFS) to the environment of metal atoms make x-ray absorption spectroscopy a useful probe of the environment of the molybdenum in nitrogenase. It is of particular interest to investigate any perturbations of the environment of the molybdenum due to the presence of nitrogenase substrates. The molybdenum K-edge x-ray absorption spectra of solution samples of the molybdenum-iron component of nitrogenase equilibrated with argon or dinitrogen as the gas phase have been examined. A comparison of the absorption edge spectra and EXAFS of the enzyme samples failed to show any changes due to the presence of dinitrogen. This suggests that, under the conditions of this measurement, dinitrogen does not cause any significant perturbation of the coordination environment of the molybdenum in nitrogenase. The presently available EXAFS data are not sufficiently precise to completely rule out the possibility that nitrogen is entering the coordination environment of molybdenum in nitrogenase. Analysis of nitrogenase EXAFS data by Fourier transformation and curve fitting showed substantial agreement with the model for the molybdenum site proposed by Cramer, Hodgson and co-workers (J. Am. Chem. Soc.(1978)100, 3398 - 3407).

The absorption edge spectra of sodium molybdate dihydrate, potassium hexachloromolybdate, molybdenum dioxide, molybdenum trioxide and tris(3,4 dithiotoluene)Mo(VI) are discussed in terms of the metal

site symmetry and molecular orbital energy levels. The Fourier transforms of the EXAFS of these molybdenum compounds, as well as those of iron and molybdenum metal foils are presented and discussed. The effects of the choice of the reference energy and the k - space domain on the results of the Fourier transform technique are discussed.

X-ray absorption measurements were made with a two ionization chamber detector system. The dependence of the precision of absorption measurements on the sample absorbance, ion chamber absorbances and x-ray photon flux is shown explicitly. The effect of sample composition on the signal-to-noise ratio of absorbance and fluorescence measurements is discussed. Experimental measurements and numerical modeling of detector performance indicate that the precision of measurements of x-ray absorption with the two ionization chamber system approaches the limit imposed by photon counting statistics. The results of measurements of the x-ray absorption spectra of nitrogenase samples by the absorption and fluorescence detection techniques are compared.

The procedures used for the growth of Azotobacter vinelandii for the production of nitrogenase are discussed in detail. The procedures used for the purification of nitrogenase according to the method of Shah and Brill (Biochem. Biophys. Acta(1973)305, 445 - 454) are described in detail.

M. Cohen

CONTENTS

Acknowledgements

The support and encouragement of Professor Melvin Calvin are gratefully acknowledged. For originally kindling my interest in nitrogen fixation and for continued encouragement during the course of this work, I sincerely thank Dr. Melvin P. Klein.

Duane Yoch, Hisao Yokata and David Busch provided assistance and advice during the startup of the preparative work. An invaluable demonstration of nitrogenase purification techniques and several helpful discussions were provided by Vinod Shah and Winston Brill, and I thank them for their assistance. During the early stages of the x-ray absorption work, nitrogenase samples were generously provided by Michael Henzl.

The x-ray absorption data could not have been collected or analyzed without the help of Alan Robertson, Jon Kirby and Al Thompson. I also thank them for many helpful discussions concerning the analysis of the x-ray absorption data. Timothy Walker contributed data on the molybdenum dinitrogen complex. Keith Hodgson generously provided model compound data, computer facilties and assistance during the curve fitting analysis of the nitrogenase EXAFS data.

To DeChantal Barrett, I am sincerely grateful for her years of devoted care, guidance and constant encouragement. The patience and encouragement of Jean Ruggles during the preparation of this thesis are gratefully and sincerely acknowledged.

This work was supported in part by the Division of Biological and Environmental Research of the Department of Energy. Synchrotron radiation facilties were provided by the Stanford Synchrotron Radiation Laboratory which is supported by NSF grant DMR-07692-A02.

Chapter I

Introduction

Certain microorganisms are able to reduce atmospheric dinitrogen (N_2) into ammonia in a process known as nitrogen fixation. Catalyzed by the enzyme nitrogenase, nitrogen fixation provides a pool of ammonia which can be used for the synthesis of biochemically vital nitrogen containing compounds.

Biological nitrogen fixation is responsible for 72 % of the fixed nitrogen input to the agricultural soils of the earth.[1] It therefore plays a central role in the global nitrogen cycle. The dependence of the Haber process for the production of ammonia on increasingly scarce fossil fuels[2] for energy and raw materials has generated increased interest in the understanding and manipulation of biological sources of fixed nitrogen.

Apart from its practical importance, biological nitrogen fixation is of interest from a chemical standpoint. The facile reduction of normally unreactive dinitrogen at room temperature and in aqueous media is remarkable when considered in the light of the severe conditions (500^{o}C, 200 atm) used in the Haber process.

In this introductory chapter, we will discuss the basic properties and enzymology of nitrogenase. This discussion will provide a basis for

understanding the results presented in later chapters. A brief discussion of the function of molybdenum in nitrogenase will be presented, followed by some comments on the application of x-ray absorption spectroscopy to the study of molybdenum in nitrogenase. This introduction, along with the other chapters of this thesis, will have separately numbered figures and references.

A. Nitrogenase

Nitrogenase is composed of two iron-sulfur proteins. The larger of the two contains 1-2 molybdenum atoms, approximately 33 iron and 26 acid labile sulfur atoms per 220,000 daltons molecular weight. It is known as component I or the Mo-Fe component. The smaller protein, known as the Fe component or component II, contains 4 iron and 4 acid labile sulfur atoms per 60,000 daltons molecular weight. Both proteins must be present for the catalysis of any of the reactions associated with nitrogenase.

In addition to dinitrogen, a variety of substrates with triple bonds are reduced by nitrogenase (fig. 1). All of these reductions are inhibited by carbon monoxide. The reduction of H^+ to H_2 (known as ATP dependent hydrogen evolution) competes for electron flow with the reduction of triply bonded substrates. ATP dependent hydrogen evolution is not inhibited by carbon monoxide. The presence or absence of CO inhibition defines two mechanistically distinct classes of nitrogenase reductions.

In addition to both proteins; ATP, a divalent metal ion, and a suitable reductant are needed for substrate reduction. Depending on reaction conditions, four to five molecules of ATP are hydrolyzed to ADP for each pair of electrons transferred to substrates. Magnesium

is the divalent metal ion usually employed. For in vitro studies, sodium dithionite serves as the reductant. Several other agents have been shown to be effective reductants. In some cases, the presence of catalytic amounts of "electron carriers" is required to mediate the transfer of electrons from reductants to nitrogenase. Figure 2 illustrates the classes of nitrogenase reductions, the sources of reducing equivalents and the hydrolysis of ATP. We may summarize the stoichiometry for the reduction of dinitrogen catalyzed by nitrogenase using dithionite as the reductant by the following net reaction.

$$3S_2O_4^{-2} + 12ATP^{-4} + 16OH^- + N_2 + 2H_2O = 2NH_4^+ + 12ADP^{-3} + 12HPO_4^{-2} + 6SO_3^-$$

B. Function of Molybdenum in Nitrogenase

It has long been known that molybdenum is required for the growth of bacteria when dinitrogen is the sole source of nitrogen.[4] More recently, it has been found that molybdenum is always present in active nitrogenase preparations.[3] Studies of a molybdate cysteine complex[5] have shown that many nitrogenase-catalyzed reactions can also be catalyzed by systems containing molybdenum as the sole metallic element. These results suggest that molybdenum plays an important role in the enzyme mechanism.

Solvent extraction studies have shown that the molybdenum in nitrogenase is contained in a small fragment containing 8 iron atoms and 6 acid labile sulfur atoms for each molybdenum[3]. Known as the iron-molybdenum cofactor, this fragment is common to nitrogenase components isolated from a variety of organisms. It is apparently different from the molybdenum centers in enzymes such as xanthine oxidase and nitrate reductase.[6] Although the removal of the iron-molybdenum cofactor is not reversible, it has been shown that the remaining parts of the

molybdenum-iron component can be synthesized separately by certain mutant bacteria.[7] This finding indicates that the primary purpose of the molybdenum-iron cofactor is not merely to stabilize the gross protein structure of the molybdenum-iron component.

The dearth of knowledge about the molybdenum in nitrogenase is partly due to the inapplicability of the commonly available spectroscopic techniques to this problem. In many metalloprotein systems, a spectroscopic property specific to the metal-protein complex can be used as a probe of the metal's environment. In some cases, if the native metal can be replaced by another metal with retention of biological activity, a metal with properties more amenable to spectroscopic study may be substituted. These approaches have not been fruitful for the study of molybdenum in nitrogenase. It appears, for instance, that none of the features of the UV-VIS or EPR[8] spectra of nitrogenase can be attributed to the presence of molybdenum.

C. X-Ray Absorption Spectroscopy

Speculation about the function of molybdenum in nitrogenase has centered on its possible role as a substrate or inhibitor binding site or as a site for electron transfer.[9] An experiment to determine the oxidation state of molybdenum in the enzyme and to investigate any possible molybdenum-substrate interactions would help to define the role of molybdenum in nitrogenase. The use of x-ray absorption spectroscopy (XAS) with synchrotron radiation x-ray sources has provided useful information about the oxidation state and coordination environment of metal atoms in a variety of biological systems.[10,11,12] In the following paragraphs, we will discuss the potential applications of XAS to the study of the molybdenum in nitrogenase.

Figure 3 shows a typical x-ray absorption spectrum which, for the purpose of discussion, has been divided into two regions. The area in the vicinity of the sharp increase in x-ray absorption is the edge region. Structure in the edge region is due to the promotion of core electrons to unfilled, discrete molecular orbital final states. The edge structure depends in a complicated fashion on the metal's oxidation state, the identity of the surrounding ligands and the arrangement of the ligands around the metal atom.[11,13,14]

The region of the spectrum is the extended x-ray absorption fine structure(EXAFS). EXAFS, which extends up to 1 KeV above the absorption edge, consists of small modulations of the photoabsorption cross section of the element of interest. EXAFS modulations are a result of final state interference effects caused by backscattering of photoelectrons off atoms in the immediate vicinity of the absorber of interest.

Two types of information contained in EXAFS are of interest for the study of metals in biochemical systems. First, the periodicitities of EXAFS modulations are related to the distances between the absorbing atom and its surrounding ligands.[15] Second, the energy dependence of of EXAFS modulation amplitudes is characteristic of the atomic number of the scattering atoms as well as the thermal and structural disorder in the arrangement of scattering atoms around the absorber.[16]

The above discussion indicates that if x-ray absorption spectra could be fully interpreted, the information they contain could be useful for the study of metals in metal-enzyme complexes. For instance, the determination of the identity and spatial arrangement of the ligands around a metal atom in an enzyme is necessary if the function of the metal is to be fully understood. The solution of this problem

in enzyme systems is often complicated by the high molecular weight of the enzyme, the lack of crystals suitable for study by x-ray diffraction, the chemical lability of the protein or the spectroscopic reticence of the metal site of interest. XAS can provide information about the metal sites in proteins in spite of these difficulties.

The XAS technique has some unique advantages for the study of metals in biochemical systems. First, XAS is element specific. X-ray absorption edges of the various metals are separated by at least several hundred electron volts. As a result, the interpretation of EXAFS and absorption edge data for one metal cannot be confused by the presence of of another metallic element in the sample. Second, the absorption edge and EXAFS cannot be obscured by changes in the metal's oxidation state, the metal site symmetry or the coordination environment of the absorbing atom. Third, the technique is not restricted to the study of samples in the crystalline state. Finally, in the interpretation of EXAFS, only the local environment of the absorber, as oppposed to the entirety of the protein structure, as is the case with x-ray diffraction, need be considered.

D. X-Ray Absorption Spectroscopy Studies of Nitrogenase

In the case of nitrogenase, if the molybdenum functions as, or is closely associated with, the substrate binding site, it is reasonable to assume that the binding of substrate would cause some perturbation of the coordination environment of molybdenum. In principle, the study of the molybdenum x-ray absorption spectra of enzyme samples equilibrated with substrates or inert gases might reveal such perturbations. Analysis of XAS data could provide some information about the nature of the molybdenum site in nitrogenase and about molybdenum-substrate inter-

actions in that enzyme. In this thesis, the results of measurements of the molybdenum x-ray absorption spectra of samples of the molybdenum-iron component of nitrogenase equilibrated with dinitrogen or with inert gases as the gas phase are reported.

In addition to the spectra of nitrogenase samples, the x-ray absorption spectra of several compounds of known structure are presented. The results of studies of compounds of known structure serve to illustrate the type of information obtainable from the analysis of x-ray absorption spectra.

E. Organization of the Text

In chapter II of this thesis, studies of the absorption edge spectra of molybdenum compounds and nitrogenase samples are presented. EXAFS studies are discussed in chapter III. Experimental considerations pertinent to both edge and EXAFS studies are discussed in chapter IV. In chapter V, the results of a study of the factors which control the precision of measurements of x-ray absorption are presented.

The nitrogenase used in this work was isolated from Azotobacter vinelandii. Techniques used for the growth of Azotobacter for nitrogenase production are described in chapter VI. The techniques used for the preparation of nitrogenase according to the method of Shah and Brill[17] are described in detail in chapter VII. Techniques used for the assay of nitrogenase activity are described in chapter VIII.

References

1. R.W.F. Hardy; Proc. of the 1st International Symposium on Nitrogen Fixation, eds. W. Newton and C. Nyman, Wash. State Univ. Press, Pullman, Wash.(1975)2, 693- 717.

2. G.D. Sweeney; Proc. of the 1st International Symposium on Nitrogen Fixation, eds. W. Newton and C. Nyman, Wash. State. Univ. Press, Pullman, Wash.(1975)2, 648 - 655.

3. V.K. Shah and W.J. Brill; Proc. Nat'l. Acad. Sci.-USA(1977)74, 3249 - 3253.

4. D.H. Burk and R.H. Burris; Ann. Rev. Biochem.(1974)10, 587 - 630.

5. G.N. Schrauzer; Proc. of the 1st International Symposium on Nitrogen Fixation, eds. W. Newton and C. Nyman, Wash. State Univ. Press, Pullman, Wash,(1975)1, 79 - 116.

6. P.T. Pienkos, V.K. Shah and W.J. Brill; Proc. Nat'l. Acad. Sci. - USA(1977)74, 5486 - 5471.

7. H.H. Nagatani, V.K. Shah and W.J. Brill; J. Bact.(1974)120, 697 - 701.

8. G. Palmer, J. Multani, W. Cretney, W. Zumft and L. Mortenson; Arch. Biochem. Biophys.(1972)153, 325 - 332.

9. W. Newton, J. Corbin and J. McDonald; Proc. of the 1st International Symposium on Nitrogen Fixation, eds. W. Newton and C. Nyman, Wash. State Univ. Press, Pullman, Wash.(1975)1, 53 - 74.

10. V.W. Hu, S.I. Chan and G.S. Brown; Proc. Nat'l. Acad. Sci.-USA (1977)74, 3281 - 3285.

11. R.G. Shulman, Y. Yafet, P. Eisenberger and W.E. Blumberg; Proc. Nat'l. Acad. Sci. - USA(1976)73, 1384 - 1388.

12. R.G. Shulman, P. Eisenberger, W. Blumberg and N. Stombaugh; Proc. Nat'l. Acad. Sci. - USA(1975)72, 4003 - 4007.

13. U.C. Srivastava and H.L. Nigam; Coord. Chem. Rev.(1972 - 1973)9, 275 - 310.

14. S.P. Cramer, T.K. Eccles, F.M. Kutzler, K.O. Hodgson and L.E. Mortenson; J. Am. Chem. Soc.(1976)98, 1287 - 1288.

15. F.W. Lytle, D.E. Sayers and E.A. Stern; Phys. Rev. B(1975)11, 4825 - 4835.

16. B.K. Teo, P.A. Lee, A.L. Simons, P. Eisenberger and B.M. Kincaid; J. Am. Chem. Soc.(1977)99, 3854 - 3856.

References

17. V.K. Shah and W.J. Brill; Biochem. Biophys. Acta(1973)305, 445 - 454.

Figure Captions

1. A list of nitrogenase catalyzed reductions of small molecules with triple bond character. All of these reductions are inhibited by carbon monoxide.
2. Schematic diagram for nitrogenase reductions, showing sources of reducing equivalents, electron carriers, ATP hydrolysis, ATP dependent hydrogen evolution and reduction of triply bonded substrates.
3. X-ray absorption spectrum of solid $Na_2MoO_4 \cdot 2H_2O$. The ratio of the incident intensity (I_0) to transmitted intensity (I) is plotted on the ordinate axis. The absorbance (μx) is the natural logarithm of this ratio. In the edge region, transitions to discrete final states are labeled as 1s-4d, 1s-5s and 1s-5p, using metal atomic orbital designations. A more satisfactory explanation of structure in the edge region, based on a molecular orbital scheme, is discussed in chapter II.

NITROGENASE REDUCTIONS

$$N_2 \xrightarrow{6e} 2\,NH_3$$

$$N_3^- \xrightarrow{2e} N_2 + NH_3$$

$$N_2O \xrightarrow{2e} N_2 + H_2O$$

$$C_2H_2 \xrightarrow{2e} C_2H_4$$

$$CH_3NC \xrightarrow{6,8,10,12,14\,e} CH_4 + CH_3NH_2 + C_2H_4 + C_2H_6 + C_3H_6 + C_3H_8 + NH_3$$

$$HCN \xrightarrow{6,4\,e} CH_4 + NH_3 + CH_3NH_2$$

XBL745-5153

Figure 1

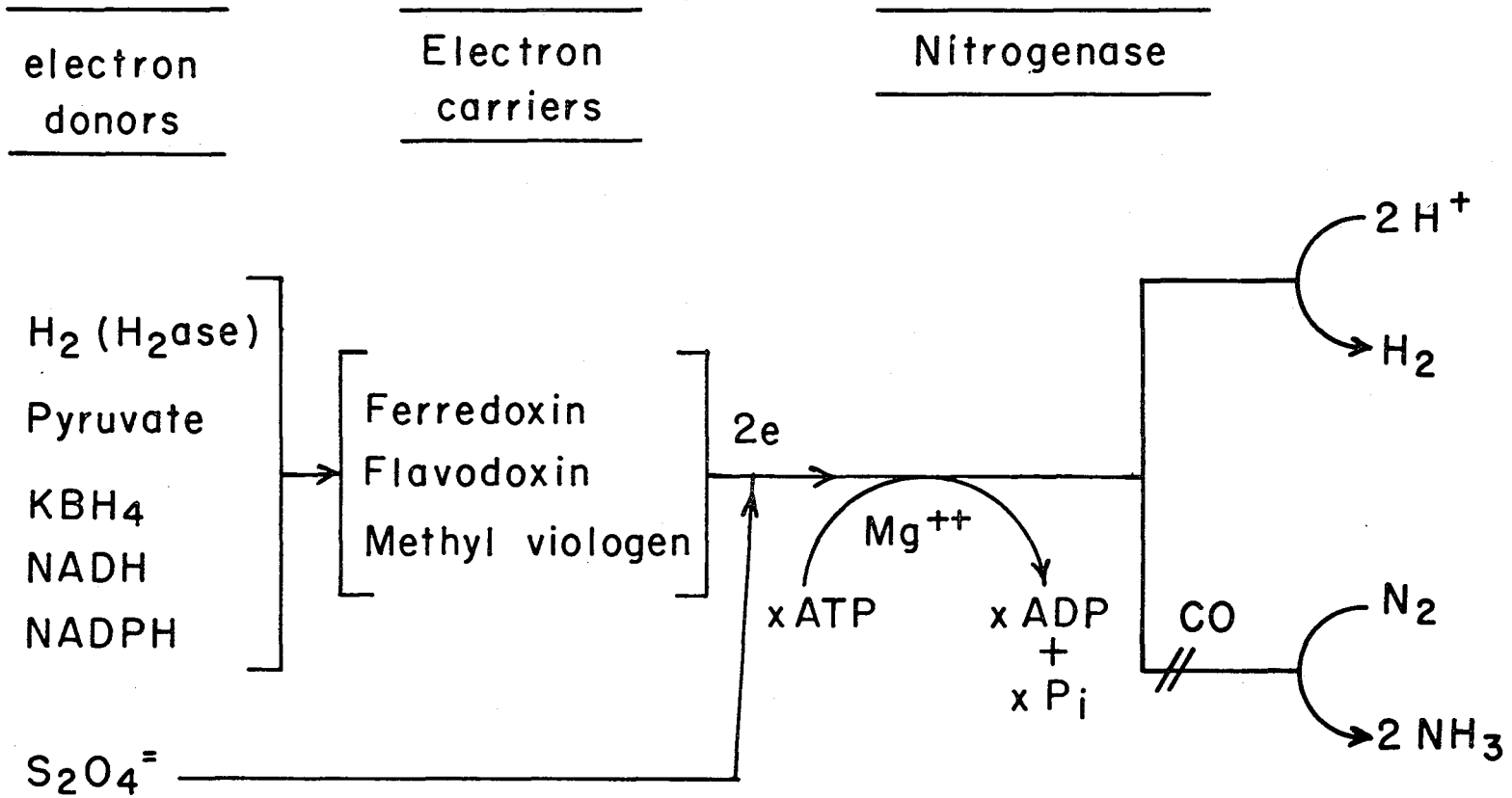

XBL745-5155

Figure 2

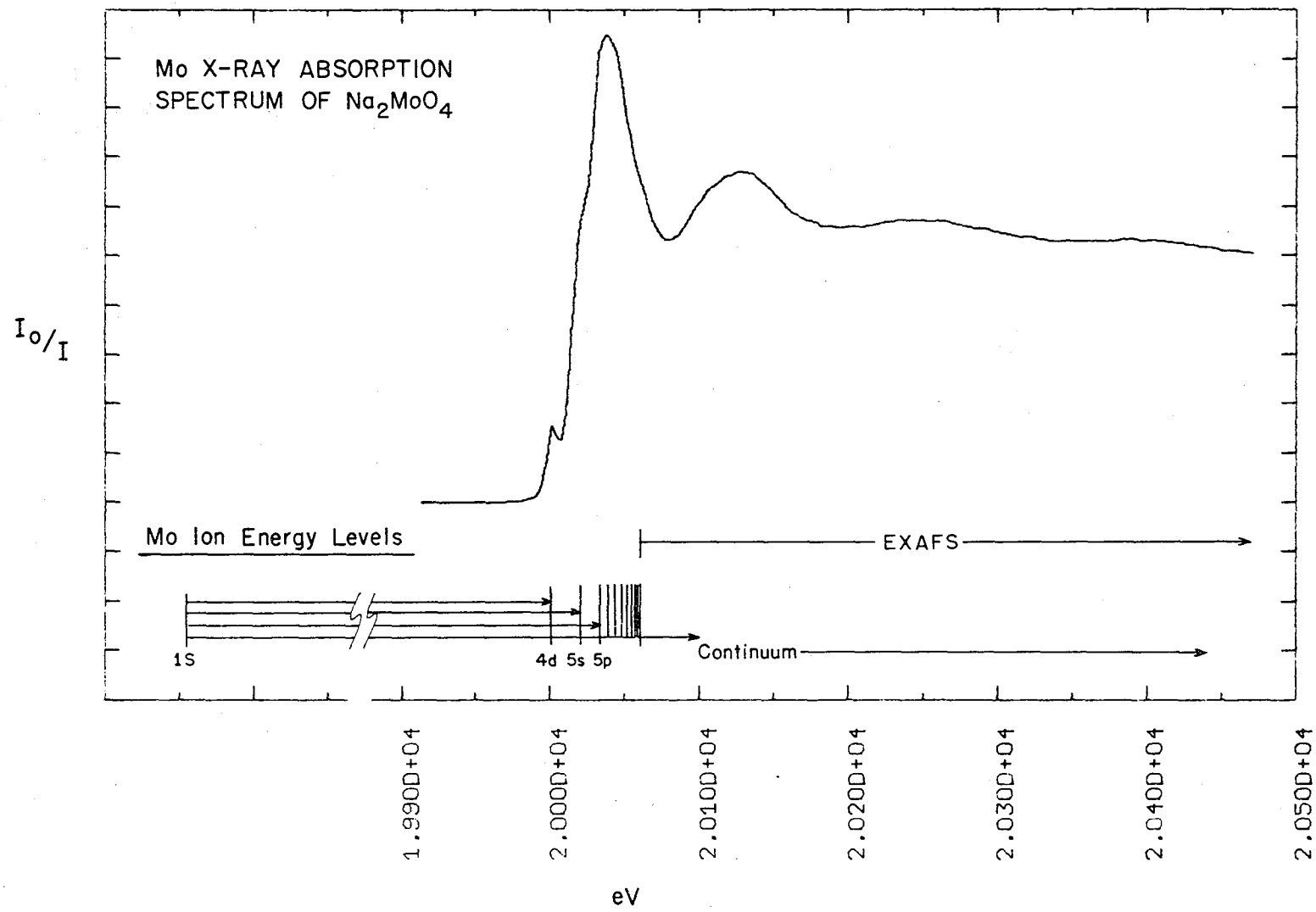

XBL 764-5809

Figure 3

Chapter II

X-Ray Absorption Edge Studies

A. Introduction

The linear absorption coefficient for x-rays decreases smoothly with increasing x-ray energy except for a small number of abrupt increases which are known as absorption edges.[1] Occurring at energies just above the characteristic x-ray emission energies for the various elements in the sample, absorption edges correspond to promotion of an inner shell electron to one of the lower lying unoccupied orbitals. The sharp initial rise in absorbance at the edge is generally due to the symmetry allowed promotion of the inner shell electron to a discrete final state orbital. A series of discrete final state orbitals is available for occupation by the ejected electron. These orbitals become more closely spaced with increasing energy and eventually merge with a continuum band of unoccupied "free electron" states[2].

In the ideal case, the x-ray absorption spectrum provides an uncontaminated plot of the magnitude of x-ray absorbance vs. x-ray energy. This ideal case function may be thought of as[2] $N(E)T(E)$, a product of the density of states at an energy E above the ground state and the transition probability $T(E)$ for promotion of an inner shell electron to the final state.

The energies of the lowest lying unoccupied states are determined by the nuclear charge and oxidation state of the absorbing atom, the strength of any metal-ligand interactions and the effects of the inner shell vacancy on the atomic potential. For noble gases[2] and highly ionic compounds[4] the energies of the excited states of an absorbing atom of atomic number Z are given by the tabulated optical term energies[4] of the Z+1 element. In these systems, the effect of the inner shell vacancy on the valence orbitals is aprroximated by increasing the nuclear charge by 1 unit. For instance, when an isolated Fe(II) atom undergoes the transition

$$Fe(1s^2 2s^2 2p^6 3s^2 3p^6 3d^6) \xrightarrow{h\nu} Fe(1s^1 2s^2 2p^6 3s^2 3p^6 n'l')$$

separations between transitions to the various excited state configurations ($3d^7$, $3d^6 4s^1$, $3d^6 4p^1$, etc.) can be computed from the appropriate term energies for the Co(II) atom.[3]

For transition metal complexes, the lowest lying unoccupied orbitals correspond to molecular orbitals formed by combinations of the valence orbitals of both the metal ion and its ligands. The energies of these orbitals are determined by the energies of the metal and ligand atomic orbitals and the degree of overlap between these orbitals. For strong metal-ligand interactions, the excited state energies will depart significantly from those of the isolated metal atom.

For single electron transitions, the dipole selection rule ($\Delta l = \pm 1$) holds. The major transition observed in K edge spectroscopy would therefore be from the 1s level to an unocccupied np orbital. When the absorbing atom is placed in a chemical environment, the symmetry of the metal site will dictate which orbitals may be occupied by the ejected electron. The strongest transitions for metal sites of O_h symmetry will

be to orbitals of t_{1u} symmetry. For tetrahedral geometries, transitions to orbitals of t_2 symmetry will be "allowed". In actual practice, transitions which are formally forbidden will occur with low intensities due to departures from strictly symmetrical geometry or vibronic coupling.

The x-ray absorption edge spectrum of a transition metal complex is composed of transitions from inner shell orbitals to molecular orbital final states formed from the 3d, 4s and 4p (for a first row transition metal) orbitals of the metal and the valence orbitals of the ligands. UV-VIS absorption spectroscopy is commonly used to probe these orbitals. The information provided by x-ray absorption spectroscopy can be used to complement the results of studies in the UV-VIS region. In L-edge x-ray spectroscopy, the possibility of choosing the symmetry of the initial state (s or p) allows the experimenter to probe different excited states. In cases where the absorption of the metal of interest in the UV-VIS region is weak or masked by other chromophores in the sample, the element specific nature of x-ray absorption spectroscopy may be profitably exploited.

Several factors limit the information obtainable in practice from an x-ray absorption edge spectrum. The features of transitions to discrete final state orbitals can be obscured or confused by the onset of the continuum absorption band. Non-linearites in the absorbance scale can distort the relative intensities of transitions[2]. Features of the spectrum are broadened both by instrumental spectral window and by the lifetime broadening of the inner shell vacancy[2]. The latter problem imposes a serious limitation on the amount of information to be gained froms studies of molybdenum K-edge spectra. The width of the molybdenum

K shell vacancy (3.6 eV)[2] is significant when compared to the spread of energies (0 - 30 eV) of the low lying unnocupied orbitals of transition metal complexes.

The x-ray absorption edge spectra of many transition metal complexes have been studied with conventional x-ray tube spectrometers. The review by Srivastava and Nigam[5] provides a good introduction to the literature on this subject. Although the edge spectra of molybdenum compounds are of interest in the present work, the results of studies on complexes of first row metals will serve as a guide to the type of information that can be obtained from edge studies.

There are several approaches to the interpretation of absorption edge spectra. A qualitative classification system, proposed by Van Nordstrand[6,7] attempts to correlate absorption edge shape with coordination geometry, type of ligand and type of metal-ligand bonding. A particularly marked change in edge shape occurs upon changing from octahedral to tetrahedral coordination. The pink to blue color change (octahedral to tetrahedral coordination) in aqueous solutions of Co(II) has been studied by x-ray absorption spectroscopy and provides a good illustration of this effect.[8]

Several authors have tried to correlate features of edge structure with the oxidation state of the metal, the nature of the surrounding ligands and the coordination geometry. The "edge width"[9], the position of the main absorption maximum[10] and the position of the inflection point in the absorption edge[11] have been used as marker features. A critical examination of the literature shows that these techniques have good predictive power as long as only one structural feature is allowed to vary. For instance, within a series of metal complexes with

octahedral coordination by oxygen, the energy of the edge inflection point may be a good indicator of the oxidation state of the metal.

When considering the spectra of compounds of different geometry, marker features such as edge inflection point energies may have different physical significance. Consider the case of octahedral vs. tetrahedral coordination of a first row transition metal ion. For octahedral geometry, the lowest unoccupied orbital of suitable symmetry for a transition form the K shell (t_{1u}) is antibonding in character and is significantly higher in energy than the 4p orbital of the free metal ion[12]. In some cases, the transition to the t_{1u} orbital will be incompletely resolved from transitions to other discrete orbitals of higher energy or from the onset of the continuum band. As a result, a single major inflection point will be observed, corresponding to the onset of the 1s-t_{1u} transition. For tetrahedral geometry, the lowest unoccupied orbital of t_2 symmetry is a bonding orbital[13,14]. Transitions to this orbital and, in some cases, other orbitals of t_2 symmetry will be well resolved from the onset of continuum absorption. In this case, several inflection points will be observed in the edge structure. A direct comparison between the inflection point energies for the two extreme cases discussed above would be inappropriate, because the inflection points mark fundamentally different spectral features. In the case of higher energy edges, such as that of molybdenum (20 KeV), the possible presence of incompletely resolved structure due to the 3.6 eV lifetime broadening of the K shell hole can further complicate the interpretation of the various marker features of absorption edge structure. In fairness to these techniques, it should be noted that when the nature of the metal site of interest is unknown, interpretation

of edge structure is necessarily on a qualitative level. However, the very real limitations of qualitative techniques for the interpretation of absorption edge structure should not be ignored.

When the identity and arrangement of the ligands around the metal atom are either known or the subject of intelligent speculation, the interpretation of absorption edge structure can proceed on a more rigorous plane. The atomic energy levels of the Z+1 metal serve as starting points for the analysis, and the effects of surrounding ligands may be taken into account by the use of molecular orbital theory. Several detailed interpretations of edge spectra along these lines have been reported.[1,13,15,16,17]

B. Materials and Methods

Edges spectra were recorded in the absorption mode using the facilities of the Stanford Synchrotron Radiation Laboratory. The EXAFS I spectrometer was used for the studies of model compounds while nitrogenase spectra were recorded on the EXAFS II spectrometer. The details of the x-ray spectrometers and the data acquisition system have been described elsewhere.[18,19]

The tris (3,4 dithiotoluene)Mo(VI) complex was prepared by the method of Gilbert and Sandell.[20] The other molybdenum model compounds were commerically available reagent grade chemicals. The spectrum of tris (3,4 dithiotoluene)Mo(VI) was taken on a benzene solution of the complex. Spectra of the other molybdenum compounds were taken on mixtures of the compounds with cellulose powder that had been pressed into pellets.

Enzyme samples were prepared according to the method of Shah and Brill.[21] The Mo-Fe component of nitrogenase was crystallized under

hydrogen and redissolved in argon saturated buffer (0.25 M NaCl, 0.025 M Tris-HCl, pH 7.45) containing 0.006 M $Na_2S_2O_4$. The protein concentration of the solution was approximately 60 mg/ml. Part of the argon saturated sample was placed in an argon flushed cuvette which was then sealed and frozen. The remainder of the enzyme solution was equilibrated with N_2 by repeated evacuation and filling of the sample flask with N_2. After 10 minutes of shaking at 0 ^{o}C, the sample was placed in an N_2 flushed cuvette which was then sealed and frozen. For acquisition of x-ray absorption data, the argon and N_2 equilibrated samples were thawed under an atmosphere of argon or N_2, respectively. During the acquisition of x-ray absorption spectra, the samples were maintained at 4 ^{o}C by cooling with a stream of cold N_2 which was passed through a styrofoam box containing the samples.

The enzyme samples for this experiment were drawn from 5 separate preparations, with a weighted specific activity of 1648 (nanomoles of C_2H_4 produced per minute per milligram of Mo-Fe protein). The range of specific activities was 1325 to 1770. After the x-ray spectra were recorded, the enzyme samples were re-assayed. The specific activity of the argon equilibrated sample was 1212 and that of the N_2 equilibrated sample was 1400.

Sample cuvettes for x-ray absorption measurements of enzyme samples were made from 1/8" thick Lucite stock with DuPont "kapton" polyimide film windows (0.001 " thick). To facilitate the simultaneous measurement of absorption and fluorescence spectra, the cuvettes were cut at a 45^{o} angle with respect to the incident beam.

The energy scale of the x-ray monochromator was calibrated using the spectrum of molybdenum metal foil as a reference standard. The

energy scale was defined so that the inflection point in the molybdenum foil edge would occur at an energy of 20003.9 eV.[22] The inflection point position was determined from the location of the zero crossings of the second derivative of the absorption edge. To calculate the value of the absorbance derivative at any point in the spectrum, a third order polynomial was fitted to the data over a domain of 10 eV above and below the point of interest, followed by computation of the analytical derivative of the fitted function. Second derivatives were computed by two applications of this routine in succession.

C. Results

The edge spectra of several molybdenum containing compounds are shown in figure 1. For these spectra, the absorbance was measured every 2.5 eV. Each point was counted for 1 second. The first derivatives of the absorption edge spectra of the molybdenum compounds are shown in figure 2.

Figure 3 shows the edge spectra of the two nitrogenase samples, along with the spectra of molybdenum foil and of a sodium molybdate solution. The foil and molybdate spectra were recorded during the same data collection as the enzyme spectra. In the region plotted, data points were taken every 1.6 eV. The enzyme spectra are the averages of 6 scans (argon) or 10 scans (N_2), amounting to counting times of 24 and 40 seconds per point, respectively. In figures 1 and 3 the absorbance due to the molybdenum K shell has been isolated by fitting a first or second order polynomial to the pre-edge region of the spectrum, followed by extrapolation and subtraction of the fitted function from the entire data set. When properly carried out, this procedure yields spectra that are flat in the pre-edge region with a small negative slope in the post-

edge portion of the data. The first derivatives of the nitrogenase spectra are shown in figure 4. The average inflection point energies for the nitrogenase spectra are listed in table I. The errors in the inflection point energies for the nitrogenase samples were estimated by measuring the inflection point energy for each of the scans used in the average scans and then calculating the standard deviation of the mean inflection point energy.

D. Discussion

The compounds whose spectra are depicted in figure 1 represent a variety of molybdenum oxidation states and site symmetries. X-ray diffraction structural data on the compounds themselves or on closely analogous compounds are available.[23 - 28] The spectra serve to indicate the sensitivity of molybdenum K edge structure to the environment of the metal atom. Drastic changes in site symmetry produce correspondingly large changes in edge structure.

Contrast the spectrum of the octahedral K_3MoCl_6[23] with that of the tetrahedral $Na_2MoO_4 \cdot 2H_2O$[27]. The spectrum of the latter compound is a type IV-a edge structure, according to the classification scheme of Van Nordstrand.[6,7] This type of edge is always observed for formally d^0 metals in tetrahedral environments. The absorption edge of the permanganate (MnO_4^-) ion has been analyzed in terms of a molecular orbital picture by Best[15]. In that treatment, the sharp spike that occurred before the main absorption maximum was attributed to a symmetry allowed transition to the lowest lying unfilled orbital of t_2 symmetry. Molecular orbital calculations for MoO_4^{-2} have been reported by Kebabcioglu et al.[29] According to the scheme described in that report, the lowest unoccupied orbital of t_2 symmetry was labeled $4t_2$. The peak

in the molybdate edge at 20002 eV can reasonably be assigned to the 1s - $4t_2$ transition. The $5t_2$ orbital was predicted[29] to be 17 eV above the $4t_2$ level. The position of the shoulder at 20021 eV in the molybdate edge spectrum is in good agreement with this prediciton.

According to the Z+1 rule for obtaining the level splittings from free ion optical data, the molecular orbital energy levels of the TcO_4^- ion would be more appropriate for the analysis of the molybdate edge spectrum. The results of Muller and Dieman[30] indicate that the $4t_2$ - $5t_2$ aplitting in TcO_4^- would be about 1 eV less than the corresponding splitting in MoO_4^{-2}. This small difference is less than the uncertainty in assigning the experimental splitting between the features in the molybdate edge spectrum.

As part of a recently published report[33], Cramer and co-workers presented the x-ray absorption edge spectrum of the thiomolybdate anion, MoS_4^{-2}. The thiomolybdate edge spectrum is similar to that of the molybdate anion, but the features on the low energy side of the absorption maximum are not as well resolved. The calculations of Kebabcioglu et al.,[29] predict that the $4t_2$ - $5t_2$ splitting in MoS_4^{-2} will be 55 % of the $4t_2$ - $5t_2$ splitting in MoO_4^{-2}. Based on an examination of the derivative of the thiomolybdate edge spectrum presented by Cramer and co-workers[33], the splitting between the features on the low energy side of the absorption maximum is 57 % of the corresponding splitting in the MoO_4^{-2} spectrum in figure 2. This result lends further credence to the identification of the two features on the low energy side of the absorption maximum in tetrahedrally coordinated molybdenum compounds as fully allowed 1s - nt_2 transitions.

Compared with the sodium molybdate edge spectrum, the absorption

edge of the octahedral K_3MoCl_6 is relatively featureless. The first derivative of the K_3MoCl_6 absorption edge shows the presence of a single inflection point and gives evidence of structure on the low energy side of the first absorption maximum.

When the metal site symmetry is lower than octahedral, the larger number of orbitals of acceptable symmetry for "dipole allowed" transitions leads to complex edge spectra. For instance, molecular orbital calculations for tris-(1,2 dithiobenzene)Mo(VI)[31] (D_{3h} symmetry) indicate the presence of two orbitals of correct symmetry within the first 7 eV of unoccupied levels. The 3.6 eV width of the inner vacancy of molybdenum would tend to broaden the edge spectrum of this compound, leaving poorly resolved shoulders, or even worse, only a smooth broad edge.

Curve c of figure 1 depicts the spectrum of tris-(3,4 dithiotoluene)Mo(VI). This compound could be expected to have an electronic structure similar to that of the dithiobenzene complex considered above. The first derivative of the edge spectrum of the dithiotoluene complex (figure 2) suggests the presence of two incompletely resolved transitions in the edge. The same is true for the spectrum of MoO_2. In both of these cases, the absorption edge is considerably broader than that of K_3MoCl_6, suggesting the presence of unresolved transitions in the edge region.

The edge structure of MoO_3 suggests a combination of features from the extreme cases of tetrahedral and octahedral geometry. The x-ray structure of this compound[27] reveals that the first coordination sphere of molybdenum is composed of six oxygen atoms. Four of the oxygens, at radii of 1.7 - 2.0 A, are situated in a tetrahedral arrangement. The

other two oxygens (2.2 - 2.3 A) are placed so as to make the entire structure a rather distorted octahedron. With molybdenum and four of the oxygens lying in a mirror plane[27], the site symmetry is C_s[32]. The first derivative of the MoO_3 spectrum is very similar to that of sodium molybdate, suggesting that the tetrahedrally arranged nearest neighbors of the molybdenum are the most important in determining the x-ray absorption edge spectrum.

This series of spectra reveal some of the limitations of molybdenum K edge spectroscopy. Subtle changes in the metal's coordination environment will have the greatest effect on the energies of the lowest lying unoccupied orbitals. Because of the 3.6 eV inner shell vacancy, small perturbations of these levels may go undetected. In the absence of resolution of the various edge festures, the interpretation of inflection point energies and the energies of absorption maxima is difficult. It is clear, however, that major changes in site symmetry are detectable.

The nitrogenase spectra in figure 3 show that the low energy side of the edge is broad and featureless, while there is a distinct shoulder on the high energy side of the absorption maximum in both spectra. A somewhat broader shoulder is observed in the spectrum of tris-(3,4 dithiotoluene)Mo(VI). In cases of quasi-octahedral symmetry, shoulders on the main absorption maximum have been attributed to splitting of the first excited state due to asymmetric corrdination.[1] Due to differences in monochromator resolution, the widths of edge features in figures 1 and 3 are not directly comparable. As a result, it would not be appropriate to attempt to interpret the difference in the widths of the shoulders in the spectra of nitrogenase and the dithiotoluene complex.

It is apparent that the presence of dinitrogen has little effect on the molybdenum edge structure of nitrogenase. Within experimental error, the inflection point energies of the two spectra are the same. A shoulder on the high energy side of the main absorption maximum appears to become broader in the presence of dinitrogen. Although this suggests some substrate effect, experience has shown that it would be premature to attempt an interpretation of this effect in the absence of confirmation by another data set of comparable quality.

In a recently published report[33], Cramer and co-workers presented the absorption edge spectrum of the molybdenum-iron component of nitrogenase from Clostridium pasteurianum. The absorption edge spectrum and first derivative edge spectrum of Clostridium pasteurianum nitrogenase are very similar to those presented in figures 3 and 4. The inflection point of the Clostridium pasteurianum spectrum reported by Cramer[33] and co-workers was 4 eV higher than that reported in this work for Azotobacter nitrogenase. This discrepancy can be attributed to differences in the definition of the energy scale reference. In this work, the molybdenum foil absorption edge derivative was computed by fitting a thrid order polynomial to the data over a total domain of 10 eV above and below the point of interest. Cramer and co-workers used a fitting domain of 3.5 eV above and below the point of interest[33]. The use of the larger fitting domain has the effect of moving the molybdenum foil edge inflection point to a higher energy, causing an apparent decrease in the energy of the nitrogenase edge inflection point energy. For a further discussion of the effect of fitting domains on the energy scale definition, see chapter IV of this thesis.

The observations reported in this work rule out the possibility

that a dramatic change in the coordination environment of the molybdenum in nitrogenase occurs in the presence of dinitrogen. Does this result preclude the direct binding of dinitrogen to molybdenum under the conditions of this experiment? The effect of dinitrogen coordination on the edge structure would depend on what, if any, ligands were displaced to accommadate the dinitrogen, the effects of dinitrogen coordination on the remaining ligands of molybdenum and the effects of dinitrogen coordination on the electronic structure of the metal center. For instance, if the coordination of dinitrogen represented the introduction of a pi-acceptor ligand into a coordination sphere that had no other ligands of this type, a major change in edge structure would be expected.[34] It is conceivable that if dinitrogen displaced another pi-bonding ligand of similar electronegativity, only a small, prehaps undetectable change would occur in the absorption edge. The present data, therefore, do not completely rule out the possibility that dinitrogen binds to the molybdenum in a solution of the molybdenum-iron component of nitrogenase.

In summary, it is concluded that the presence of dinitrogen causes no major perturbation of the coordination environment of the molybdenum in the molybdenum-iron component of nitrogenase. Under the conditions of this experiment, the enzyme was not capable of actually reducing substrate. It would be of interest to compare the results of this study with spectra of nitrogenase samples conatining both protein components as well as concentrations of ATP and reductant sufficient to support the turnover of substrate. The 3.6 eV width of the molybdenum inner vacancy presents a serious limitation to the amount of information to be gained from studies of the molybdenum K edge of nitrogenase samples. The use of molybdenum L edge spectroscopy would overcome this problem. Unfortun-

ately, this x-ray energy range (2.8 KeV) is not available with present day synchrotron radiation sources.

References

1. G.L. Glen and C.G. Dodd; J. Appl. Phys.(1968)39, 5372 - 5377.

2. L.G. Parratt; Rev. Mod. Phys.(1959)31, 616 - 645.

3. R.G. Shulman, Y.Yafet, P. Eisenberger and W. Blumberg; Proc. Nat'l. Acad. Sci.-USA(1976)73, 1384 - 1388.

4. C.E. Moore; Atomic Energy Levels, Nat;l. Bureau of Standards. (USA) (1952) v.II-III.

5. U.C. Srivastava and H.L. Nigam; Coord. Chem. Rev.(1972-1973)9, 275 - 310.

6. R.A. Van Nordstrand; Non-Crystalline Solids, ed. V.D. Frechette, J. Wiley & Sons, N.Y.(1958), 168 - 198.

7. R.A. Van Nordstrand; Handbook of X-Rays, ed. E.F. Kaeble, McGraw-Hill Book Co., N.Y.(1967), 43-1 - 43-18.

8. C. Mandel and A.R. Chetal; Ind. J. Phys.(1964)38, 433 - 436.

9. E. Vainshtein, R. Ovrutskaya, B. Kotlyar and U.R. Linde; Soviet Physics: Solid State(1964)5, 2150 - 2153.

10. H.L. Nigam and U.C. Srivastava; Chem. Commun.(1971)14, 761 - 763.

11. S. Cramer, T. Eccles, F. Kutsler, K. Hodgson and L. Mortenson; J. Am. Chem. Soc.(1976)98, 1286 - 1287.

12. M. Karplus and R. Porter; Atoms and Molecules, W.A. Benjamin Co., N.Y.(1970), 427.

13. M. Wolfsberg and L. Helmholz; J. Chem. Phys.(1952)20, 837 - 842.

14. A. Viste and H. Gray; Inorg. Chem.(1964)3, 1113 - 1123.

15. P.E. Best; J. Chem. Phys.(1966)44, 3248 - 3253.

16. W. Seka and H. Hansen; J. Chem. Phys.(1969)50, 344 - 350.

17. K. Tsutsumi, O. Aita and K. Ichikawa; Phys. Rev. B.(1977)15, 4638 - 4643.

18. B.M. Kincaid; Ph. D. Thesis, Stanford University(1974).

19. J.A. Kirby; Manual for EXAFS Program, Lawrence Berkeley Laboratory Report No. UCID - 3952(1977).

20. T.W. Gilbert and E.B. Sandell; J. Am. Chem. Soc.(1960)82, 1087 - 1091.

21. V.K. Shah and W.J. Brill; Biochm. Biophys. Acta.(1973)305, 445 - 454.

22. J.A. Bearden; Rev. Mod. Phys.(1967)39, 78 - 106.

23. Z. Amilius, B. Van Laar and H.M. Rietveld; Acta Cryst. (1969)B25, 400 - 402.

24. B.G. Brandt and A.C. Skapski; Acta Chem Scand.(1967)21, 661 - 672.

25. T.P. Sleight, C.R. Hare and A.E. Sleight; Mat. Res. Bull.(1968)3, 437 - 444.

26. L. Khilborg; Arkiv For Kemi(1963)21, 357 - 363.

27. K. Matsumoto, A. Kobayashi and Y. Sasaki; Bull. Chem. Soc. Japan, (1975)48, 1009 - 1013.

28. A.E. Smith, G.N. Schrauzer, P. Mayweg and W. Heinrich; J. Am. Chem. Soc.(1965)87, 5798 - 5799.

29. R. Kebabcioglu, A. Muller and W. Rittner; Chem. Phys. Lett.(1971)8, 59 - 62.

30 A. Muller and E. Dieman; Chem. Phys. Lett.(1971)9, 369 - 374.

31. G.N. Schrauzer and P. Mayweg; J. Am. Chem. Soc.(1966)88, 3235-3242.

32. I.R. Beattie and T.R. Gilson; J. Chem. Soc. A(1969), 2322 - 2327.

33. S.P. Cramer, K.O. Hodgson, W.O. Gillum and L.E. Mortenson; J. Am. Chem. Soc.(1978)100, 3398 - 3440.

34. T.P. Walker; unpublished observations of the edge structure of trans-bis-dinitrogen bis(1,2 diphenylphosphinoethane)Mo(0) and its tetrahydride analog show that the absorption edge of the dinitrogen complex has very definite structure both above and below the first absorption maxima. whereas the tetrahydride species has a smooth featureless edge.

Table I

Inflection Point Energies for the Spectra in Figure 3

Sample	Inflection Point Energy (eV)
Mo Foil	20003.9
Mo-Fe + Argon	20006.6 ± 0.9[1]
Mo-Fe + N_2	20007.1 ± 1.0[1]
MoO_4^{-2} solution	20000.0[2]
	20008.7
	20017.1

Notes

1. The errors in the inflection point energies for the nitrogenase samples were estimated by measuring the inflection point energy for each of the scans used in making up the average scan and then calculating the standard deviation of the mean inflection point energy.
2. Three inflection points are observed in the edge rise region of the sodium molybdate spectrum.

Figure Captions

1. Absorption edge spectra of several molybdenum containing compounds. The spectrum of molybdenum metal foil is shown as a reference. All of the spectra were recorded on solid samples dispersed in cellulose and pressed into pellets except curve c, which was taken on a solution of the compound in benzene.
2. First derivative of absorption edges. The first derivatives in this figure were calculated by fitting a third order polynomial to the data over a domain of 5 eV above and below the point of interest, followed by evaluation of the analytical derivative of the fitted function.
3. Absorption edge spectra of soluitons of the molybdenum-iron component of nitrogenase equilibrated with argon or dinitrogen as indicated. The spectra of molybdenum metal foil and of a sodium molybdate solution are shown as references.
4. Absorption edge derivatives of the nitrogenase spectra shown in figure 3. These derivatives were calculated as described in the caption of figure 2, using a fitting domain of 10 eV above and below the point of interest. Decreasing the fitting domain to 3.5 eV above and below the point of interest revealed no other inflection points in the edge spectra.

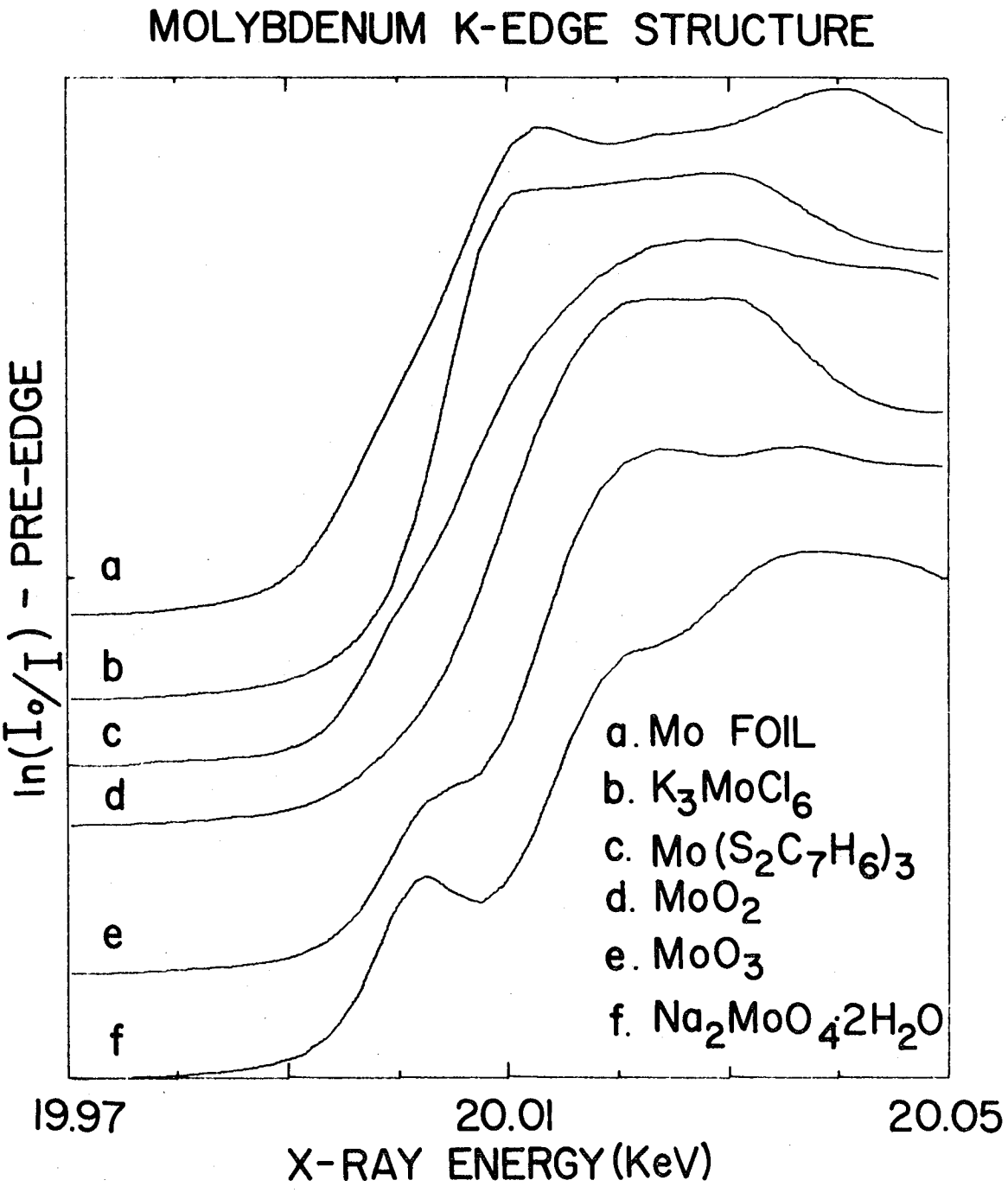

XBL 784-3957

Figure 1

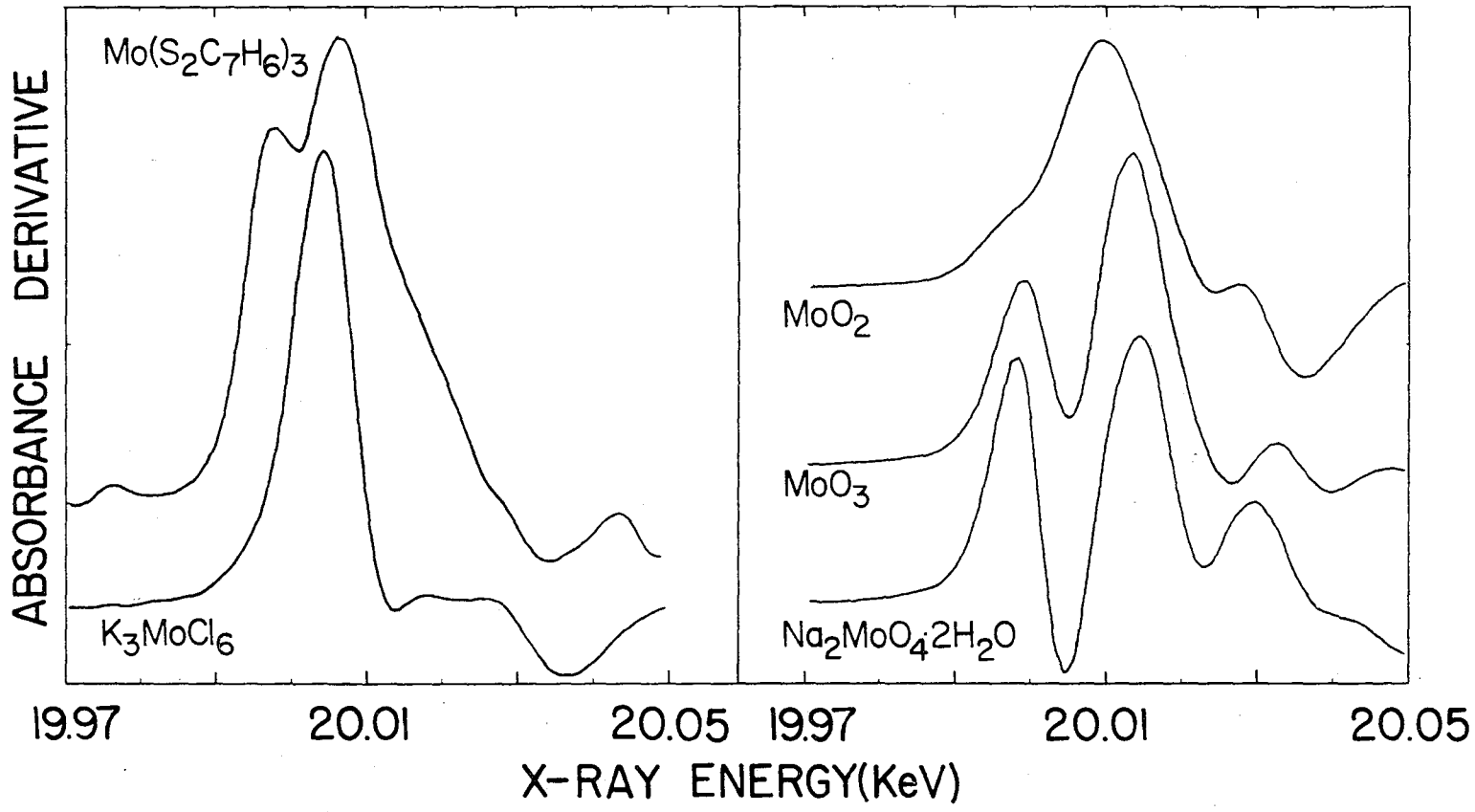

XBL 786-4033

Figure 2

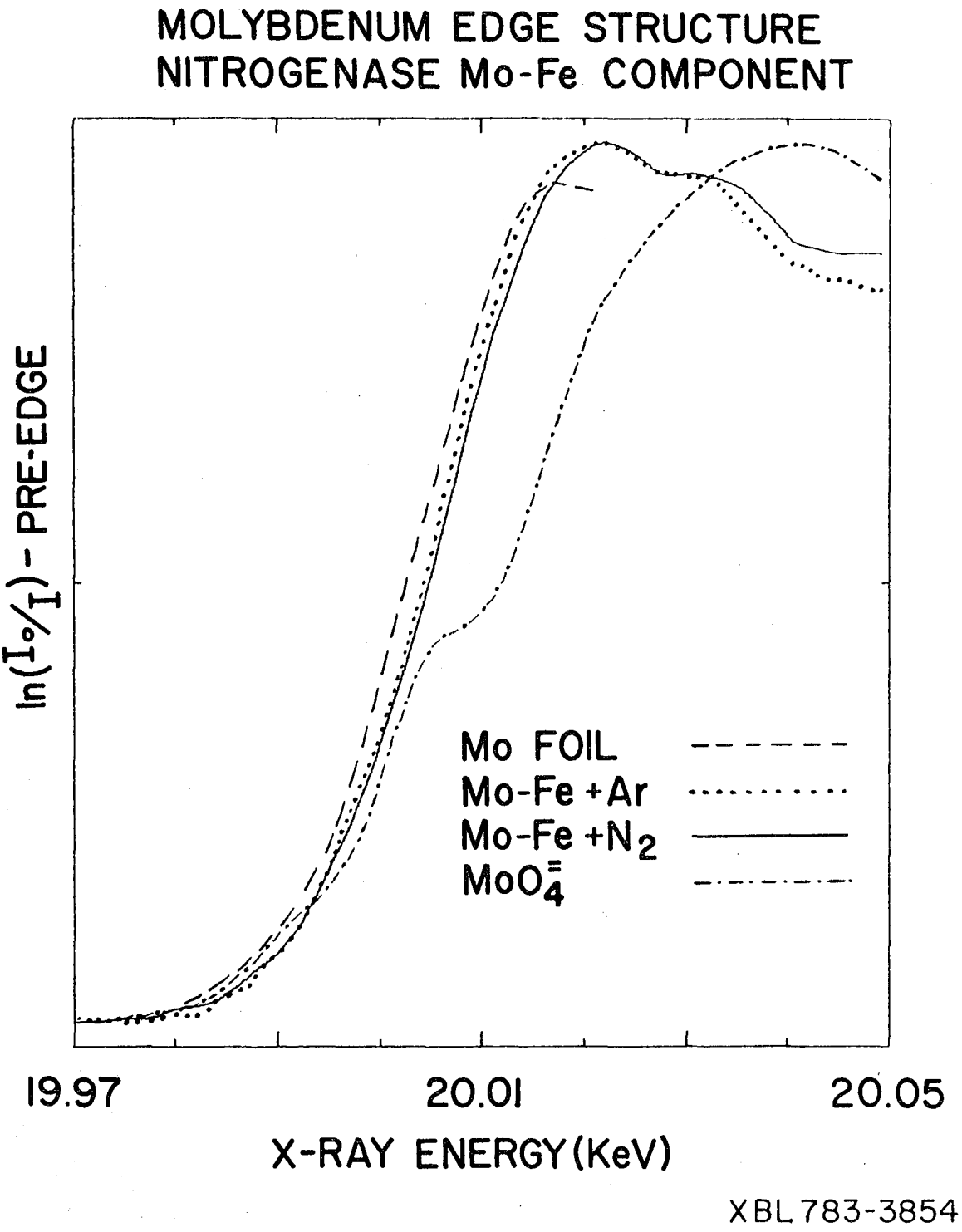
MOLYBDENUM EDGE STRUCTURE
NITROGENASE Mo-Fe COMPONENT
ln(I°/I) - PRE-EDGE
Mo FOIL
Mo-Fe +Ar
Mo-Fe +N2
MoO4=
19.97
20.01
20.05
X-RAY ENERGY(KeV)
XBL 783-3854

Figure 3

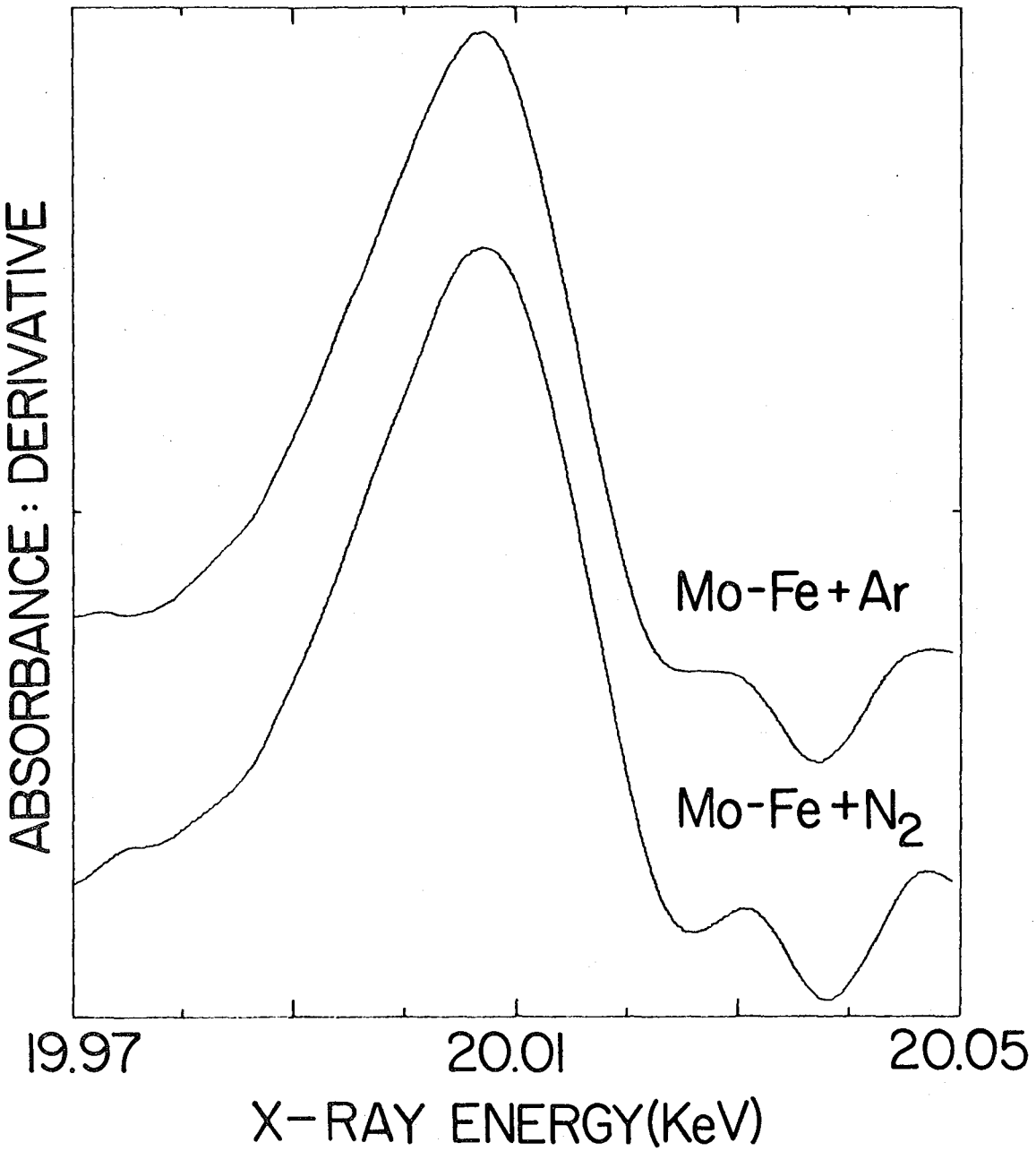
ABSORBANCE: DERIVATIVE
Mo-Fe+Ar
Mo-Fe+N2
19.97
20.01
20.05
X-RAY ENERGY(KeV)
XBL786-4040

Figure 4

Chapter III

EXAFS Studies

A. Introduction

The x-ray absorption spectrum of a monatomic gas has sharp increases in the absorption coefficient at the absorption edges, accompanied by fine structure within a few electron volts of the edge. Above the absorption edge, the absorption coefficient decreases smoothly with increasing x-ray energy. This behavior is in accord with the simplest theory for photoabsorption.[1] For molecules in the gaseous or liquid states, and for crystalline or amorphous solids, the absorption coefficient displays modulations that persist as far as 1 - 2 KeV above an absorption edge. These modulations are known as extended x-ray absorption fine structure or EXAFS.

EXAFS is the result of final state interference effects due to the backscattering of photoelectrons by atoms in the vicinity of the absorbing atom.[2] When the backscattered photoelectron wave interferes with the outgoing wave near the absorbing core in a constructive(destructive) manner, the absorption coefficient is increased(decreased). Meeting the conditions for constructive or destructive interference depends on the wavelength of the photoelectron, the round trip path length between absorber and scatterer and the potential through which the photoelectron travels during the scattering process. The effect of the potential is

to introduce a phase delay in the photoelectron wave.

As the photoelectron wavelength is scanned (accomplished in practice by changing the x-ray energy) the absorption coefficient is modulated as the conditions for constructive or destructive interference are, in succession, met. The EXAFS may be thought of as a kind of interferogram, whose periodicities are sensitive to the distances between the absorbing and scattering atoms.

The earliest attempts to explain EXAFS date from the 1930s.[3] These theories, based on assumptions of long range order in the sample material, did not adequately explain the occurrence of EXAFS in disordered systems. More recent approaches have attempted to explain EXAFS as a phenomenon dependent on the short range order around the absorbing atom.[2,4,5] These treatments have met with greater success in the interpretation of EXAFS. The advent of synchrotron radiation sources for x-ray spectroscopy has generated great interest in the use of EXAFS as a structural probe in chemical[6] and biochemical[7] systems. This interest has encouraged the developement of theoretical treatments of the EXAFS phenomenon.[8]

EXAFS is expressed as a normalized modulation of the absorption coefficient.

$$\chi(k) = \frac{\mu(k) - \mu_B(k)}{\mu_0(k)} \qquad (1)$$

In equation 1, $\mu(k)$ is the measured absorption coefficient, or some quantity proportional to it. $\mu_B(k)$ is a smooth "background function", designed to remove the free atom absorbance and instrumental contribution from the EXAFS. $\mu_0(k)$ is the free atom photoabsorption cross

section for the absorbing element and shell (K or L) of interest. Division by $\mu_0(k)$ is performed so that $\chi(k)$ will be equal to a fractional modulation of the free atom photoabsorption cross section.

In equation 1, $\chi(k)$ is written as a function of k, the photoelectron wave vector.

$$k = \hbar^{-1}(2m\,[E - E_0]\,)^{\frac{1}{2}} \qquad (2)$$

In equation 2, m is the photoelectron mass, E is the x-ray energy and E_0 is the reference energy or "zero of k". As the structure of the EXAFS interferogram is directly dependent on the DeBroglie wavelength of the photoelectron, given by $\lambda = 2\pi/k$, the expression of the EXAFS as a function of k rather than of the photoelectron energy is reasonable and convenient. The selection of E_0 and the generation of $\mu_B(k)$ and $\mu_0(k)$ will be discussed below.

In recent theoretical treatments, EXAFS is formulated as being due to the elestic scattering of spherically symmetric photoelectron waves by atoms in the vicinity of the absorber. The neighboring atoms are assumed to be point scatterers. These assumptions lead to an expression for $\chi(k)$ as a sum of damped sinusoidal oscillations.[2]

$$\chi(k) = -\sum_j \frac{N_j}{kR_j^2} |f(\pi,k)|\, e^{-\sigma_j^2} e^{-R_j/n} \sin(2kR_j + \alpha_j(k)) \qquad (3)$$

Each term in this sum corresponds to a "shell" of N_j identical atoms, each at a distance R_j from the absorbing atom. $|f_j(\pi,k)|$ is a backscattering amplitude function which describes the energy dependence of the interaction between the photoelectron and the scattering atom.

A Debye-Waller type factor, $e^{-\sigma^2 k^2}$, allows for the damping of EXAFS due to thermal or structural disorder in the environment of the absorber. Photoelectron decay and other inelastic effects result in distance dependent attenuation of EXAFS, and these effects are reflected in the mean free path factor $e^{-R_j/\eta}$. The argument of the sinusoidal factor contains $2R_j$, the round trip photoelectron path length and the phase shift $\alpha_j(k)$ due to the interatomic potentials experienced during the scattering process. The phase shift function is characteristic of the absorber-scatterer pair of interest.

Equation 3 gives a good description of EXAFS for higher photoelectron energies ($k > 3$) in systems where multiple scatttering may be neglected.[8,9] In spite of its shortcomings, this formula provides a reasonably satisfactory model for the phenomenological analysis of EXAFS.

In this study, EXAFS has been applied to the investigation of molybdenum-substrate interactions in nitrogenase. Specifically, the EXAFS of solution samples of the Mo-Fe component of nitrogenase equilibrated with dinitrogen or argon will be compared in an effort to detect and characterize changes in the coordination environment of molybdenum due to the presence of substrate. In the following paragraphs, the type of information available from EXAFS will be discussed and the applicability of this sort of information to the study of the molybdenum in nitrogenase will be considered.

The major application of EXAFS has been to the determination of absorber-scatterer distances in non-crystalline systems. Absorber - scatterer distance information is obtained by analysis of the periodicities of EXAFS modulations. To obtain distance information, the

contribution of $\alpha_j(k)$ to the sinusoid arguments must be removed. The direct approach to this problem is th analyze EXAFS from a compound of known structure containing the absorber-scatterer pair that is of interest in the unknown compound.[7] More recently, it has been found that through the analysis of EXAFS from a series of model compounds[10], transferable phase shift functions may be computed for a given absorber-scatterer pair.

The contributions of the absorbing and scattering atoms to the phase shift has been determined by ab initio calculations.[11] Through the application of a curve fitting technique, it was found that the dependence of the phase shift contributions of the various elements on the photoelectron wave vector (k) could be expressed as a family of functions, each characterized by four constant parameters. This result led to the tabulation of phase shift parameters for a series of absorbing and scattering elements. The total phase shift function $\alpha_j(k)$ for any absorber-scatterer pair could be formulated by selection of the appropriate tabulated parameters. Initial results from the application of tabulated phase shift parameters have been promising[12]. The use of tabulated phase shift data may obviate the need to find a suitable model compound for every absorber - scatterer pair of interest.

To some extent, the backscattering amplitude function is characteristic of the nature of the scattering atom. Calculations of the backscattering amplitude[13] show that for low Z elements (C, O, N) $|f_j(\pi,k)|$ is large at low values of k but dies away quickly with increasing photoelectron energy. For heavier elements, $|f_j(\pi,k)|$ is small at low k, reaches a maximum at 3 - 10 A^{-1} and then dies out slowly with increasing k. According to equation 3, the envelope of a

single shell in k $\chi(k)$ is given by

$$\frac{N_j}{R_j^2} |f_j(\pi,k)| \; e^{-\sigma_j^2 k^2} e^{-R_j/\ell} \quad . \tag{4}$$

Neglecting any k dependence of the mean free path factor, the k dependence of the envelope is given by $|f_j(\pi,k)| \; e^{-\sigma_j^2 k^2}$. In principle, if the envelope function (4) of each term in equation 3 could be isolated, the k dependence of the amplitude might be used to identify the scattering atom.

In practice, this approach can only distinguish between scatterers with appreciably different atomic numbers. As the atomic number increases, $|f_j(\pi,k)|$ changes smoothly and slowly.[13] The damping of EXAFS modulations at high k is due to the effects of the disorder factor as well as to the decay of the backscattering amplitude. Unless σ could be accurately estimated, the EXAFS envelope could not be used to differentiate between scatterers of similar atomic number (eg. Fe and Mn; or C and N). It is possible to estimate σ from vibrational frequency data[14] or from the temperature dependence of the magnitude of $\chi(k)$. In such cases, the effects of σ on the EXAFS envelope could be removed. However, in cases where enough information is known to make an intelligent estimation of σ, identification of the scattering atoms is usually not a problem.

In summary, the identification of scatterers by the k dependence of the EXAFS envelope is complicated by the effect of σ. It is possible to distinguish between scatterers of markedly different atomic number. Due to the unpredictable size of σ in unknown structures, the backscattering amplitude functions of elements with similar atomic

numbers are not sufficiently distinct to permit scatterer identification on the basis of the k dependence of the EXAFS envelope.

In the above discussion, the sensitivity of EXAFS to the type and arrangement of scattering atoms around the absorbing atom was considered. Suppose, for the moment, that molybdenum in nitrogenase is directly involved in substrate binding, or is closely associated with the substrate binding site. How might substrate binding change the type and arrangement of atoms around the molybdenum? Posiible effects include the introduction of new ligands, and/or the displacement of original ligands. If dinitrogen enters the coordination sphere of molybdenum, one or both of these effects would occur. If dinitrogen is bound to some other site in the enzyme, substrate binding may cause indirect rearrangements of the ligands around molybdenum. The sensitivity of EXAFS to the radial distribution of scatterers around the absorbing atom may be of use in detecting the appearance of new ligands or the rearrangement of existing ones. The sensitivity of the EXAFS envelope to the identity of the scattering atoms could be of use in characterizing the coordination environment of the molybdenum in nitrogenase. Likely candidates for first coordination sphere neighbors of the molybdenum in nitrogenase are carbon, nitrogen, oxygen, sulfur, iron and molybdenum. Although the first three of these possibilities may not be distinguishable on the basis of EXAFS envelopes, the presence of heavier scatterers such as iron or molybdenum should be detectable.

B. Acquisition of EXAFS Data

EXAFS data were obtained at the Stanford Synchrotron Radiation Laboratory. The EXAFS I facility was used for data collection on model molybdenum compounds. The monochromator system and ionization chamber

detection system have been described by Kincaid[14]. The EXAFS II spectrometer, equipped with a similar monochromator and ionization chamber system, was used for nitrogenase data collection. Fluorescence detection was accomplished using silicon solid state radiation detectors. Computer programs for monochromator control and data acquisition were written by Jon Kirby.[15]

C. Initial Data Processing

During data collection, the monochromator stepping motor position, the incident x-ray intensity (I_0), transmitted x-ray intensity (I), and fluorescence intensity (F) were recorded by the computer, along with a variety of scan parameters and bookkeeping data. When more than one fluorescence detector was used, the fluorescence intensity measured by each detector was recorded separately.

Initial data processing was carried out at the CDC 6600/7600 computer facility of the Lawrence Berkeley Laboratory, using programs written by Alan Robertson.[16] Initial data processing included conversion of fluorescence data to F/I_0 units and absorption data to I_0/I units. When multiple scan spectra were recorded during studies of dilute enzyme samples, spectrum averaging was performed at this point.

D. Preparation of EXAFS Data for Analysis

Preparation of EXAFS data for analysis and Fourier transformation of EXAFS were performed on a Xerox Data Systems Sigma-2 computer. Programs for the interactive manipulation of data including background removal, conversion of the abscissa units from monochromator position to energy units to wavevector units, Fourier transformation and plotting of results were written by Alan Robertson.[16]

After initial data processing, abscissa values were converted

from monchromator stepping motor units to x-ray energy units (eV), using the absorption edge position of molybdenum metal foil as an energy reference. For absorption mode data, the natural logarithm of I_0/I was computed, making the ordinate values proportional to the absorption coefficient. In the case of thick samples where the absorber of interest is low in concentration, F/I_0 is proportional to the photoabsorption cross section of the element of interest,[17]

The absorbance or fluorescence due to the K shell of the element of interest was isolated from the background absorbance or scattering due to the other elements in the sample. This was accomplished by fitting a first or second order polynomial to the pre-edge region of the spectrum, followed by extrapolation and subtraction of the fitted function from the entire data set. When performed correctly, this operation provides spectra that are flat in the pre-edge region and that have a small negative slope above the edge. Pre-edge subtraction procedures that introduced a significant curvature into the post-edge region of the data were rejected.

Isolation of the K shell contribution to the absorption or fluorescence was follwed by division of the data by the edge jump and normalization of the spectrum for the gradual falloff of the free atom photoabsorption cross section. As used in the present context, the edge jump is defined as the change in absorbance or fluorescence that occurs at the absorption edge. To estimate the size of the edge jump, a staight line was fitted to the high energy (300 - 1000 eV above the edge) part of the spectrum and was extrapolated back to the absorption edge. The edge jump was taken to be the height of the intersection of the fitted line with the absorption edge above the flat pre-edge portion

of the spectrum. Using tabulated values[18], the K shell photoabsorption cross section of the element of interest was calculated over the energy range of the spectrum. The calculated function was then scaled so as to have a value of 1.0 at the absorption edge. Division of the data by the scaled function yielded the normalized spectrum. The units of the EXAFS modulations extracted from this spectrum would now be "fractional modulation of the K shell photoabsorption cross section ".

Following normalization, the EXAFS modulations were isolated from the smooth free atom absorbance. In practice, the slowly varying background of any experimentally determined EXAFS spectrum contains contributions from the energy dependence of the ion chamber sensitivity and the non-linear response of the ion chamber detection system to the slow decay of the x-ray beam intensity as well as from the "free atom" absorbance. Due to the dependence of the scattering background on geometrical effects and detector resolution, the backgrounds in fluorescence mode spectra are even more pathological. As a result of these considerations, the removal of the slowly varying background from the EXAFS is an empirical art rather than an exact science.

Several techniques for the creation of μ_B, the "background function", have been reported. These include Fourier filtering[19], fitting of polynomials to the EXAFS part of the spectrum[19] and cubic spline fits to the EXAFS[12]. In this work, a running average technique devised by Lytle[20] was employed. In the running average technique, the data points in the normalized spectrum were first made equidistant in energy space by means of a linear interpolation routine. A background value for each point in the spectrum was then computed by averaging the values of the data for (typically) 35 eV above and below the point of interest.

After the first smoothing, the background function, which was given the name S^1, was repeatedly resmoothed by the running average routine, creating, in turn, the functions S^2, S^3, S^4, ..., until the background function had no perceptible modulations in it. Examples of the background functions created by the running average technique are shown in figure 1.

After subtraction of the background, the energy space EXAFS was converted to photoelectron wave vector units or, "k space", using equation 2. The selection of E_0 is an area of ambiguity in the analysis of EXAFS. In principal, E_0 is the x-ray energy required to effectively remove a core electron from the absorbing atom's potential field, leaving it with zero kinetic energy. The difficulty with this definition is that there is no generally agreed upon method for determining E_0 from the experimental data.

Several methods for the selection of E_0 have been proposed. The first is to define E_0 using some feature of the absorption edge as a reference. Reference features that have been proposed include the edge inflection points[19] and the energy of the first absorption maximum.[21] The second method is to pick a constant energy for a series of compounds with the same absorbing element.[22] Finally, in connection with the use of theoretically determined phase shift information, E_0 has been treated as a variable parameter, whose value is to be optimized by numerical techniques.[8,23]

All of the above methods acknowledge the difficulty of establishing a meaningful E_0 from the experimental data. When comparing spectra from a series of compounds with the same absorbing atom, it seems reasonable that E_0 should vary somewhat from compound to compound. Since

E_0 may be thought of as the amount of energy needed to remove an electron from the influence of the core potential, chemical factors such as the oxidation state of the absorber might be expected to change E_0.

An incorrect choice of E_0 will cause errors in distance determinations by the analysis of EXAFS. For a given E_0, the phase shift function $\alpha_j(k)$ for absorber - scatterer pair A - B can be determined from the EXAFS of a compound of known structure conatining the A - B pair. If this information is applied to the analysis of EXAFS from a second compound of known structure containing the A - B pair, the determined A - B distance will be in error unless the E_0 for the second compound is chosen correctly. The successful prediction, using a constant E_0 value, of absorber-scatterer distances in molybdenum compounds suggests that the variation in E_0 from compound to compound may be insignificant.[22] Other authors[8, 12], conversely, have found it necessary to vary E_0 from one compound to another in order to obtain consistently accurate absorber-scatterer distances from EXAFS.

In the present work, the E_0 for molybdenum spectra was usually chosen to be about 6 eV above the absorption maximum of the edge. The dependence of the results of the Fourier transform technique for EXAFS analysis on the choice of E_0 will be discussed in a later section.

E. Analysis of EXAFS

The conversion of the data to k space completes the preliminary manipulations of the EXAFS data. In equation 3, $\chi(k)$ is expressed as a sum of damped sinusoidal modulations. The information to be extracted in an "analysis" of EXAFS lies in the amplitudes and periodicities of the modulations.The task of any analytical technique for EXAFS is to decompose $\chi(k)$ into the contributions of the various terms in equation

3 and to extract the amplitude and frequency behavior of each. To date, EXAFS has been analyzed by the ab initio calculation of $\chi(k)$[5,14], Fourier transformation[9], curve fitting techniques[19] and combinations of curve fitting and Fourier transformation.[12] In this work, we present spectra analyzed by the Fourier transformation technique. The developement of curve fitting techniques was outside the scope of the present study. However, some of the nitrogenase EXAFS data collected during the course of this study have been analyzed using the curve fitting programs and data developed by Cramer, Hodgson and co-workers[22] at Stanford University. The results of that analysis and a brief discussion of the curve fitting approach are presented in the discussion of nitrogenase EXAFS results.

F. Fourier Transformation of EXAFS

A function that is a sum of sinusoidal terms may be decomposed by Fourier transformation. A familiar example of this approach is given by the technique of Fourier transform nuclear magnetic resonance spectroscopy.[24] In this technique, the free induction decay of nuclear magnetic resonance, which is an oscillatory function of time, is Fourier transformed to give a frequency spectrum. In the case of EXAFS, $\chi(k)$ is an oscillatory function of k. In equation 3, k/π and r (the radius variable) are Fourier conjugate quantities in the same sense as are time and frequency in the example of Fourier transform magnetic resonance.

In practice, Fourier analysis of EXAFS is accomplished by evaluation of the integral (5).

$$\phi_n(r) = \int_{k_{min}}^{k_{max}} k^n \chi(k) W(k) e^{-i2kr} \frac{d(2k)}{2\pi} \qquad (5)$$

In equation 5, k_{max} and k_{min} are the upper and lower limits of the domain of $\chi(k)$. W(k)is a window function which describes the finite extent of the data in k space as well as any weighting function imposed on the data during analytical calculations. In this work, Fourier transforms were calculated by a Fast Fourier Transform algorithm.

The magnitude of $\phi_n(r)$, $|\phi_n(r)|$, has a peak corresponding to each major periodicity in $\chi(k)$. If the $\alpha_j(k)$ in equation 3 were constants, the peaks in $|\phi_n(r)|$ would be located at the various values of R_j. In fact, the $\alpha_j(k)$ are not constants, but instead have a strong linear dependence on k as well as a weaker non-linear dependence.[11] A strictly linear dependence of $\alpha_j(k)$ on k results in a simple shift of the peaks in $|\phi_n(r)|$ from the real R_j. The non-linear dependence of $\alpha_j(k)$ on k results in assymetric peaks in $|\phi_n(r)|$ along with additional shifts in the peak positions.

In figure 2, the effects of linear and non-linear phase shifts on the appearance of $|\phi_3(r)|$ are shown. The $|\phi_3(r)|$ were obtained from $\chi(k)$ calculated from equation 3, assuming that a hypothetical iron atom was located at R_j = 5.25 A from the absorber. A backscattering amplitude function for iron was calculated from the data given in reference 13. The phase shift function used was (k) = 10.0 - π - 1.5k + bk^2, where b ranged from 0.0 to 0.09 A^2. A typical value for b would[11] be in the range of 0.02 to 0.04 A^2. The effect of an increasingly positive non-linear dependence of $\alpha_j(k)$ on k is to distort the low R side of the peaks while shifting the maxima to larger values of R.

Thus, the $|\phi_n(r)|$ obtained by Fourier transformation of equation 3 provide "apparent" radial distribution functions, where the peak positions are shifted from the actual values of R_j due to the effect of

$\alpha_j(k)$. In practice, the peaks in $|\phi_n(r)|$ are always shifted to lower apparent radii by several tenths of an Angstrom. The exact value of the apparent phase shift will depend on the absorber-scatterer pair under study, the domain of $\chi(k)$ and the choice of E_o.

Due to damping by the disorder factor and the decay of the back-scattering amplitude function, EXAFS modulations persist over a limited domain in k space. For a given compound and temperature, the $|f_j(\pi,k)|$ and the σ_j are fixed. Damping due to these factors causes an unavoidable broadening of the peaks in $|\phi_n(r)|$. Formally speaking, the sharp peaks present in the Fourier transform of a sum of undamped sinusoids are broadened by convolution with the Fourier transform of the envelope functions $k^{n-1}\,|f_j(\pi,k)|\,e^{-\sigma_j^2 k^2}$. In some cases, W(k) causes additional distortions of $|\phi_n(r)|$. Specifically, if the EXAFS modulations have not been completely damped out at k_{max}, a rectangular W(k) will introduce a series of symmetrically placed sidelobes on both sides of each of the structural or "real" peaks in $|\phi_n(r)|$. The sidelobes of large peaks in the spectrum can complicate the interpretation of the smaller peaks in the spectrum. This problem has been discussed by Hayes and co-workers[25].

The distortion of $|\phi_n(r)|$ by sidelobes can be reduced by apodization of the data with a suitable window function W(K). If W(k) goes smoothly to zero at the ends of the k space data, the sidelobes will be reduced in magnitude. The attenuation of sidelobes is accomplished at the cost of some broadening of the structural peaks in the spectrum.

The use of non-rectangular apodization functions W(k) is discussed in references 23 and 21. In the present work, an apodization function proposed by Kaiser[24] was employed. Figure 2 shows a "family" of Kaiser

window functions. Multiplication of $\chi(k)$ by these functions reduces the size of the sidelobes in $|\phi_n(r)|$. The effects of the application of non-rectangular window functions on sidelobe intensity are shown in figure 3.

Multiplication of $\chi(k)$ by k^n prior to Fourier transformation has two major implications. First, the multiplication by higher powers of k tends to remove some of the damping of EXAFS modulations. This results in narrower peaks in the $|\phi_n(r)|$ and, therefore, greater resolution of closely spaced peaks. An increase in resolution is achieved at the cost of decreasing the signal - to - noise ratio of the data, as discussed below. In practice, once $k^n\chi(k)$ has a relatively flat envelope over the k space domain of the data, little can be gained by further increases in n. In the next section of this chapter, an example of a useful transform with n as high as 5 will be given. The second implication of k^n multiplication concerns the weighting of the data points in the computation of the Fourier transform. The Fourier transform process may be thought of as a many - to - many mapping. For each value of r, the amplitude of the corresponding periodicity in $\chi(k)$ is projected out and integrated over the k space domain of $\chi(k)$. The periodicities with the largest integrated amplitudes will produce the largest peaks in $|\phi_n(r)|$. Multiplication of the data by higher powers of k increases the amplitude of the high k portions of the data, effectively giving that portion of the data greater weight in determining $|\phi_n(r)|$. This has advantages in that errors due to the incorrect choice of E_0 are reduced, and that the assumptions leading to equation 3 have greater validity in this region. On the other hand, while $\chi(k)$ grows smaller with increasing k, the noise present in any measurement of $\chi(k)$ does not. The higher k

portions of the data thus have a lower signal - to - noise ratio, and giving them greater weight in the computation of $|\phi_n(r)|$ results in greater contamination of $|\phi_n(r)|$ by noise. For data with a low signal - to - noise ratio to begin with, this effect limits the useful values of n to 3 or less.

Finally, the computation of $|\phi_n(r)|$ with several values of n can aid in the interpretation of Fourier transforms of EXAFS. It was noted earlier that the backscattering amplitude functions of heavier elements decay more slowly at high k than do those of lighter elements. Thus, increasing the value of n effectively increases the relative contribution of the heavier scatterers to $|\phi_n(r)|$. When a series of transforms with several values of n are examined, the peaks due to the heavier scatterers often grow with respect to the peaks due to lighter scatterers as n is increased. This effect can aid in the assignment of peaks in the Fourier transform to particular scattering elements in the vicinity of the absorbing atom.

G. EXAFS of Compounds with Known Structures

In this section, the EXAFS of several compounds of known structure will be presented. Examination of the data in k space provides visual examples of equation 3, showing the dependence of $\chi(k)$ on the structure of the material. The Fourier transforms of the EXAFS of model compounds illustrate the technique and show the dependence of the results on the choice of E_0, the domain of the data in k space and the weighting of the data in k space prior to Fourier transformation.

In figure 5, the EXAFS of sodium molybdate dihydrate, potassium hexachloromolybdate and molybdenum metal foil are shown. Structural data for these materials and the others to be discussed are presented in table I. Visual examination of the EXAFS in figure 5 suggests that both $Na_2MoO_4 \cdot 2H_2O$ and K_3MoCl_6 have single nearest neighbor distance. This conclusion is in agreement with the structural data. The molybdate EXAFS has a longer period of modulation than that of the hexachloromolybdate EXAFS. This is consistent with equation 3, which suggests that as the absorber-scatterer distance increases, the period of modulation of the EXAFS should decrease.

Comparison of the molybdate and the hexachloromolybdate EXAFS with the EXAFS of molybdenum metal foil is instructive in two ways. First, the highly ordered metal structure, with several "shells" of molybdenum atoms at different distances, produces a much more complex EXAFS interferogram than than that of sodium molybdate or potassium hexachloromolybdate. The second point to note is that in the metal, the amplitude of the EXAFS is small at low k, reaches a maximum at about $k = 7\ A^{-1}$, and then dies out slowly with increasing k. This behavior is characteristic of the backscattering amplitude functions of the heavier elements.

In the case of chlorine and oxygen backscattering, the peaks in the amplitude functions occur [13] below k = 3 A^{-1}. In figure 5, only the high k tails of the chlorine and oxygen backscattering functions are visible.

In figure 6, the EXAFS of iron, copper and molybdenum metal foils are shown. These data have been multiplied by k^3 to emphasize the modulations at high k. Note the peak, characteristic of heavy scatterers, in the EXAFS envelopes of all three samples. The envelopes of the iron and copper EXAFS are roughly similar. The envelope of the molybdenum foil EXAFS is much flatter than those of either iron or copper, and the molybdenum EXAFS is still strong at k = 16 A^{-1}. This behavior is an example of the slower high k decay of the backscattering amplitude function as the atomic number of the scatterer increases.

In figure 7, we show the EXAFS of molybdenum dioxide and trioxide. These are complex materials, each having several distinct Mo - Mo and Mo - O distances less than 6 A. The complex structures produce complex interferograms, with beating due to interference between the modulations produced by several different absorber - scatterer distances. There are large, low frequency oscillations at low k due to Mo - O scattering. The low frequency oscillations decay quickly with increasing k, yielding to higher frequency oscillations due to Mo - Mo scattering.

In figure 8, the EXAFS of tris(3,4 dithiotoluene)Mo(VI) and $Na_2Mo_2O_4cys_2 \cdot 5H_2O$ are shown. In the dithiotoluene complex, the molybdenum is surrounded by 6 sulfur atoms at 2.33 A. The EXAFS of this compound, although quite noisy, shows a fairly flat envelope in the 3 - 7 A^{-1} region, followed by a rapid decay. The EXAFS of the molybdate - cysteine complex clearly shows beating between two differ-

ent frequency modulations. The environment of the molybdenum in this compound consists of 4 oxygens located between 1.7 and 2.3 A, a nitrogen and a sulfur in the same range, and another molybdenum at 2.569 A. The Mo - Mo scattering dominates the EXAFS at high k.

The Fourier transforms of the model compound spectra are shown in figures 9 - 13. In figure 9, the transforms of the molybdate and hexachloromolybdate EXAFS are shown. A single major peak is evident in both transforms.

In figures 10 and 11, the Fourier transforms of the EXAFS of iron and molybdenum foils are shown. In addition to transforms with two different types of k space weighting, a histogram of N/R_j^2 values is shown for each material. The positions of the lines in the histogram have been shifted so that the postion of the low R line in the histogram would coincide with the first shell peak in the Fourier transform.

Examination of the transforms of the metal foil EXAFS reveals 4 discernable peaks in each case. In both figures, peaks of the second and other more distant shells are significantly displaced from the positions expected on the basis of crystal structure data. Although it is conceivable that the process of rolling the foils has resulted in distortions of the metal structure, it is worthy of note that in both cases, the second shell is at larger distance than would be expected on the basis of the crystal structure. This suggests that there is some systematic distortion of the second shell. A probable cause of this distortion is interference of sidelobes of the first shell with the structural peak of the second.

The iron and molybdenum metal foil transforms provide a good example of the use of different k space weighting factors. The envelope

of the molybdenum $k\chi(k)$ has roughly the same shape as the iron $k^3\chi(k)$. The resolution of the $|\phi_1(r)|$ of the molybdenum EXAFS is comparable to that of the $|\phi_3(r)|$ of the iron EXAFS. By increasing the exponent of k multiplication to 3 in the case of molybdenum EXAFS and 5 in the case of iron EXAFS, partial resolution of at least 4 shells is achieved. Because the differences between the various absorber - scatterer distances in iron are smaller than the corresponding differences in molybdenum, the resolution of peaks in the Fourier transform of iron EXAFS would always be poorer, even if the backscattering amplitude functions of the two metals were identical.

In figure 12, the transforms of the EXAFS of tris(3,4 dithiotoluene)Mo(VI) and the molybdate cysteine complex are shown. The low signal - to - noise ratio of the EXAFS of the dithiotoluene complex is apparent from the size of the spurious "noise" peaks in the Fourier transform. The Fourier transform of the molybdate cysteine complex shows two major peaks. The first peak is due to oxygens and a nitrogen in the first coordination sphere of molybdenum, while the major contribution to the second peak is from another molybdenum atom at 2.569 A from the absorber. Although the differences in the various molybdenum - oxygen distances in this compound range from 0.2 to 0.35 A, only one peak is detected in the Fourier transform. The difficulty of extracting structural information from Fourier transforms with overlapping peaks is a major disadvantage of EXAFS analysis by the Fourier transform method.

In figure 13, the transforms of EXAFS of the oxides of molybdenum are shown. The variety of similar Mo - O and Mo - Mo distances in these compounds results in transforms with incompletely resolved peaks. In

this situation, the larger peaks can seriously distort the positions of the smaller peaks in the transform.

In addition to the major peaks in all of the transforms presented above, a series of smaller peaks can be observed. These peaks occur at all values of r in the transforms but are most apparent in the 6 - 10 A range where there are no major structural peaks. To some extent, these peaks are due to contributions to EXAFS from scatterers outside the first coordination shell. However, due to the $1/R^2$ distance dependence of the EXAFS amplitude, and the rapidly increasing thermal and structural disorder of outer shells not directly bonded to the absorber, it is unusual to detect significant structural peaks in Fourier transforms of EXAFS beyond 4 A at room temperature. In cases with multiple scatterers, such as MoO_2 with 6 molybdenum atoms at 5.3 - 5.6 A, metal - metal scattering can sometimes be detected at large distances. In most cases, however, the small peaks that occur at large values of r are due to the noise present in any experimental determination of $\chi(k)$.

Although the noise contributions to $|\phi_n(r)|$ are most apparent at large radii, it must be emphasized that noise contamination is present at all radii. In this respect, it is sometimes useful to show $|\phi_n(r)|$ to a maximum radius of 8 or 10 A, even though no useful structural information can be obtained at these radii. The magnitude of the noise peaks at large radii provides an estimate of the possible noise distortion of $|\phi_n(r)|$ at lower radii where the "real" or structural peaks are located. In the ideal case, noise contributions to $|\phi_n(r)|$ would be "white", that is, of more or less equal intensity at all values of r. In this case, any features of $|\phi_n(r)|$ at low r that are the same size or smaller as the noise peaks at high r could not be given a meaningful

structural interpretation. Peaks less than 3 or 4 times the size of the noise peaks can be seriously distorted by noise contamination.

While discussing the effects of noise on the interpretation of Fourier transforms, it is appropriate to comment on the practice of smoothing the EXAFS data prior to Fourier transformation. In order to accurately represent $\chi(k)$ for apparent radii of R_{max} or less, $\chi(k)$ must be sampled with a minimum k space interval of $k = 2\pi/R_{max}$. This is simply a statement of the Sampling Theorem. In practice, it is not feasible to acquire EXAFS data with the points equally spaced on the k axis. Usually, the data are taken in several regions, with the points in each region roughly equidistant in energy space. As a result, EXAFS spectra are usually oversampled and the resulting number of points is often inconveniently large for processing by Fourier transformation or curve fitting programs. Particularly for the noisy data obtained on dilute biological samples, reduction of the number of data points is often accomplished by smoothing the data followed by deletion of a fraction of the data points. The application of polynomial, gaussian - weighted or Fourier filter smoothing routines allows the number of points to be reduced to a manageable size without significant loss of information.

Through the use of smoothing techniques, it is not possible to remove noise components in the data that are in the frequency range containing EXAFS structural information.[33] In EXAFS, noise contributions corresponding to apparent radii of 1 - 5 A cannot be removed by smoothing without distortion of the structural frequency components in this region. If the smoothing technique employed significantly reduces the size of the noise peaks in the 6 - 10 A range, the resulting $|\phi_n(r)|$

appear to have a higher signal - to - noise ratio than is actually the case. The peaks in $|\phi_n(r)|$ at low values of r are as contaminated by noise as ever, while the high r region of the transform appears to be largely free of noise. It is dishonest and misleading, therefore, to use a smoothing routine that significantly reduces the size of the noise peaks in any radius region of $|\phi_n(r)|$ that is shown in a plot.

The following case is an example of a smoothing procedure that does not result in cosmetic improvements in $|\phi_n(r)|$. Suppose a spectrum has been obtained, stripped of background absorbance, converted to k space, and now consists of 512 equally spaced points in the k space domain of 3 - 16 A^{-1}. If 512 points turned out to be an inconveniently large array for data processing, a reduction in the number of points would be in order. To accurately sample the data to a maximum apparent radius of 15.5 A, there must be no less than 128 equally spaced points in the 3 - 16 A^{-1} domain. A smoothing routine that attenuates all frequency components corresponding to radii in excess of 15.5 A could then be applied and the number of data points then reduced to 128 by keeping every fourth data point of the smoothed array. One way to accomplished the smoothing would be to Fourier transform the 512 point array, apply a rectangular window digital filter over the r space domain of 0 A to 15.5 A and then reverse Fourier transform. Any other type of smoothing routine could be interpreted in terms of its effective transfer function.[33] Any smoothing procedure whose transfer function attenuates frequencies corresponding to radii of less than 15.5 A is not effective in preventing information loss during the reduction of the number of data points to 128. If the transfer function indicates attenuation of frequencies corresponding to radii of 6 - 10 A, the transforms

of the smoothed data will have misleadingly low noise levels in the high r regions of the plot.

The results of the Fourier transform method for EXAFS analysis are known to be dependent on the choice of E_o, k_{min} and k_{max}. In tables II and III the dependence of the Fourier transform effective phase shift on E_o and k space domain is examined for Mo - O, Mo - Cl and Mo - Mo scattering. Examination of these results provides an idea of the sensitivity of the Fourier transform method to the choice of analytical parameters, and should facilitate comparison of the results presented in this work with those of other workers in the field[22]. The results show that a choice of a higher E_o produces an increase in the effective phase shift for all cases examined. Comparison of the effective phase shifts for Mo - Mo scattering in the molybdate-cysteine complex and in molybdenum metal indicate that if the effective phase shifts are to agree, the E_o for molybdenum metal should be chosen about 20-25 eV lower than that for the molybdate-cysteine complex. For example, if the E_o for the molybdenum metal data was set at 20004 eV, the metal edge inflection point, the E_o for the molybdate-cysteine complex would be at 20024 eV, which is just above the first maximum in the absorption edge. Although this example is an extreme case, it illustrates the possible hazards involved in choosing a single, constant E_o for all compounds of a given absorber.

The effective phase shift determined from the $|\phi_n(r)|$ transform is weakly dependent on the choice of k_{min} and more strongly dependent on the choice of k_{max}. Increasing k_{min} tends to decrease the effective phase shift while decreasing k_{max} tends to increase it. Qualitatively, this behavior is in accord with the results of Lee et al.[11], which show

that the phase shift has a negative linear dependence on k and a positive k^2 dependence. The effect of the positive k^2 dependence would be largest at high k.

G. EXAFS Studies of Nitrogenase

Nitrogenase EXAFS data were collected in four major data collections. For each data collection, samples of the Mo-Fe component of nitrogenase were prepared as described in the materials and methods section of the preceeding chapter. In three of the data collections, the nitrogenase samples were maintained at -90 ^{o}C during the experiment. In the fourth data collection, the nitrogenase samples were maintained at 4 ^{o}C during the experiment. With frozen samples, severe problems with the background of absorption mode data were experienced. These problems were apparently due to inhomogeneities introduced into the sample by the freezing process. For this reason, the final data collection was made on liquid samples.

Nitrogenase activity was determined by the acetylene reduction assay immediately after x-ray absorption data collection. For samples maintained in the frozen state, the recovery of nitrogenase activity was generally 90 % or better. For the experiment where the solutions were maintained at 4 ^{o}C, the recovery of the argon equilibrated sample was 75 % and that of the dinitrogen equilibrated sample 88 %. The individual data collections will be referred to by date as described below. Information on the various EXAFS data collections is summarized in table IV.

March 1976. Samples of the Mo-Fe component of *Clostridium pasteurianum* nitrogenase were provided by Michael Henzl of the University of Wisconsin at Madison. Spectra were measured in the fluorescence mode only, using a single channel silicon semiconductor detector with niobium foil fluorescence filters. Enzyme samples were maintained at -90 ^{o}C.

July 1976. Samples of Azotobacter vinelandii Mo-Fe component were used in this and all subsequent experiments. The protein concentration of the samples of Mo-Fe component was 90 mg/ml. Spectra were measured simultaneously in the absorption and fluorescence modes. Fluorescence measurements were made with a three element silicon semiconductor detector operated without niobium fluorescence filters. Long term instabilities in the x-ray monochromator system made an accurate measurement of the absorption edge energy impossible. To correct for drifting of the monochromator, individual scans were shifted before spectrum averaging so that the absorption edge energies of all the scans would be identical. Samples were maintained at -90 ^{o}C during the experiment.

October 1976. Spectra were recorded in both the abosrption and fluorescence modes. Fluorescence measurements were made with a three element silicon detector operated with niobium foil fluorescence filters. Monochromator instabilities again prevented the accurated measurement of absorption edge energies. Individual scans were shifted to a common edge energy before averaging. Samples were maintained at -90 ^{o}C during the experiment.

May 1977. Spectra were measured in both the absorption and fluorescence modes. Fluorescence measurements were made with a three element silicon detector operated with niobium foil filters. Improvements in monochromator stability made an accurate measurement of the nitrogenase absorption edge possible. Nitrogenase samples were maintained at 4 ^{o}C during the experiment.

The EXAFS data from the three data collections on frozen samples were averaged to improve the signal - to - noise ratio. The averaged

EXAFS scans for the nitrogenase samples were created as follows. First, individual scans within the same data collection were averaged. The energy scales of the separate data collections were then adjusted so that the edge energies would be the same for all nitrogenase spectra. The average scans from the separate data collections were then processed for background removal, normalization and conversion to k space as described in section D of the present chapter. A linear interpolation routine applied at this point adjusted the x-axis values of the data files so that each file would have points with identical x-axis values. This step was necessary for the computation of a meaningful average of EXAFS data from different data collections.

Finally, a weighted average of the EXAFS from the separate data collections was computed. The EXAFS from each data collection was weighted by the total number of molybdenum x-ray fluorescence counts colllected just above the molybdenum K edge during that particular data collection. The weighting factor (w) was calculated by the following formula.

$$w = D_F' R s \qquad (6)$$

In equation 6, D_F' is the experimentally determined ratio of the change in the fluorescence count rate at the absorption edge to the total fluorescence count rate above the edge. D_F' may be considered as an empirical version of D_F, the fluorescence detectability factor discussed in chapter V of the present work. D_F' will vary from one spectrum to the next depending on detector resolution and geometry. R is the total fluorescence count rate above the absorption edge and s

is the total counting time per point above the edge in the multiscan averaged spectrum. For instance, if the multiscan average spectrum for a particular data collection is the average of 100 spectra, each counted for 1 second per point, then s would be 100. As defined by equation 6, w is an estimate of the total number of actual molybdenum x-ray fluorescence counts (as opposed to R, which is a total count rate, containing contributions from scattering and x-ray fluorescence) collected during a given data collection. It is recognized that w is not a statistically rigorous weighting factor. However, it does represent a reasonable attempt to take into account variations in signal - to - noise ratio from one data collection to the next. The signal - to - noise ratio will vary due to differences in detector resolution, x-ray beam intensity and total data collection time. The values of D_F', R and s used in computing the average spectra are given in table IV.

The practice of averaging EXAFS from different data collections after normalization and background removal was found to be more convenient than averaging the original spectra in energy space. As a test, the spectra were also averaged in energy space after normalization to insure that all spectra had comparable y-axis units. The Fourier transforms of the EXAFS obatined by this procedure were essentially identical to those obtained by the k space averaging procedure described above.

In figure 14, absorption and fluorescence mode spectra for a nitrogenase sample are presented. Due to the large background absorbance (due largely to the water in the enzyme solution) the change in absorbance at the molybdenum K edge is barely visible. The change in fluorescence at the molybdenum K edge is clearly visible, as are the

modulations due to EXAFS in the fluorescence intensity. In figure 15, the background absorbance has been removed from the absorption mode data. The EXAFS and absorption edge are now clearly visible and can be seen to be similar to comparable features in the fluorescence mode data. In practice, the number of photons counted in the absorption mode experiment are a factor of 10^5 higher than the number counted in a fluorescence measurement. As a result, the absorbance is determined with much higher precision than the fluorescence, and very small relative changes in the absorbance can be measured with a fairly good signal - to - noise ratio.

It will be noted that the absorption mode spectrum in figure 15 is marred by the presence of several discontinuties or "glitches". The origin of absorption mode glitches has been discussed by Kincaid.[14] The glitches are greatly reduced in magnitude in the fluorescence mode spectrum. The reason for this is discussed in chapter IV of the present work. During the course of this work, it has been found that the fluorescence mode of detection is less sensitive to interference by glitches of the type seen in figure 15, as well as those due to small inhomogeneities in the sample material.

The fluorescence mode EXAFS from the average of data collected at -90 ^{o}C are shown in figure 16. The EXAFS from data collected at 4 ^{o}C are shown in figure 17. The x-axis scales in figures 16 and 17 were defined by selecting 20030 eV as k = 0. For purposes of discussion, the data sets in figures 16 and 17 will be referred to as the -90 ^{o}C data and the 4 ^{o}C data, respectively.

H. Fourier Transforms of Nitrogenase EXAFS

The EXAFS of the nitrogenase samples were analyzed by Fourier transformation.[9] In figure 18, the Fourier transforms of the -90 ^{o}C data sets are shown. In addition to the transforms of the EXAFS of samples equilibrated with argon and dinitrogen, a "difference" transform is shown. The difference transform was calculated by Fourier transformation of the difference between the EXAFS ($\chi(k)$) of the Mo-Fe+N_2 sample and that of the Mo-Fe+Ar sample. Identical difference transforms were obtained by subtraction of the normalized energy space (F/I_o) spectra followed by the removal of the residual background. The difference transform should highlight any features of the Fourier transform attributable to the presence of dinitrogen in the EXAFS of the Mo-Fe+N_2 sample.

Examination of the transforms in figure 18 reveals that both the Mo-Fe+Ar and the Mo-Fe+N_2 data display a major periodicity at an apparent radius of 1.72 A, with a shoulder at 2.5 A. There are no significant differences between the two transforms.

The results of the Fourier transform technique depend on the weighting of the data in k space prior to Fourier transformation. By changing the weighting given to different regions of the k space domain prior to Fourier transformation, information can be obtained about the dependence of the EXAFS amplitdue on k. As pointed out earlier, when the high k part of the data is given greater weight in the computation of the Fourier transform, peaks due to scatterers with higher atomic numbers tend to grow with respect to peaks due to scatterers of lower atomic number. Thus, the "k weighting effect" provides a qualitative indication of the presence of scatterers of different atomic number.

In practice, the "k weighting effect" has been observed in molybdenum (MoO_2) and manganese compounds[34]. In some cases, however, where strcutural data indicated the presence of mixed heavy and light scatterers, no "k weighting effect" was observed.[35] As a result, it appears that caution should be exercised when interpreting the "k weighting effect" as an indication of the presence or absence of scatterers of different atomic number.

In figure 19, the Fourier transforms of the -90° C EXAFS weighted by k^3 are shown. The peak at 2.5 A has grown with respect to the 1.72 A component. While the limited predictive reliability of the "k weighting effect" is acknowledged, the results in figure 19 suggest that the 2.5 A peak is due to a scatterer of higher atomic number than the scatterer(s) responsible for the 1.72 A peak.

In figure 20, the transforms of the nitrogenase data taken at 4 °C are shown. The major periodicity occurs at an apparent radius of 1.72 A, as was observed in the -90 °C data transforms. However, there are additional peaks at 3.62 A and 5.32 A (N_2) and 4.06 A and 4.82 A(Ar) which are not present in the transforms of the -90 °C data. There appear to be significant differences between the transforms. The k^3 transforms (fig. 21) of the 4 °C data emphasize the peaks at 3 A and beyond, although the transforms are becoming seriously distorted by noise in the data.

The interpretation of the data taken at 4 °C presents several problems. The first is that of the peaks at distances greater than 4 A. Experience with the analysis of EXAFS data from materials of known structure indicates that unless there are multiple scatterers present, the detection of scatterers beyond 4 A is not possible. It

could be proposed, knowing that a number of iron atoms are present in/ the molybdenum-iron cofactor[36], that the molybdenum in nitrogenase is in a novel cluster structure with multiple molybdenum-iron distances. This explanation fails to explain why the EXAFS of frozen and liquid solutions are different. To formulate an explanation consistent with both the -90 ^{o}C and 4 ^{o}C results, it would have to be assumed that (a) upon thawing, the molybdenum site undergoes a structural change; (b) the structure assumed upon thawing is quite unusual by EXAFS standards; and (c) molybdenum-substrate interactions which occur at 4 ^{o}C are somehow blocked in the frozen state. An alternative to the above speculations is to assume that some pathological artifact in the 4 ^{o}C data has given rise to spurious peaks at large radii. Under usual circumstances, these discrepancies would be resolved by repetition of the experiment in question. However, the present beam time situation at the Stanford Synchrotron Radiation Laboratory makes it unlikely that these experiments will be repeated in the near future.

I. Curve Fitting Analysis of Nitrogenase EXAFS

In a recently published paper, Cramer, Hodgson and co-workers[37] reported a detailed analysis of the EXAFS of a lyophilized sample of the Mo-Fe component of nitrogenase from Clostridium pasteurianum. Using a curve fitting technique for the analysis of EXAFS, these authors demonstrated that the EXAFS of nitrogenase could be adequately explained by a molybdenum environment consisting of 3 - 4 sulfurs at 2.35 A from the molybdenum, 1 - 2 sulfurs at 2.49 A and 1 - 2 irons at 2.72 A. In collaboration with Keith Hodgson, the nitrogenase EXAFS data shown in figures 16 and 17 have been analyzed using the curve fitting programs and model compound data developed by Cramer, Hodgson et al.[22,37]

In the following paragraphs, the curve fitting technique for EXAFS analysis will be briefly summarized.

In the curve fitting approach, the EXAFS envelope functions and the arguments of the sinusoids are expressed in terms of model mathematical forms. This gives a model $\chi(k)$ and the terms in equation 3, or its equivalent, effectively become a family of similar functions. Each member of this family is characterized by a limited number of constant parameters. To apply the curve fitting technique, the experimental $\chi(k)$ is numerically compared with the model $\chi(k)$. By means of a least squares procedure, the values of the constant parameters that define the model $\chi(k)$ are refined to obtain a best fit with the experimental data. Structural information, such as absorber-scatterer distances and coordination numbers, can be extracted from the optimum values of the parameters.

In practice, the envelope functions for the various scatterers and the phase shift functions for the various absorber scatterer pairs are determined either from the analysis of the EXAFS of materials of known structure[22] or by theoretical calculations.[8] In either case, amplitude and phase shift data are tested by the analysis of the EXAFS of other compounds of known structure. In this fashion, reliable amplitude and phase shift data for the analysis of EXAFS of unknown structures are accumulated, and the limits of accuracy of structure determinations with this data are defined.

In the analysis of the EXAFS of materials of unknown structure, plausible model structures are proposed based on the examination of the Fourier transform of the EXAFS and on any other physical or chemical information available about the unknown material. The EXAFS of the

unknown material is compared with the EXAFS calculated on the basis of the proposed structure, and the number of scatterers and the absorber - scatterer distances are allowed to vary to obtain a best fit. Proposed model structures are tested until a model is found that gives a good fit to the experimental EXAFS and which is consistent with other information about the unknown material.

The EXAFS data in figures 16 and 17 were fit to the sulfur-iron-sulfur model of Cramer, Hodgson and co-workers[37]. The results of the curve fitting analysis are of interest to the extent that they can be compared with the results of Cramer, Hodgson and co-workers[37], and also because the curve fitting technique may be able to detect subtle differences between the EXAFS of samples equilibrated with argon and the EXAFS of samples equilibrated with dinitrogen. The EXAFS data were fit as two data sets for each type of sample. The first was the average -90 ^{o}C EXAFS shown in figure 16. The second was the average of the data in figures 16 and 17.

Before fitting, the data in figures 16 and 17 were adjusted so that E_o would be equal to 20021 eV. This placed E_o at 14 eV above the edge inflection point energy, making the x-axis units of the EXAFS comparable to those used by Cramer, Hodgson and co-workers.[37] For curve fitting, the calculated EXAFS data were compared numerically with experimental data that had been Fourier filtered over the r space domains listed in table V. The domains were chosen so that the magnitude of the Fourier transform of the EXAFS would be near a minimum at the cut-off points.

The final fit to the S-Fe-S model was a three shell fit, in which the scatterer numbers and absorber-scatterer distances in three terms of

equation 3 were allowed to vary to produce an optimum fit.[38] The three shell fit was built up in a stepwise fashion, using one, two and three shells in succesion. As each shell was added, the scatterer numbers and distance determined in the Cramer et al.,[37] analysis were used as starting values for the optimization of the parameters of the newly added shell. After the first fit of the data to a single shell, the scatterer number and distance determined by optimization served as starting values of the first shell number and distance to be optimized in the two shell fit. In the same way, the values determined in the two shell fit served as starting values for optimization in the three shell fit.

Throughout the fiiting procedure, amplitude and phase data determined by the analysis of model compound data served as fixed parameters during optimization.[22] In any of the fits of the nitrogenase data, only the scatterer number and the distance in each shell were allowed to vary.

The results of the three shell fitting of the four data sets are presented in table VI. The original data sets, Fourier filtered EXAFS and the three shell fits are shown in figures 22 and 23. The absorber-scatterer distances listed in table VI are in good agreement with those determined by Cramer, et al.[37] There are no significant differences between the absorber-scatterer distances determined for samples equilibrated with argon and dinitrogen.

The coordination numbers determined in these fits are significantly larger than those determined Cramer et al.[37] The significance of this result is questionable for two reasons. First, some difficulty has been experienced in applying empirically determined amplitude data from absorption spectra to the analysis of fluorescence mode EXAFS.[39]

Second, visual examination shows that the EXAFS data presented in this study are larger in amplitude, especially in the high k region of the data, than that presented by Cramer et al.[37] This may be a result of the lower signal - to - noise ratio of the present data. The larger amplitude in the high k regions might simply reflect the lower signal - to - noise ratio in that region of the data. It may be that the larger coordination numbers determined in the fit are a result of the optimization procedure fitting to low frequency noise contamination. Particularly suspicious is the apparent increase in the coordination numbers in the fits of the EXAFS of the argon-equilibrated samples. Examination of the Fourier transforms of the EXAFS does not suggest an increase of this magnitude in the areas under the major peaks.

In an effort to detect the possible coordination of dinitrogen to the molybdenum in nitrogenase, two types of fits with nitrogen containing shells were attempted. In the first type of fit, the third sulfur shell was replaced with a nitrogen at an estimated radius of 2.3 Å, and the coordination numbers and distances in all three shells were optimized. For both the EXAFS of the sample equilibrated with argon and that of the sample equilibrated with dinitrogen, the agreement between the data and the fit was reduced when the third shell sulfur was replaced with a nitrogen.

If the entry of nitrogen into the coordination sphere of molybdenum could be regarded as a minor perturbation of the molybdenum environment, the addition of a nitrogen shell to the existing three shell fit might produce an improved agreement between the fit and the data. Of course, if the addition of a nitrogen to the environment of the molybdenum was a very small perturbation, the precision of the data

may not be great enough for the fitting procedure to detect a measurable improvement in the fit due to the addition of a nitrogen shell.

A nitrogen shell was added to the optimum three shell S-Fe-S fits to the data on the argon equilibrated and dinitrogen equilibrated samples. The nitrogen was assumed to be at a distance of 2.3 A as a starting radius for optimization. The number and distance of S and Fe scatterers were fixed and the number and distance of N scatterers were allowed to vary to produce a best fit. For data on both the argon equilibrated and dinitrogen equilibrated samples, the addition of a nitrogen shell produced no detectable improvement in the agreeement between data and fit. Within the error limits, the optimum coordination number for nitrogen was zero.

In the data region near 9.5 A^{-1}, the Cramer et al.[37] model fits the Mo-Fe+Ar EXAFS significantly better than the Mo-Fe+N_2 data. This suggests a possible difference in the EXAFS due to the presence of substrate. Comparison of the Mo-Fe+Ar data with that presented by Cramer et al.[37] reveals dissimilarities in the 9.5 A^{-1} region. This suggests that the differences between the Mo-Fe+Ar and Mo-Fe+N_2 data sets in the 9.5 A^{-1} region may be a result of different noise contamination of the two data sets. Without confirmation by another set of data, therefore, it would be hazardous to try to interpret these differences.

J. Discussion of EXAFS Studies of Nitrogenase

Examination of the Fourier transforms of nitrogenase EXAFS does not reveal any significant change in the nearest neighbor environment of the molybdenum in nitrogenase in the presence of dinitrogen. The results of a limited curve fitting analysis of the data indicate that the presence of dinitrogen does not cause any significant change in the Mo-S or Mo-Fe distances in nitrogenase. The curve fitting analysis provides no evidence suggesting the presence of nitrogen in the coordination environment of molybdenum. Are these results sufficient evidence to rule out the possibility that dinitrogen binds to the molybdenum in nitrogenase under the conditions of this experiment? The answer to this question depends on the magnitude of the changes in the EXAFS produced by the entry of a single light atom such as a nitrogen into a coordination environment containing several atoms of heavier elements such as sulfur or iron.

In figure 24, the EXAFS of a compound where nitrogen is known to have entered the coordination environment of molybdenum is shown. In spectrum A, the EXAFS of trans bis dinitrogen(bis 1,2 diphenylphosphino ethane)Mo(0) (compound A) is shown. Spectrum B is the EXAFS of bis 1,2 diphenylphosphinoethane molybdenum tetrahydride (compound B), which is the tetrahydride analog of compound A. Spectrum C is the difference between spectra A and B. The raw data for spectra A and B were generously donated by Timothy Walker. The environment of the molybdenum in compound A consists of two nitrogens at about 2.0 A and four phosphorous atoms at about 2.45 A. The EXAFS of this compound clearly shows the beating in the EXAFS envelope that is characteristic of the superposition of two modulations of different periodicity. At

photoelectron energies of interest in the study of EXAFS, hydrogen is a weak scatterer of electrons. As a result, the EXAFS of compound B should be dominated by the contributions of the four phosphorous atoms surrounding the molybdenum. Spectrum B in figure 24, which appears to have a single major periodicity, is consistent with this idea.

The EXAFS data presented in figure 24 have an important implication for the study of molybdenum-substrate interactions in nitrogenase by the EXAFS method. Even though the molybdenum in compound A has two nitrogens as its nearest neighbors, its EXAFS is clearly dominated by the contributions of the four phosphorous atoms. In general, the entry of a light atom into the coordination environment of a metal that was surrounded by heavier atoms would produce only a small change in the EXAFS. The entry of the light atom would be most difficult to detect if the distance between it and the metal atom happened to be close to the distance between the metal and its other, heavier nearest neighbors. In that case, the peaks in the Fourier transform due to the two types of scatterers would be incompletely resolved. Although the curve fitting method can separate the contributions of scatterers whose Fourier transform peaks overlap, the detection of a light atom scatterer at the same distance as several heavier scatterers would require the analysis of a small fraction of the total modulation amplitude. This would require EXAFS data of high precision.

The results presented in a study of the EXAFS of molybdenum compounds[22] indicate that for the type of Fourier transform done in the present work, a peak in a transform due to a sulfur scatterer would be about three times as large as a peak due to a nitrogen scatterer at the same distance. This is because the backscattering amplitude function

of nitrogen decays much more quickly with increasing k than does the amplitude function for sulfur.

Suppose that a nitrogen atom entered the coordination sphere of molybdenum at nearly the same distance as the four sulfur nearest neighbors. In the Fourier transform, the peak due to the nitrogen would be about twelve times smaller than the contribution of the four sulfurs. In order to detect the peak due to the nitrogen in the Fourier transform, the magnitude of the noise in the difference spectrum would have to be less than 1/12 of the size of the 1.72 A peak in the Mo-Fe+N_2 Fourier transform. Examination of figures 18 - 21 shows that the main peak is, at best, four to five times larger than the background noise. The precision of the present EXAFS data may not be adequate to detect the presence of a single nitrogen in the environment of molybdenum in the case where the Mo-N and Mo-S distances were similar.

K. A Summary of the X-Ray Absorption Studies of Nitrogenase

In summary, neither the Fourier transform technique nor the curve fitting method for the analysis of EXAFS provides any evidence to suggest that the presence of dinitrogen in a solution of the Mo-Fe component of nitrogenase causes any perturbation of the coordination environment of the molybdenum, either by direct coordination of dinitrogen to molybdenum or by disturbing the other nearest neighbors of the molybdenum. However, if dinitrogen entered the coordination sphere of molybdenum at the same distance as the sulfur nearest neighbors, it is possible that the present EXAFS data are not sufficiently precise to detect the small change that would occur in the EXAFS under those circumstances. As a result, the possibility that N_2 binds to the molybdenum cannot be conclusively ruled out by the present data. The

presence of dinitrogen produces no significant change in the absorption edge spectrum of nitrogenase. Preliminary studies of the absorption edge spectra of a molybdenum-dinitrogen complex and its tetrahydride analog indicate that the entry of dinitrogen into the coordination environment of molybdenum produces marked changes in the edge structure. Although the extrapolation of these results to the case of nitrogenase could not be rigorously justified, the absence of any change in the nitrogenase edge structure argues against the binding of dinitrogen to the molybdenum in nitrogenase under the conditions of the measurements performed in this work.

Table I

Structural Data

Compound	Reference	Distance	R_j(A)	N_j
$Na_2MoO_4 \cdot 2H_2O$	27	Mo-O	1.77	4
K_3MoCl_6	28	Mo-Cl	2.45	6
MoO_2	29	Mo-O	2.01	6
		Mo-Mo[1]	2.51	1
		"	3.11	1
		"	3.7-3.8	6
		"	4.85	2
		"	5.16	2
		"	5.35	2
		"	5.43	2
		"	5.53	2
		"	5.61	2
		"	6.63	2
MoO_3	30	Mo-O	1.67	1
		"	1.73	1
		"	1.95	2
		"	2.25	1
		"	2.33	1
		Mo-Mo	3.44	1
		"	3.70	1
		"	3.96	1

Table I (cont'd)

Compound	Reference	Distance	R_j(A)	N_j
$Na_2Mo_2O_4cys_2 \cdot 5H_2O$	31	Mo-O	1.71	1
		"	1.91	1
		"	1.95	1
		"	2.30	1
		Mo-N	2.23	1
		Mo-S	2.49	1
		Mo-Mo	2.569	1
Mo Metal	32	Mo-Mo	2.72	8
			3.14	6
			4.44	12
			5.21	24
			5.48	8
Fe Metal	32	Fe-Fe	2.49	8
			2.87	6
			4.06	12
			4.75	24
			4.97	8

Table I (cont'd)

Explanatory Note

1. The Mo-Mo distances beyond 3.11 A were calculated by Jon Kirby. It is recgonized by the author that ther are other distances of comparable magnitude in the structures of the other compounds. The large r distances for MoO_2 were calculated in an attempt to assign the peaks in the MoO_2 transform that occur at distances beyond 3 A.

Table II

Dependence of Effective Phase Shift on E_o

E_o	Effective Phase Shifts (A) [1]			
	Mo-Mo [2] (metal foil)	Mo-Mo ($Na_2Mo_2O_4cys_2$)	Mo-O ($Na_2MoO_4 \cdot 2H_2O$)	Mo-Cl (K_3MoCl_6)
19980	0.29			
19985	0.30			
19990	0.31			
19995	0.33			
20000	0.35	0.29	0.33	0.39
20005	0.35	0.30	0.34	0.41
20010	0.38	-	0.34	0.43
20015	0.39	0.33	0.35	0.45
20020	0.41	0.34	0.36	0.47
20025	-	0.36	-	-
20030	0.44	0.36	0.39	0.50
20035	-	0.38	0.40	0.52
20040	0.48	0.39	0.40	0.53
20045	-	-	0.42	0.55
20050	-	0.41	0.43	0.57
20055	-	-	0.44	0.58
20060	-	-	0.45	-

Notes

1. Effective phase shift is defined as the difference between the crystallographic distance and the peak position in $|\phi_3(r)|$. Domain of k space data was 3 - 16 1/A. Apodization with Kaiser window #3.

Table II(cont'd)

2. The Mo-Mo distance for molybdenum foil was measured using the peak corresponding to the first shell.

Table III

Dependence of Effective Phase Shift on the Domain of k-Space Data Used

Distance	Compound	E_o	Domain	Effective Phase Shift
Mo-Mo	$Na_2Mo_2O_4cys_2$	20035	3-15	0.38
			4-15	0.38
			5-15	0.36
			6-15	0.35
			7-15	0.35
Mo-O	$Na_2MoO_4 \cdot 2H_2O$	20045	3.9-15.7	0.42
			5.2-25.7	0.40
			6.0-15.7	0.38
			7.0-15.7	0.37
			3.9-14.0	0.44
			3.9-12.0	0.45
			3.9-10.0	0.54
Mo-Cl	K_3MoCl_6	20035	2.7-15.4	0.52
			3.7-15.4	0.50
			4.7-15.4	0.48
			5.7-15.4	0.48
			6.7-15.4	0.47
			3.7-13.4	0.50
			3.7-11.4	0.51
			3.7-9.4	0.55

Table IV

Data for Calculation of Weighted Average EXAFS

Data Collection	Gas Phase	Fluorescence Channel	D_F'	Maximum Count Rate (sec^{-1}) R	seconds per point s	Niobium Filters	Weighting Factor W
3/76	Argon	F1	0.25	900	39	yes	8775
"	N_2	F1	0.27	900	34	"	8262
7/76	Helium	F1	0.14	1305	16	no	2923
	"	F2	0.25	871	16	"	3484
	"	F3	0.22	1081	16	"	3805
	N_2	F1	0.14	1305	15	"	2740
	"	F2	0.26	789	5	"	1025
	"	F3	0.18	1046	15	"	2824
10/76	Argon	F1	0.13	760	36	yes	3557
	"	F2	0.13	757	36	"	3542
	"	F3	0.15	678	36	"	3661
	N_2	F1	0.15	682	61	"	6240
	"	F2	0.16	756	66	"	7983
	"	F3	0.19	681	66	"	8539
5/77	Argon	F1	0.26	565	100	"	14690
	"	F2	0.19	671	100	"	12749
	"	F3	0.32	568	100	"	18176
	N_2	F1	0.27	593	92	"	14730
	"	F2	0.21	716	92	"	13833
	"	F3	0.36	628	92	"	20799

Table V

R-Space Fourier Filtering Domains

for Nitrogenase EXAFS Curve Fitting Analysis

Data Set	R_{min}(A)	R_{max}(A)[1]
-90 ^{o}C Fluorescence Mo-Fe+Ar	1.5	3.2
Average of -90 ^{o}C and 4 ^{o}C Fluorescence Mo-Fe+Ar	1.2	3.8
-90 ^{o} C Fluorescence Mo-Fe + N_2	1.3	3.5
Average of -90 ^{o}C and 4 ^{o}C Fluorescence Mo-Fe+N_2	1.2	3.2

1. R_{min} and R_{max} define the frequency range of the EXAFS data that was considered in doing the curve fit. A rectangular window was applied to the Fourier transforms of the EXAFS over the indicated domains. The windowed data was transformed back into k space and the curve fitting was performed on the filtered data.

Table VI

Results of Three Shell Fits to Nitrogenase EXAFS Data[1]

Data Set	Mo-S(A)[2]	Mo-Fe(A)	Mo-S'(A)	N_S[3]	N_{Fe}	$N_{S'}$	F[4]
-90 °C Mo-Fe+Ar	2.38(01)	2.70(01)	2.60(01)	6.0	4.3	7.0	0.94
Average of -90 °C and 4°C Mo-Fe+Ar	2.37(01)	2.70(01)	2.59(01)	6.4	4.3	6.9	2.079
-90 °C Mo-Fe+N_2	2.37(01)	2.72(02)	2.61(02)	4.6	2.7	3.6	1.81
Average of -90 °C and 4 °C Mo-Fe+N_2	2.37(01)	2.72(01)	2.61(02)	4.5	2.4	2.5	1.59

1. Consult references 22 and 37 of this chapter for details of the curve fitting procedure and the S-Fe-S model for the molybdenum site in nitrogenase, respectively.

2. Molybdenum-scatterer distances determined from the curve fitting procedure. Numbers in parentheses are the errors in the last two significant figures of the distances, determined by the curve fitting program.

3. Coordination numbers, determined from the c_0 and a_1 parameters (see reference 22) of the optimum fit.

4. F is the minimization function value equal to the sum of $k^6(DATA_i - FIT_i)^2$ over all the data points. F is smaller for cases of better agreement between the data and the optimum fit.

References

1. L.I. Schiff; Quantum Mechanics, 3rd edition, McGraw Hill Co., N.Y.(1968), 420.

2. E.A. Stern; Phys. Rev. B(1974)10, 3027 - 3037.

3. R.L. DeKronig; Z. Phys.(1931)70, 317 - 324.

4. C. Ashley; Stanford Synchrotron Radiation Laboratory Report 74/01, (1971).

5. P.A. Lee and J.B. Pendry; Phys. Rev. B(1975)11, 2975 - 2811.

6. B.M. Kincaid and P. Eisenberger; Phys. Rev. Lett.(1975)22, 1361 - 1364.

7. R.G. Shulman, P. Eisenberger, W.E. Blumberg and N.A. Stombaugh; Proc. Nat'l. Acad. Sci.-USA(1975)72, 4003 - 4007.

8. P.A. Lee and G. Beni; Phys. Rev. B(1977)15, 2862 - 2883.

9. E.A. Stern, D.E. Sayers and F.W. Lytle; Phys. Rev. B(1975)11, 4863 - 4846.

10. P.H. Citrin,P. Eisenberger and B.M. Kincaid; Phys. Rev. Lett.(1976) 36, 1346 - 1349.

11. P.A. Lee, B-K. Teo and A.L. Simon; J. Am. Chem. Soc.(1977)99, 3856 - 3859.

12. B-K. Teo, P. Eisenberger and B.M. Kincaid; J. Am. Chem. Soc. (1978) 100, 1735 - 1734.

13. B-K. Teo, P.A. Lee, A.L. Simons, P. Eisenberger and B.M. Kincaid; J. Am. Chem. Soc.(1977)99, 3854 - 3856.

14. B.M. Kincaid; Ph. D. Thesis, Stanford University(1975).

15. J. Kirby; Lawrence Berkeley Laboratory Report UCID - 3952(1977).

16. A. Robertson; Ph. D. Thesis, Univ. of California, in preparation.

17. J. Jaklevic, J.A. Kirby, M.P. Klein, A.S. Robertson, G.S. Brown and P. Eisenberger; Solid State Commun.(1977)23, 679 - 682.

18. W.H. McMaster, N. Kerr Del Grande, J.H. Mallett and J.H. Hubbel; Compilations of X-Ray Cross Sections, UCRL 50174, Sec. II, Rev. I National Technical Information Service, Springfield Va. (1969).

19. S.P. Cramer, T.K. Eccles, F. Kutzler, K.O. Hodgson and S. Doniach; J. Am. Chem. Soc.(1976)98, 8059 - 8069.

Refererences (Cont'd)

20. F.W. Lytle; Private communication.

21. R.G. Shulman, Y. Yafet, P. Eisenberger and W.E. Blumberg; Proc. Nat'l. Acad. Sci. - USA(1976)73, 1384 - 1388.

22. S.P. Cramer, K.O. Hodgson, E.I. Stiefel and W.E. Newton; J. Am. Chem. Soc.(1978)100, 2748 - 2761.

23. G. Martens, P. Rabe, N. Schwentner and A. Werner; Phys. Rev. B (1978)17, 1481 - 1488.

24. T.C. Farrar and E.D. Becker; Pulse and Fourier Transform NMR, Academic Press, N.Y.(1971).

25. T.M. Hayes, P.N. Sen and S.H. Hunter; J. Phys. C: Solid State Phys.(1976)9, 4357 - 4364.

26. J.F. Kaiser; System Analysis by Digital Computer, F.F. Kuo and J.F. Kaiser; eds., J. Wiley and Sons Inc., N.Y. (1966).

27. K. Matsumoto, A. Kobayashi and Y. Sasaki; Bull. Chem. Soc. Jap. (1975)48, 1009 - 1013.

28. Z. Amilius, B. VanLaar and H.M. Rietveld; Acta Cryst. (1969)B25, 400 - 402.

29. B.J. Brandt and A.C. Skapski; Acta Chem. Scand.(1967)21, 661 - 672.

30. L. Khilborg; Arkiv Fur Kemi(1963)21, 357 - 364.

31. J.R. Knox and L.K. Prout; Acta Cryst.(1969)B25, 1857 - 1866.

32. C. Kittel; Intro. to Solid State Physics, 4th ed., J. Wiley and Sons, N.Y.(1971) 38 - 39.

33. P.D. Wilson and T.H. Edwards; Appl. Spect. Rev.(1976)12, 1 - 81.

34. J.A. Kirby; unpublished observations.

35. The Fourier transform of the EXAFS of $Na_2Mo_2O_4 \cdot cys_2 \cdot 5H_2O$ failed to show this effect.

36. V.K. Shah and W.J. Brill; Proc. Nat'l. Acad. Sci.-USA(1977), 3249 - 3253.

37. S.P. Cramer, K.O. Hodgson, W.O. Gillum and L. Mortenson; J. Am. Chem. Soc.(1978)100, 3398 - 3407.

38. In practice, the EXAFS data are fit to a model equation (see reference 22) that is equivalent to, but not identical with, equation 3.

References (Cont'd)

39. K.O. Hodgson; Private communication.

Figure Captions

1. Creation of an EXAFS background function by the running average technique. The data are from the spectrum of potassium hexachloromolybdate. The range of the energy space data used for creation of the background function is shown (top), alomg with the background functions created by 1, 3, 5 and 7 succesive iterations of the running average calculation over an energy domain of 70 eV.
2. Effect of nonlinear phase shift on the appearance of $_3(r)$. Transforms are shown for simulated EXAFS, calculated according to equation 3 for an iron atom 5.25 A from the absorber. The total phase shift function was given by (k) = 10.0 - -1.5k + bk^2 where b had the following values: (a) 0.09, (b) 0.04, (c) 0.02 and (d) 0.00.
3. A family of "Kaiser" apodization windows. The window functions are multiplied by the k space EXAFS before Fourier transformation to reduce sidelobe intensity.
4. Fourier transform magnitudes of window functions, showing the attenuation of sidelobes by the use of a Kaiser window function. In the Fourier transform of actual EXAFS data, the sidelobes would be symmetrically distributed oh both sides of each structural peak.
5. Molybdenum EXAFS. The EXAFS of sodium molybdate dihydrate(E_o = 20045 eV), potassium hexachloromolybdate (E_o = 20034 eV) and molybdenum metal foil (E_o = 20012 eV) are shown. The y axis scales of the three spectra are directly comparable.
6. EXAFS of metal foils at room temperature. The EXAFS has been multiplied by k^3 to emphasize the high k regions of the data. The E_o values for Cu, Fe, and Mo are 8996, 7133 and 20012 eV resp.

7. EXAFS of molybdenum trioxide (E_0 = 20050 eV) and molybdenum dioxide (E_0 = 20035 eV).
8. EXAFS of tris(3,4 dithiotoluene)Mo(VI) (E_0 = 20034 eV) and $Na_2Mo_2O_4 \cdot cys_2 \cdot 5H_2O$ (E_0 = 20035 eV). Arbitrary y axis units.
9. Fourier transforms of EXAFS. Transform k space domain 4 - 16 A^{-1}. Apodization with Kaiser window #3.
10. Fourier transforms of molybdenum foil EXAFS. Domain = 3 - 16 A^{-1}. Apodization with Kaiser #3.
11. Fourier transforms of iron foil EXAFS. Domain = 3 - 16 A^{-1}. Apodization with Kaiser #3 window.
12. Fourier transforms of EXAFS shown in figure 8. For the molybdate-cysteine complex, the data domain was 3 - 16 A^{-1}. For the dithiotoluene EXAFS the data domain was 3 - 12 A^{-1}. Apodization with Kaiser #3 window.
13. Fourier transforms of the EXAFS of molybdenum oxides. The data domain was 3 - 16 A^{-1}. Apodization with Kaiser window #3.
14. Molybdenum K edge spectrum of a nitrogenase sample. The fluorescence data was obtained at the same time as the absorption data using a three element silicon semiconductor detector. The spectrum shown is the average of the data from the three detector channels. The fluorescence data is shown as obtained without any background removal. These spectra are the result of 4.6 hours of actual data collection time.
15. Comparison of absorption and fluorescence mode data. The large background absorption seen in figure 14 has been removed. The spectra were plotted so that the edge jumps in fluorescence and absorption mode data would be equal.

16. Average nitrogenase EXAFS collected at - 90 ^{o}C. The data are from fluorescence mode spectra. E_o = 20030 eV.
17. Nitrogenase EXAFS collected at 4 ^{o}C. E_0 = 20030 eV.
18. Fourier transforms of -90 ^{o}C nitrogenase EXAFS. Data domain is 3 - 12 A^{-1}. Apodization by Kaiser window #3.
19. Transforms of -90 ^{o}C EXAFS data weighted by k^3 before transformation. Data domain and apodization as in figure 18.
20. Fourier transforms of 4 ^{o}C nitrogenase data. Data domain is 3 - 12 A^{-1}. Apodization with Kaiser window #3.
21. Fourier transforms of 4 ^{o}C nitrogenase data weighted by k^3 before transformation. Apodization and data domain as in figure 20.
22. Curve fitting analysis of EXAFS. Solid line: Three shell fit to -90 ^{o}C EXAFS data. Dashed line: Fourier filtered EXAFS. E_o = 20021 eV. Fitting domain is 4 - 12 A^{-1}.
23. Curve fitting analysis of EXAFS. Solid line: Three shell fit to average of -90 ^{o}C and 4 ^{o}C nitrogenase EXAFS. Dashed line: Fourier filtered EXAFS data. E_o = 20021 eV. Fitting domain is 4 - 12 A^{-1}.
24. EXAFS of dinitrogen complex and its tetrahydride analog. Curve A: Molybdenum EXAFS of trans bis(1,2 diphenylphosphinoethane)Mo(0). Curve B: Molybdenum EXAFS of bis(1,2 diphenylphosphinoethane) molybdenum tetrahydride. Curve C: Difference EXAFS: Curve A minus curve B.

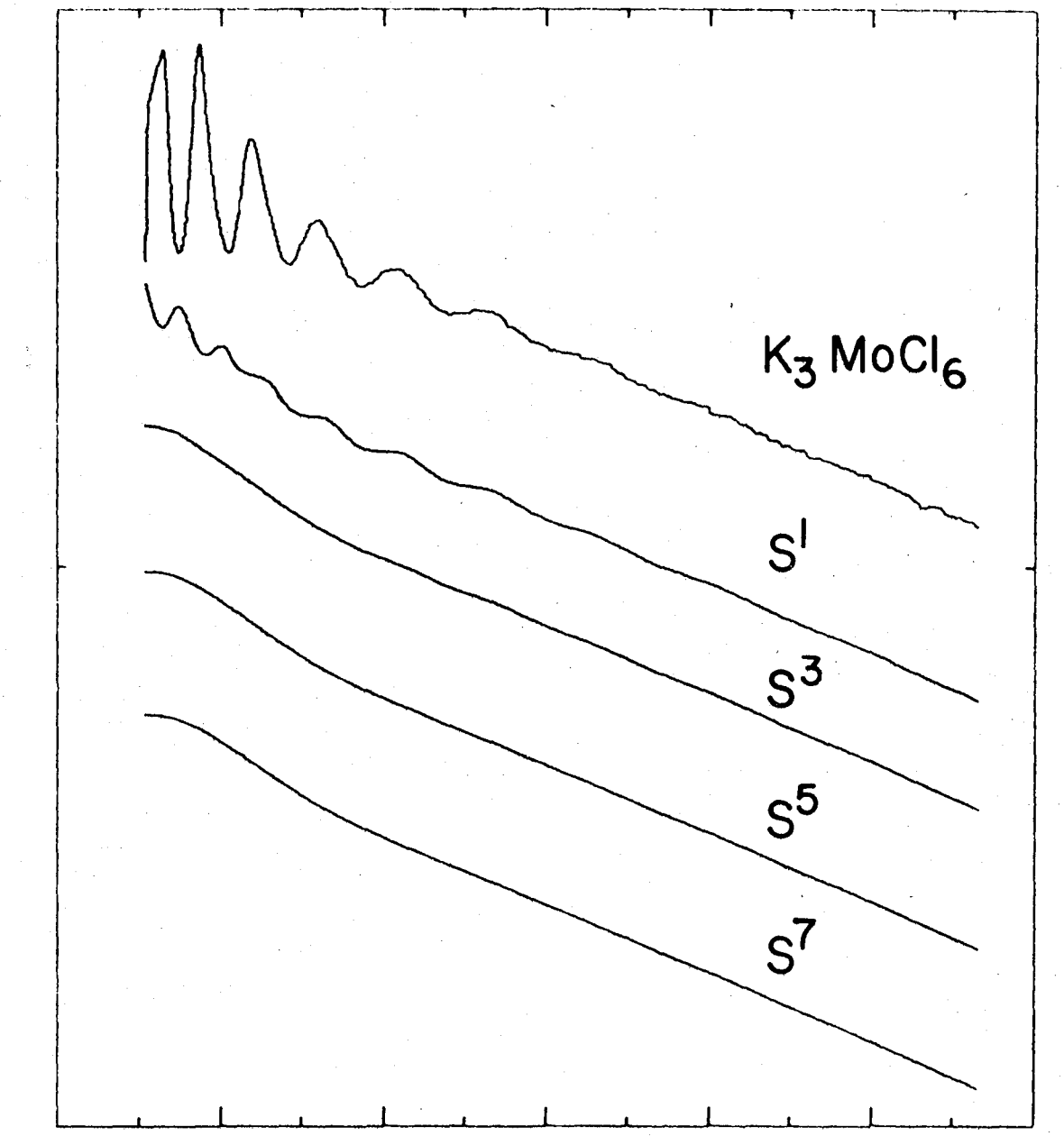

XBL 784-3954

Figure 1

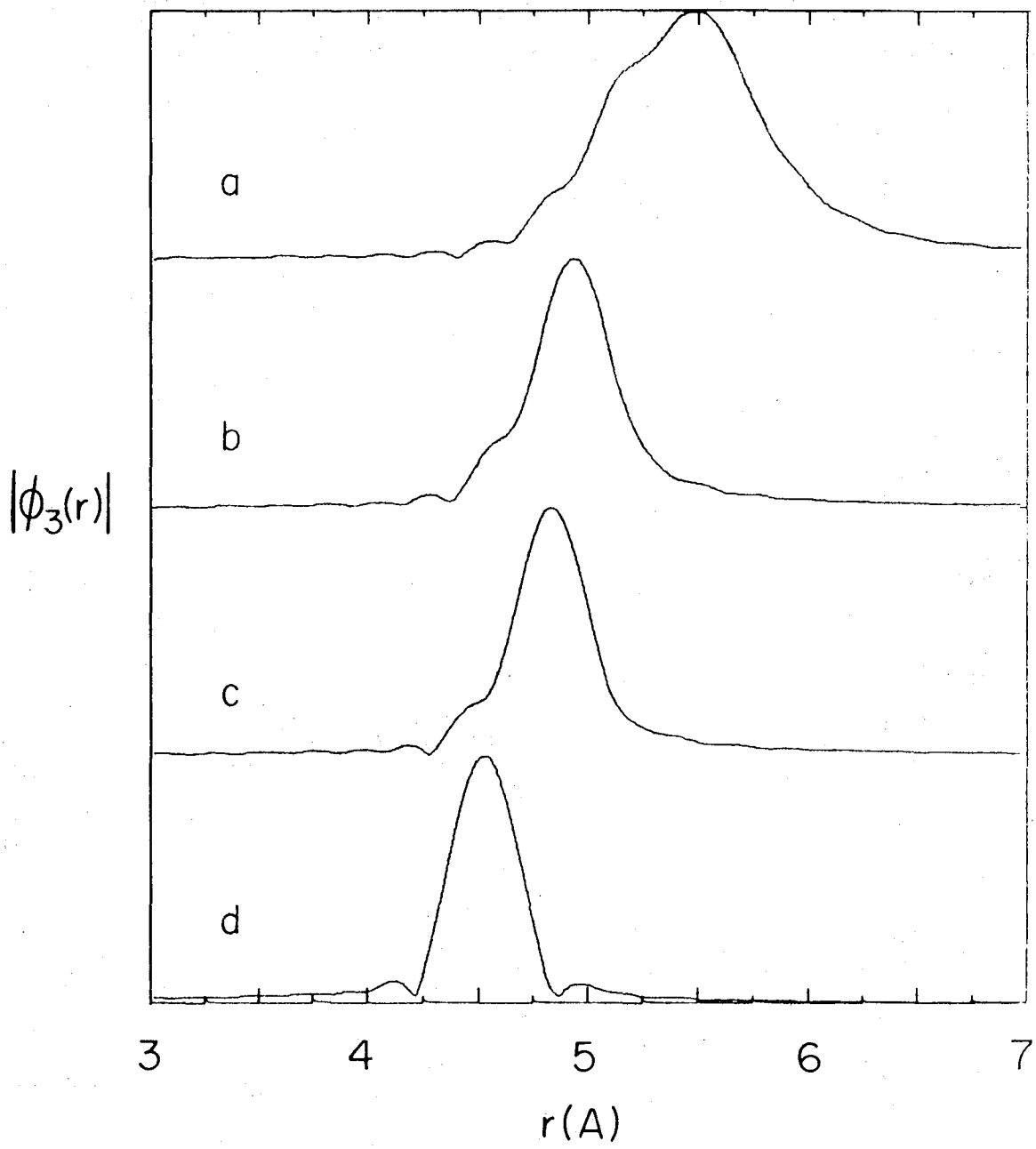

XBL 786-3976

Figure 2

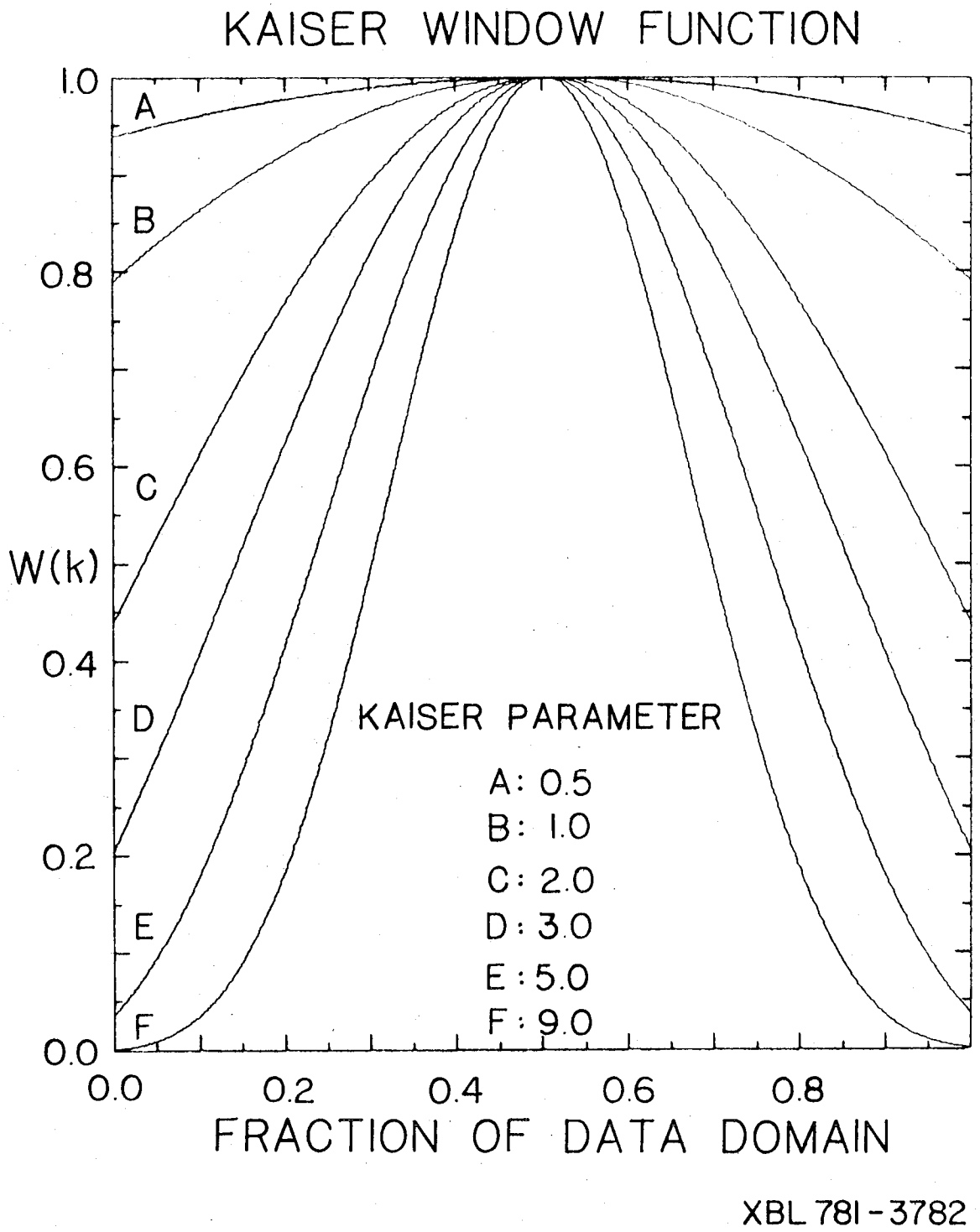
KAISER WINDOW FUNCTION
1.0
0.8
0.6
0.4
0.2
0.0
W(k)
A
B
C
D
E
F
KAISER PARAMETER
A: 0.5
B: 1.0
C: 2.0
D: 3.0
E: 5.0
F: 9.0
0.0
0.2
0.4
0.6
0.8
FRACTION OF DATA DOMAIN
XBL 781-3782

Figure 3

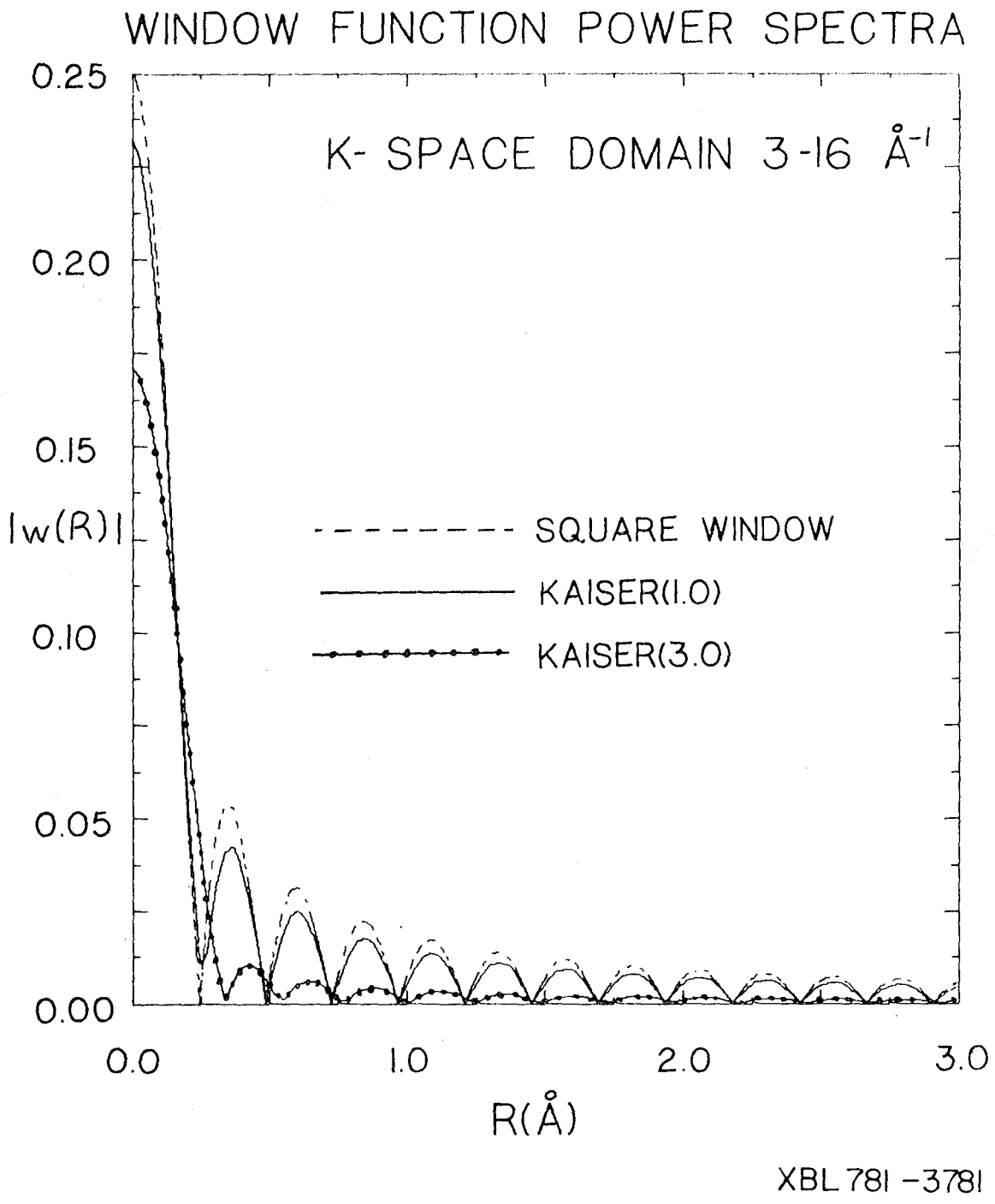
WINDOW FUNCTION POWER SPECTRA
K- SPACE DOMAIN 3-16 Å^{-1}
SQUARE WINDOW
KAISER(1.0)
KAISER(3.0)
|w(R)|
0.25
0.20
0.15
0.10
0.05
0.00
0.0
1.0
2.0
3.0
R(Å)
XBL 781 -3781

Figure 4

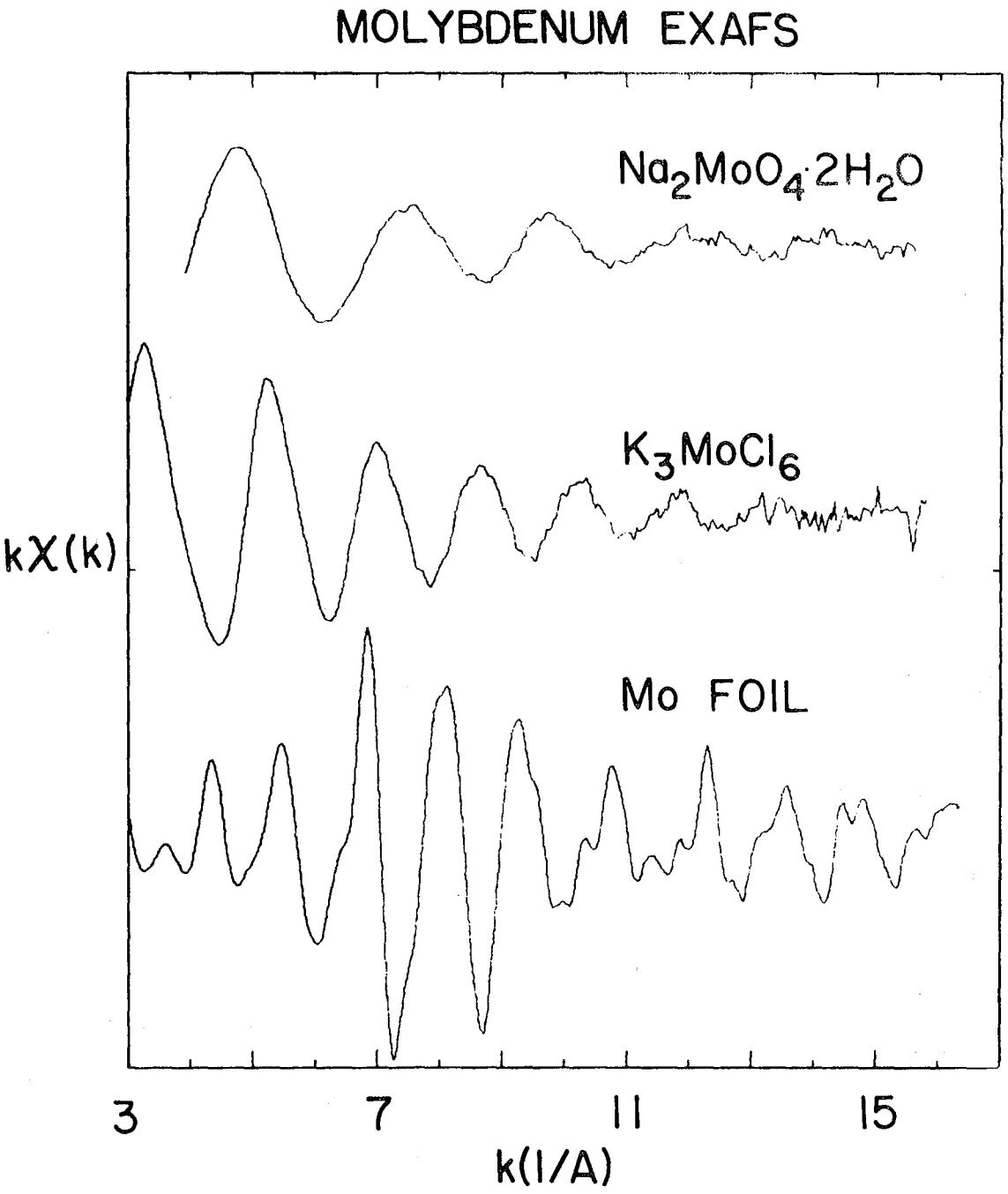
MOLYBDENUM EXAFS
$Na_2MoO_4 \cdot 2H_2O$
K_3MoCl_6
Mo FOIL
kχ(k)
3
7
11
15
k(1/A)
XBL 784-3956

Figure 5

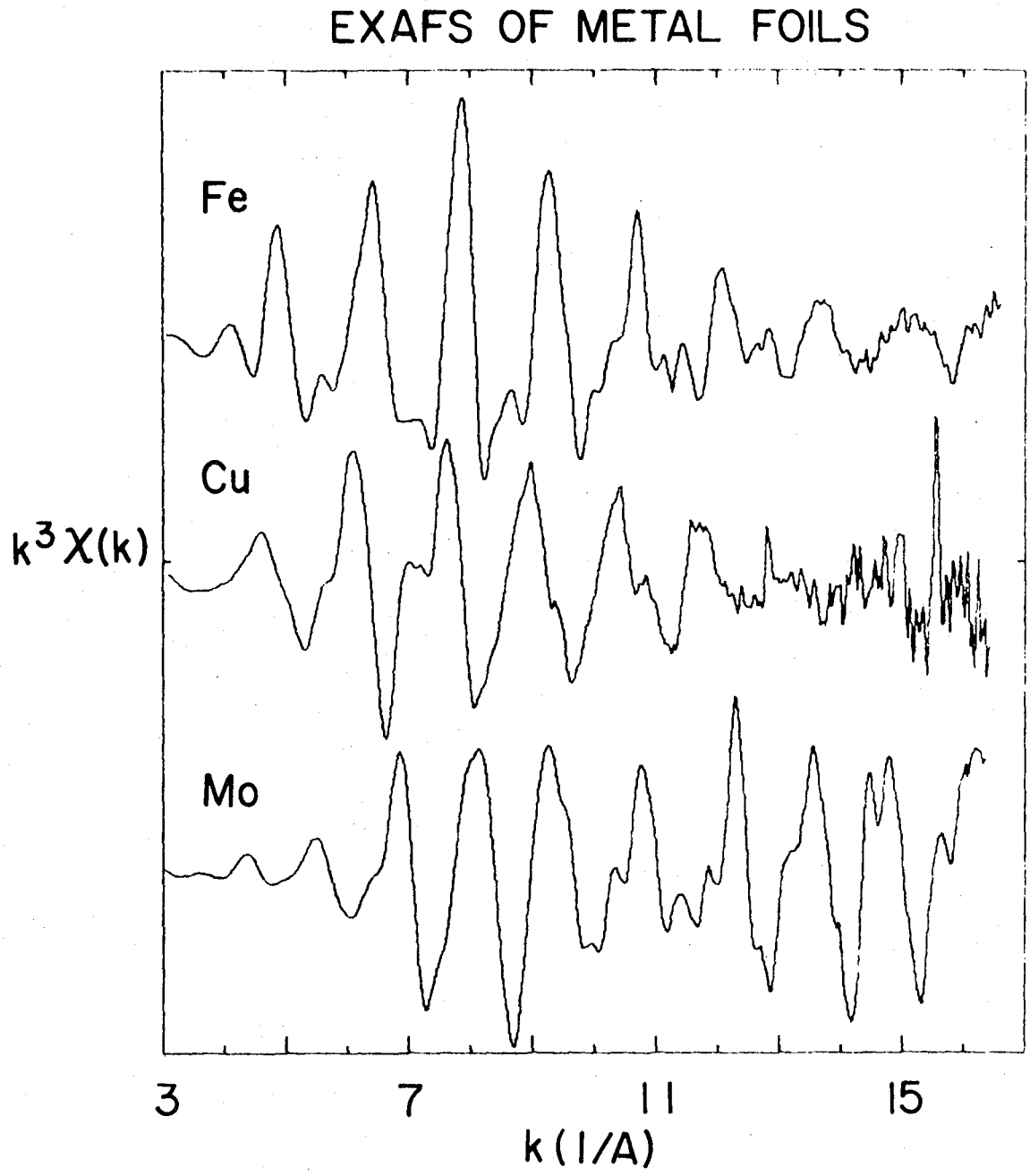

Figure 6

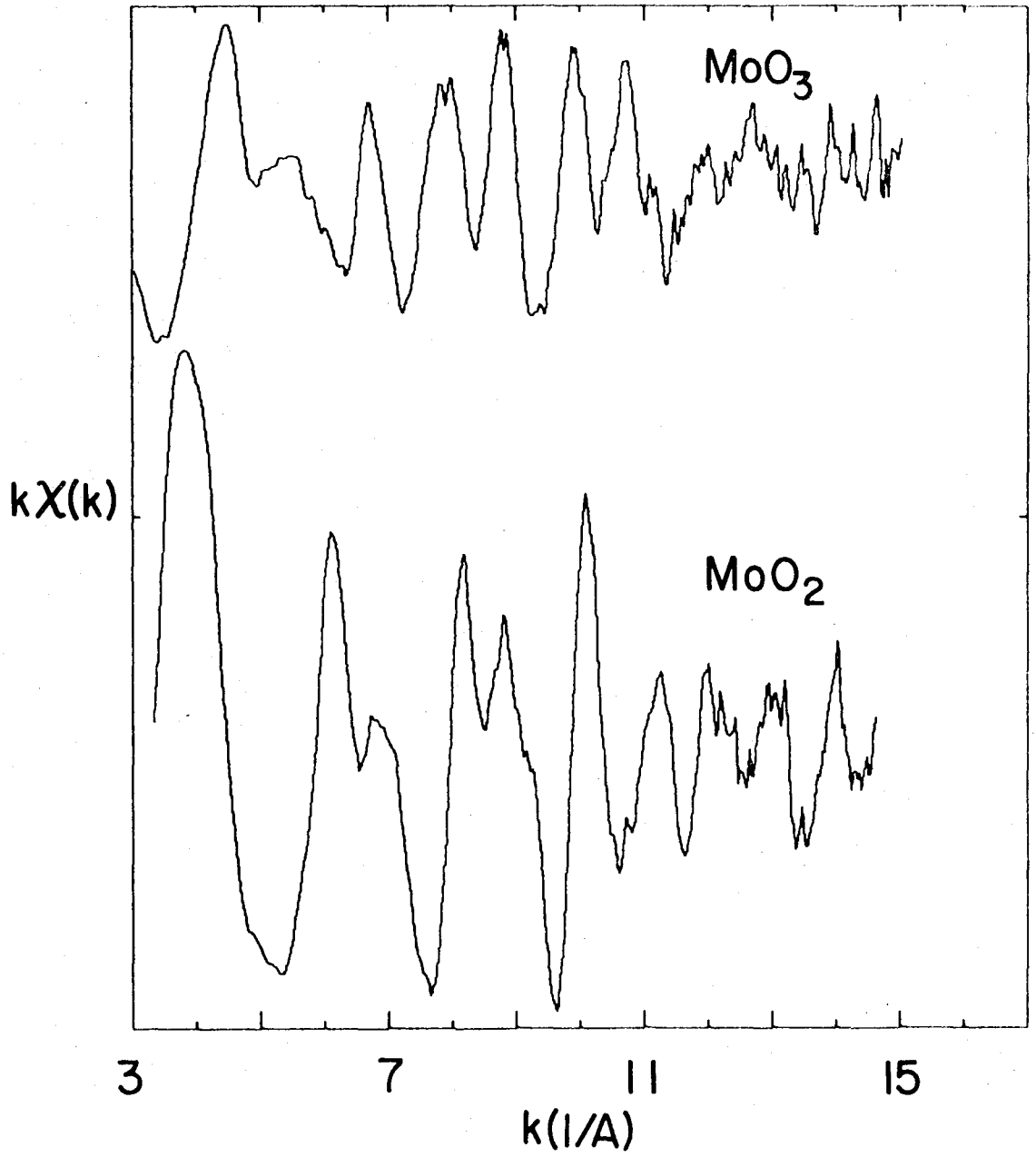

Figure 7

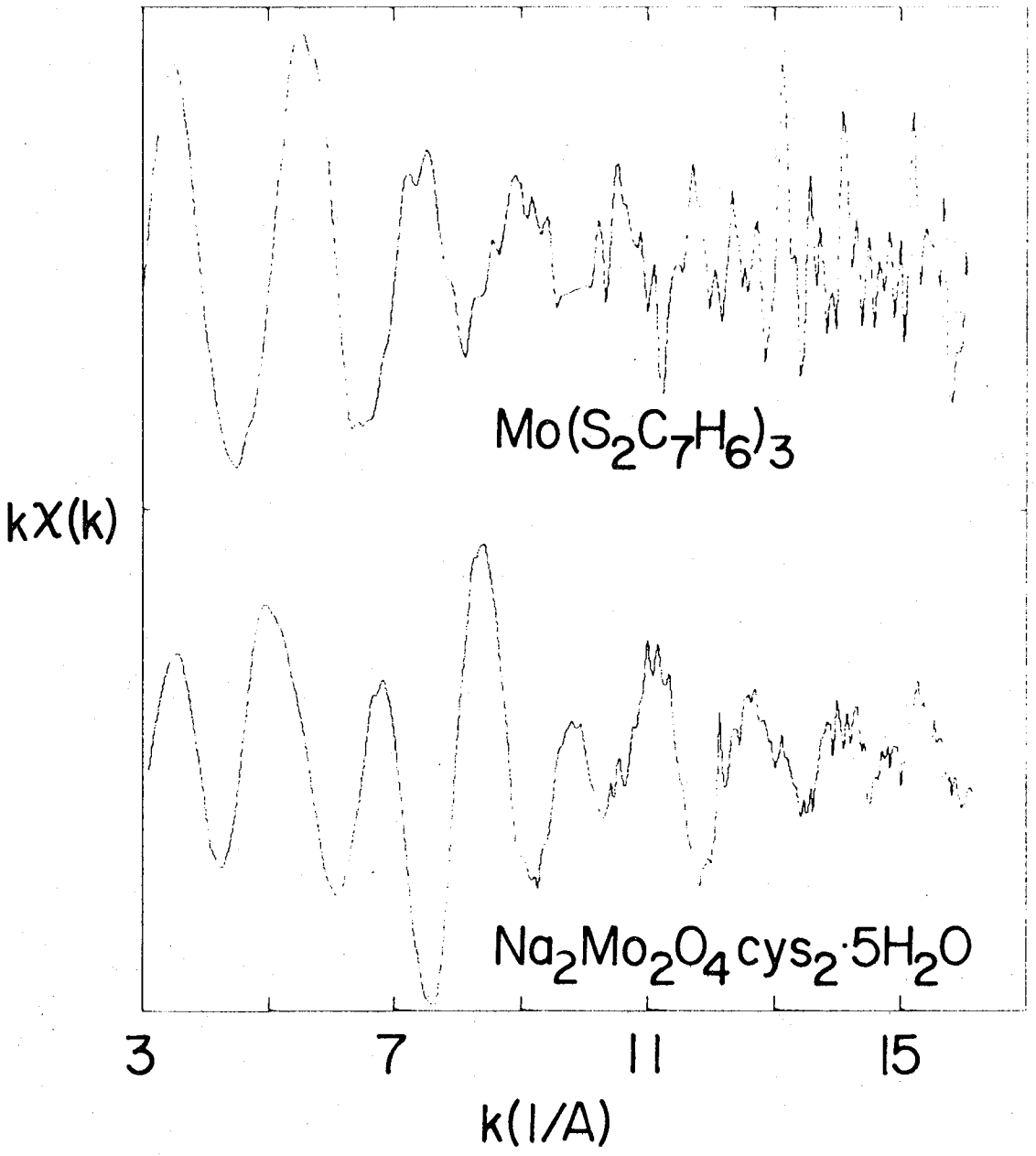

Figure 8

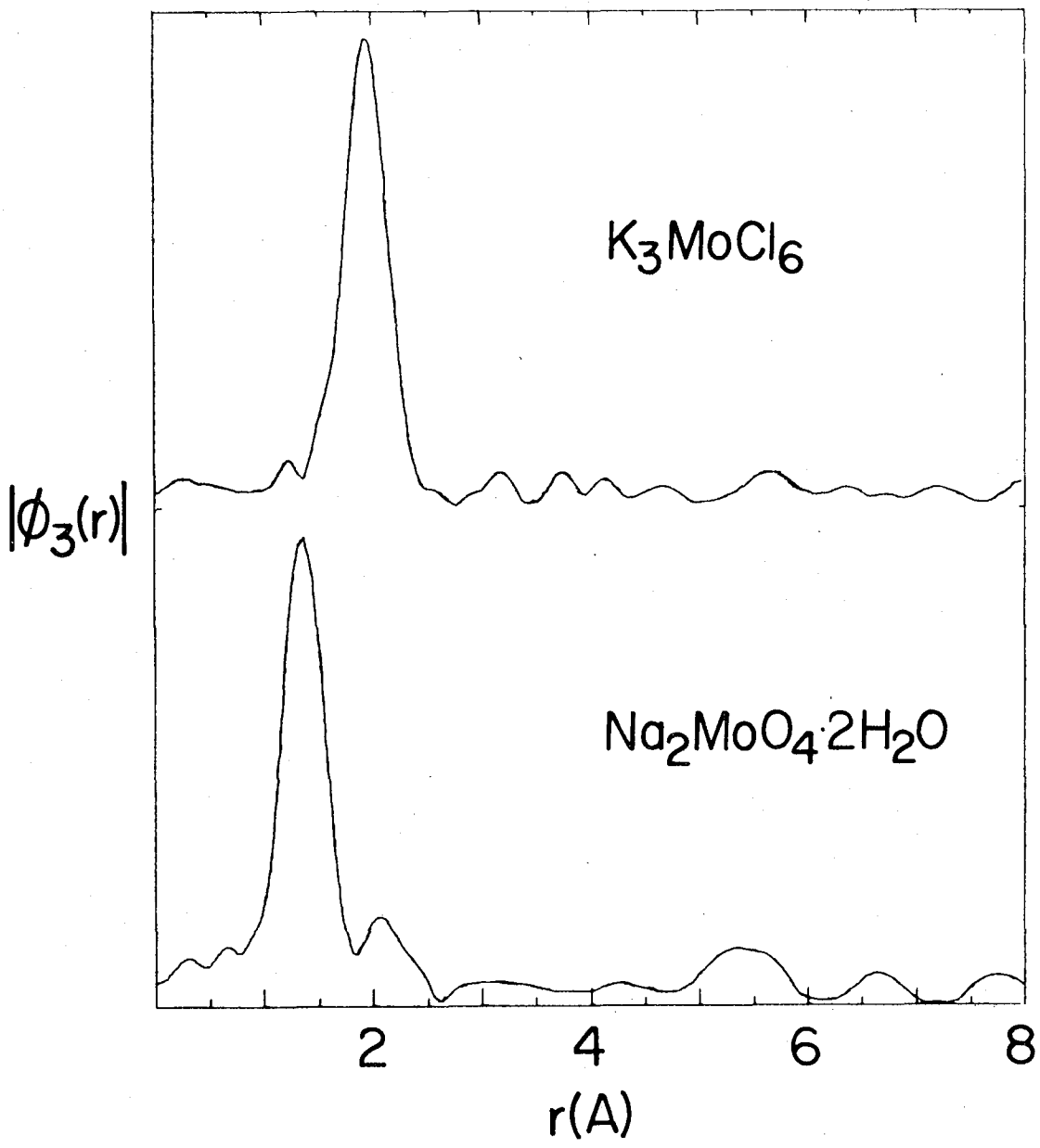

XBL 786-3994

Figure 9

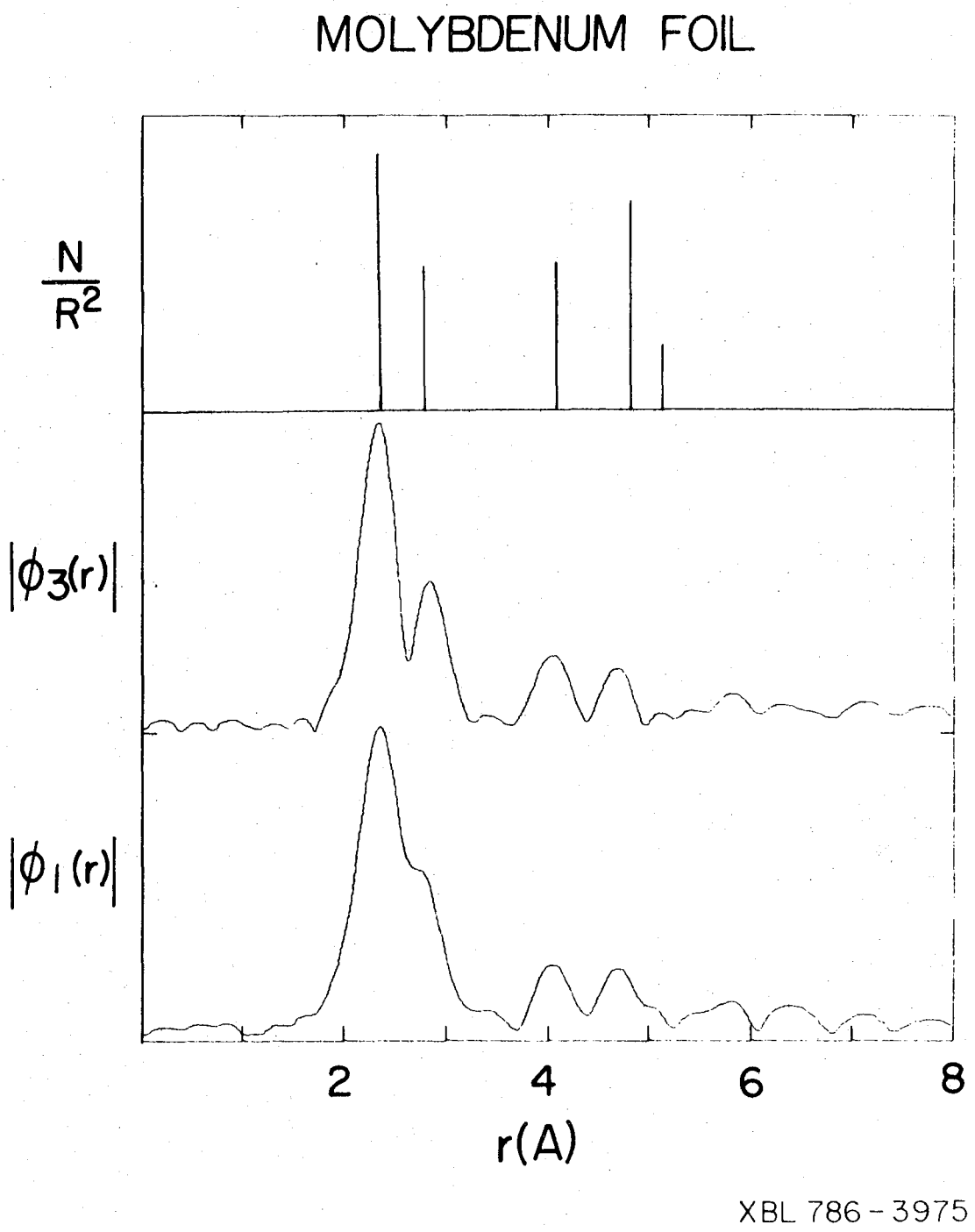

Figure 10

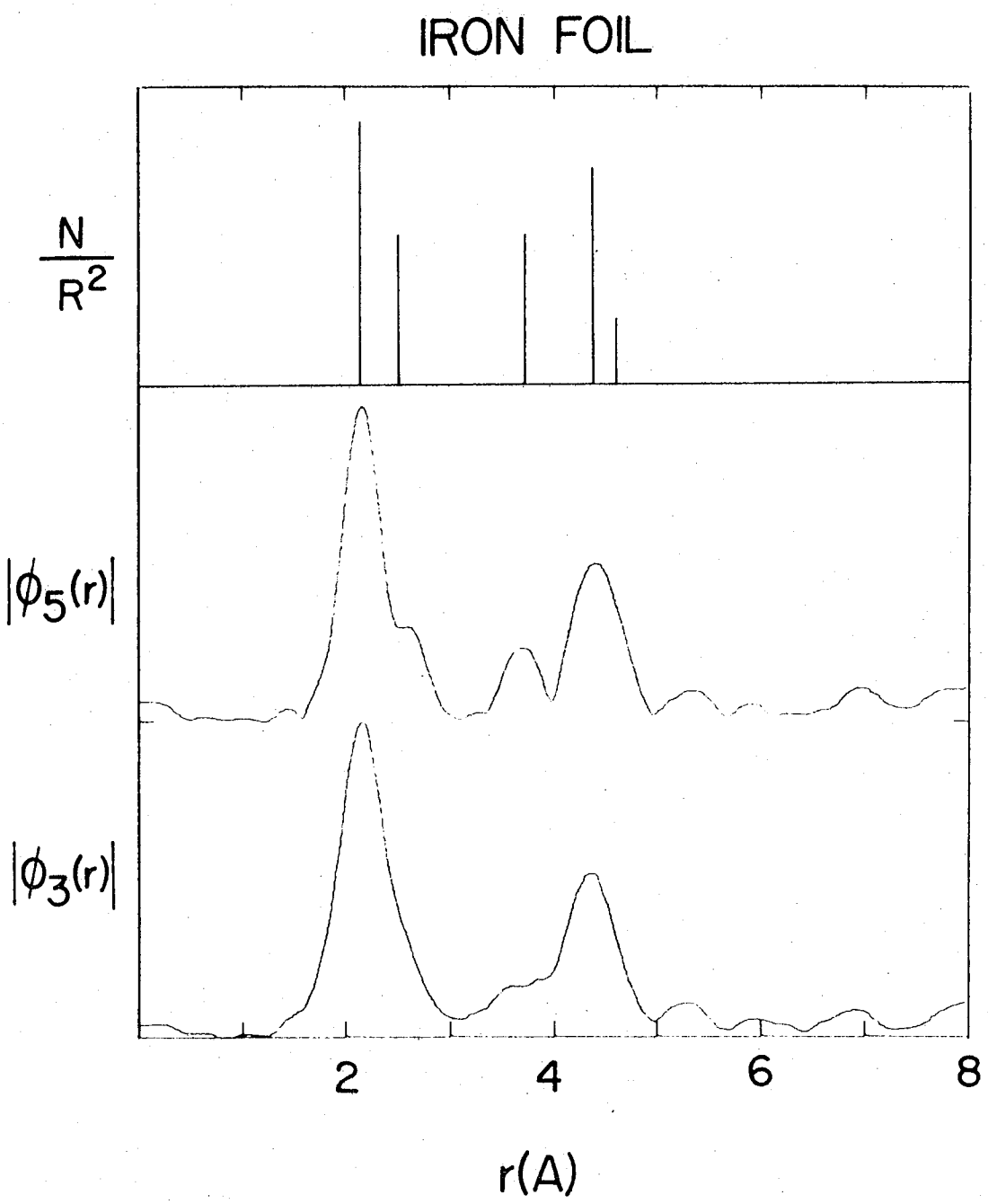

figure 11

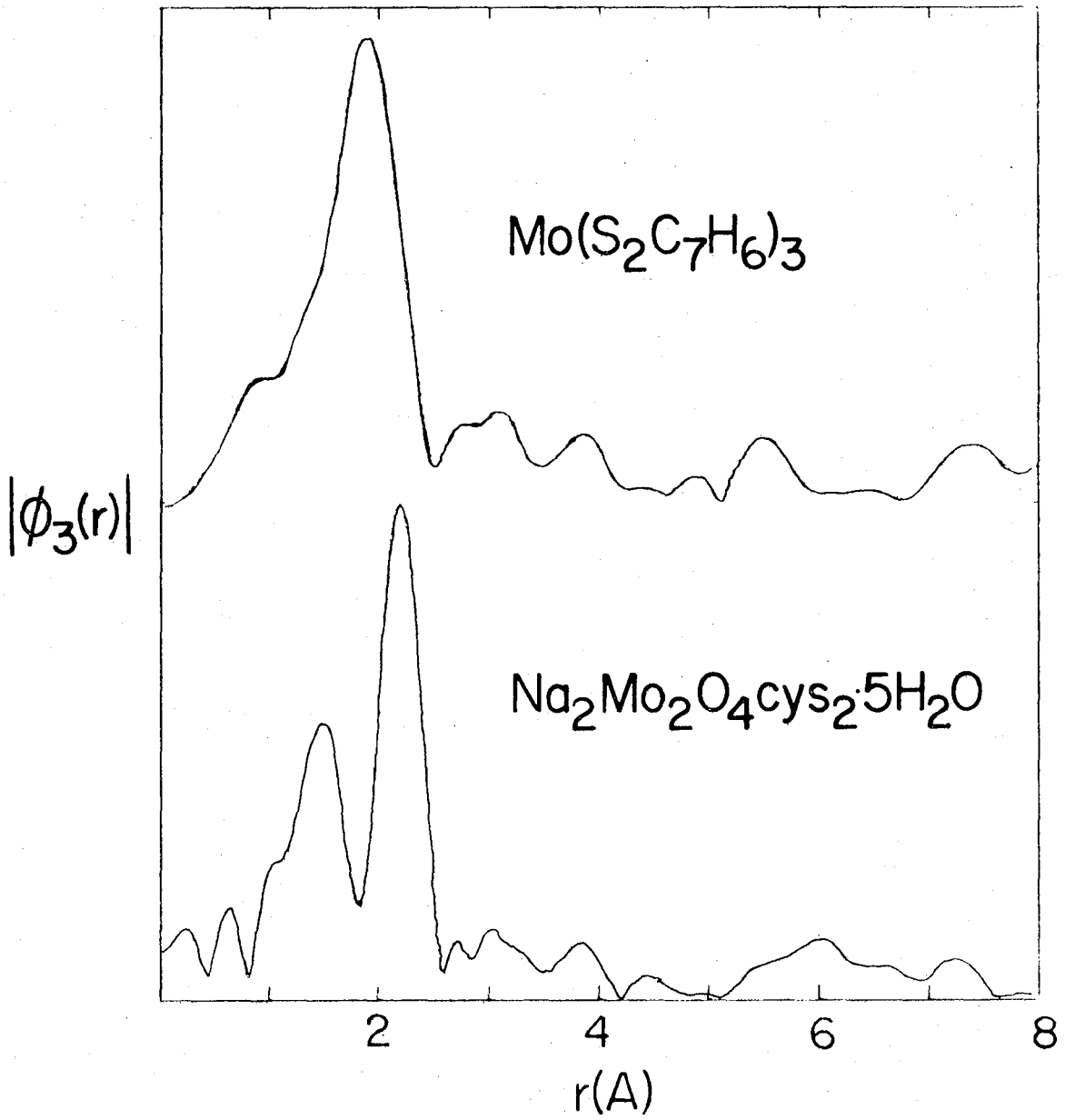

XBL 786-3991

Figure 12

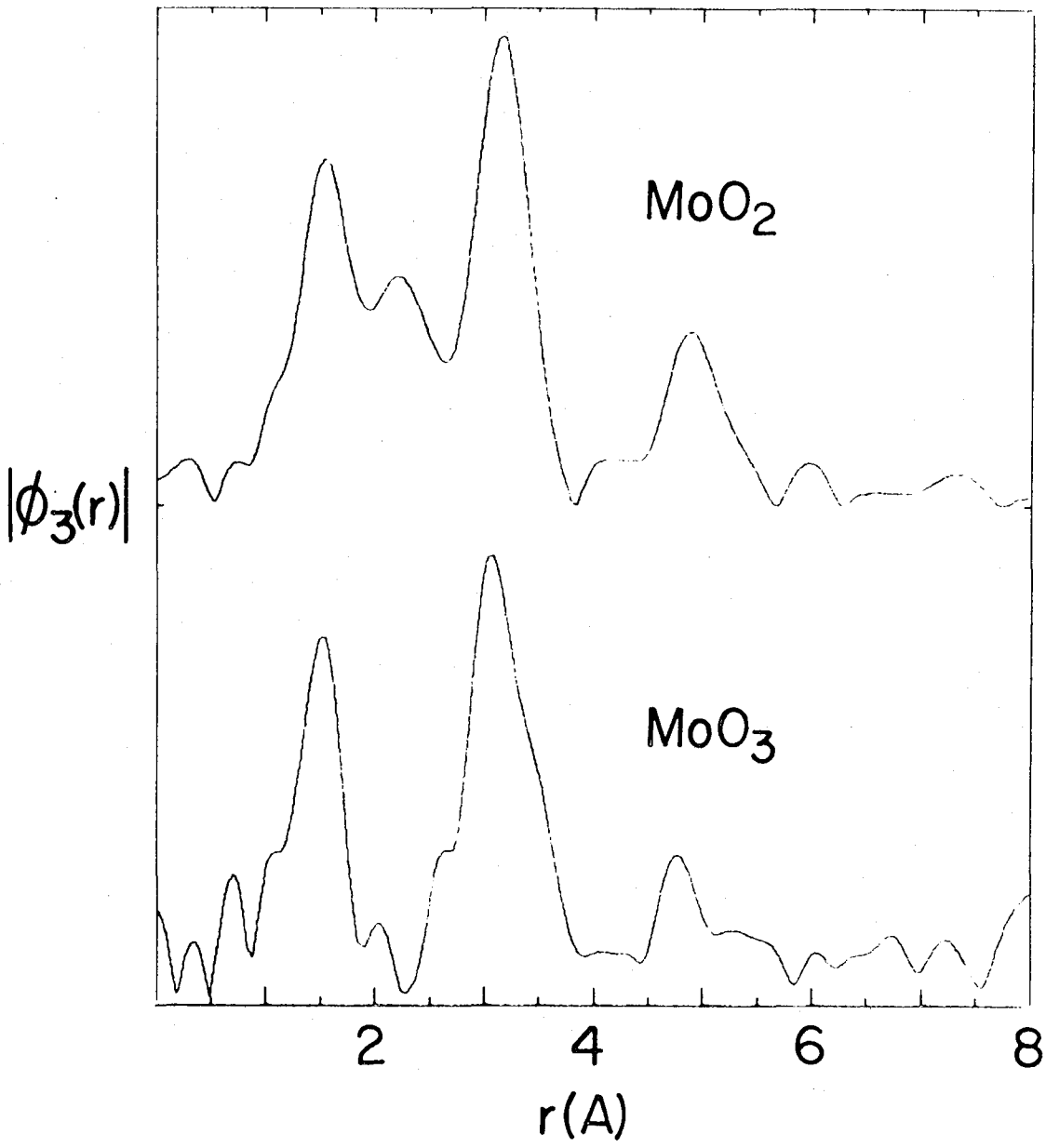

XBL 786-3996

Figure 13

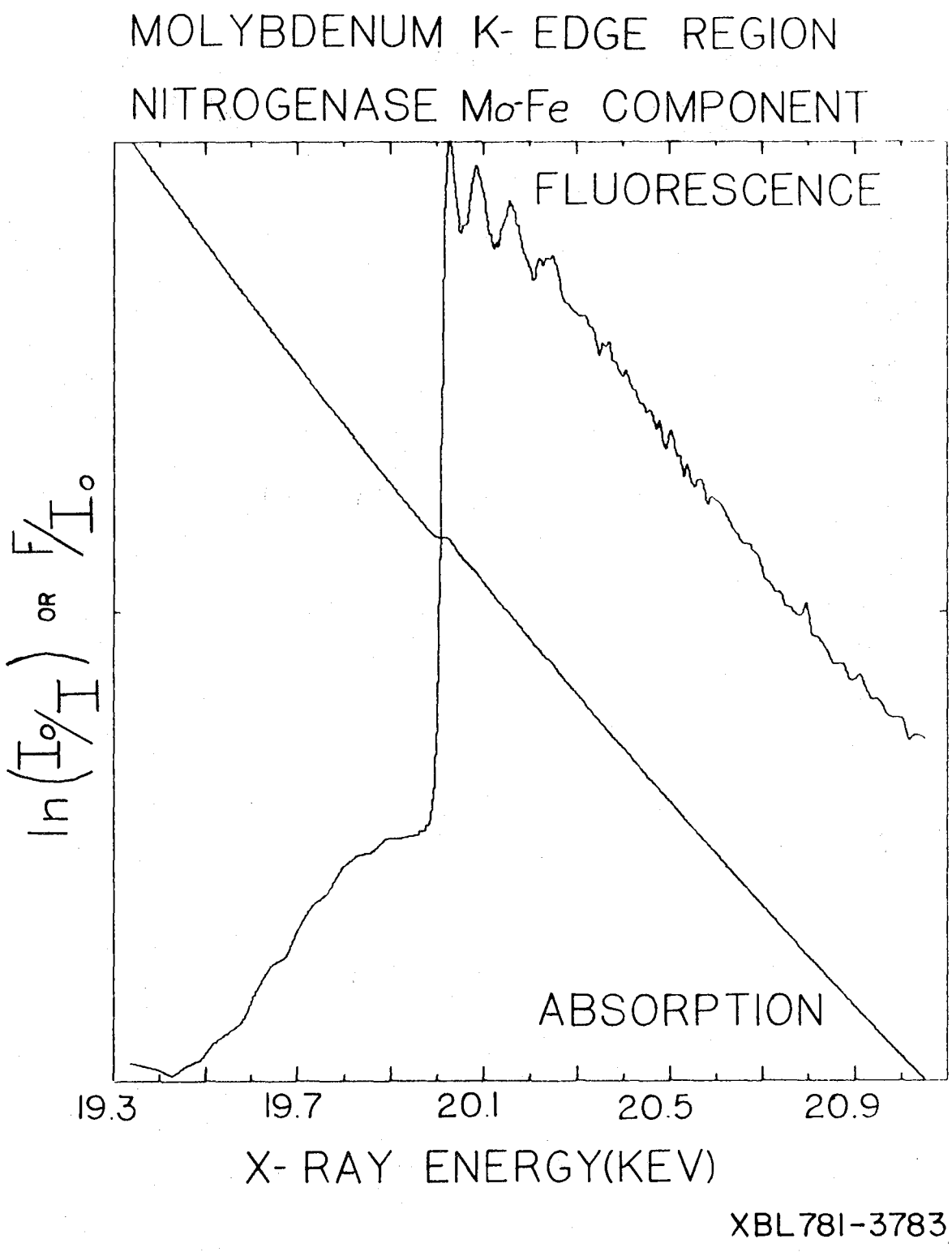
MOLYBDENUM K- EDGE REGION
NITROGENASE Mo-Fe COMPONENT
FLUORESCENCE
ABSORPTION
ln(I₀/I) OR F/I₀
19.3
19.7
20.1
20.5
20.9
X- RAY ENERGY(KEV)
XBL781-3783

Figure 14

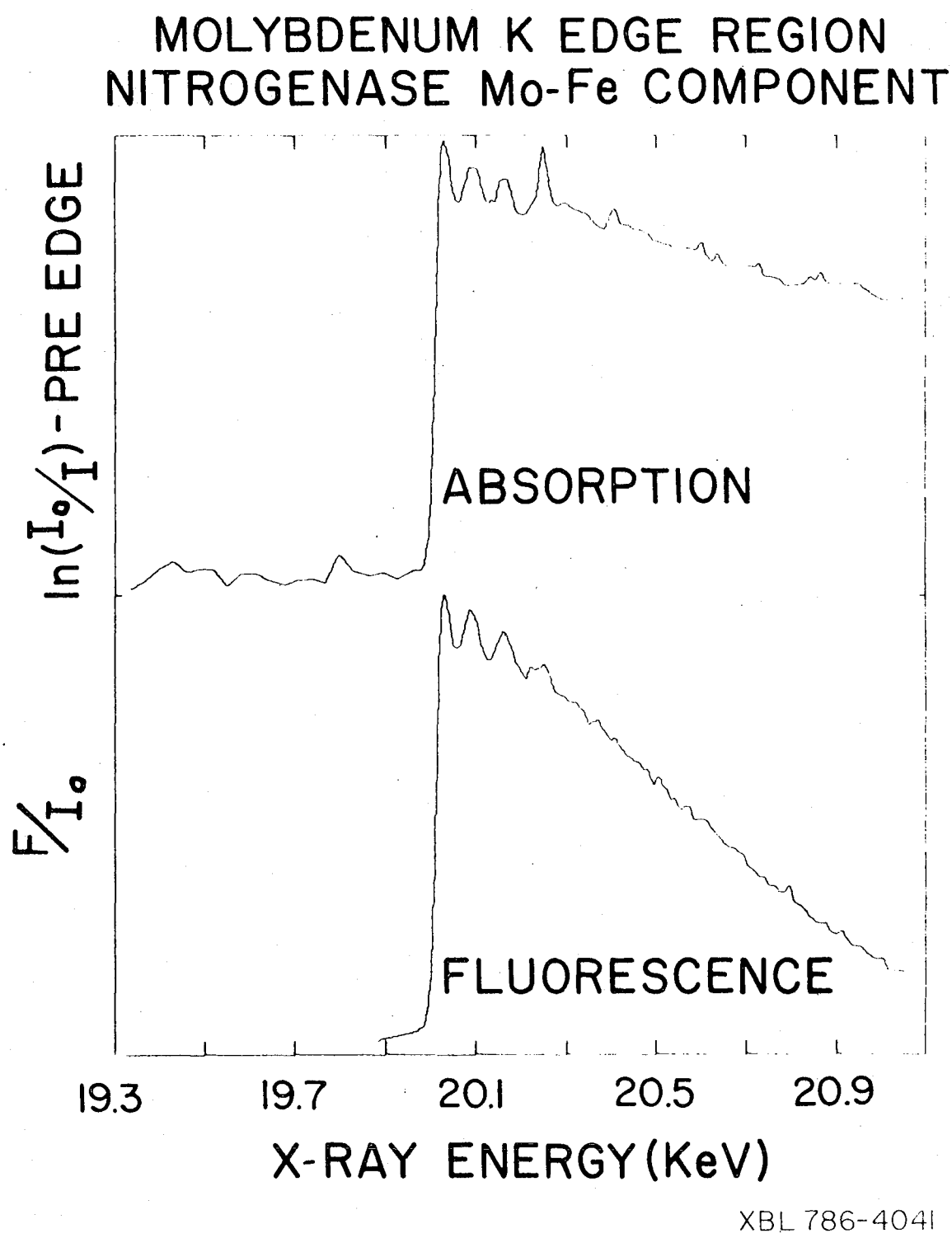
MOLYBDENUM K EDGE REGION
NITROGENASE Mo-Fe COMPONENT
ln(I₀/I)-PRE EDGE
ABSORPTION
F/I₀
FLUORESCENCE
19.3
19.7
20.1
20.5
20.9
X-RAY ENERGY(KeV)
XBL 786-4041

Figure 15

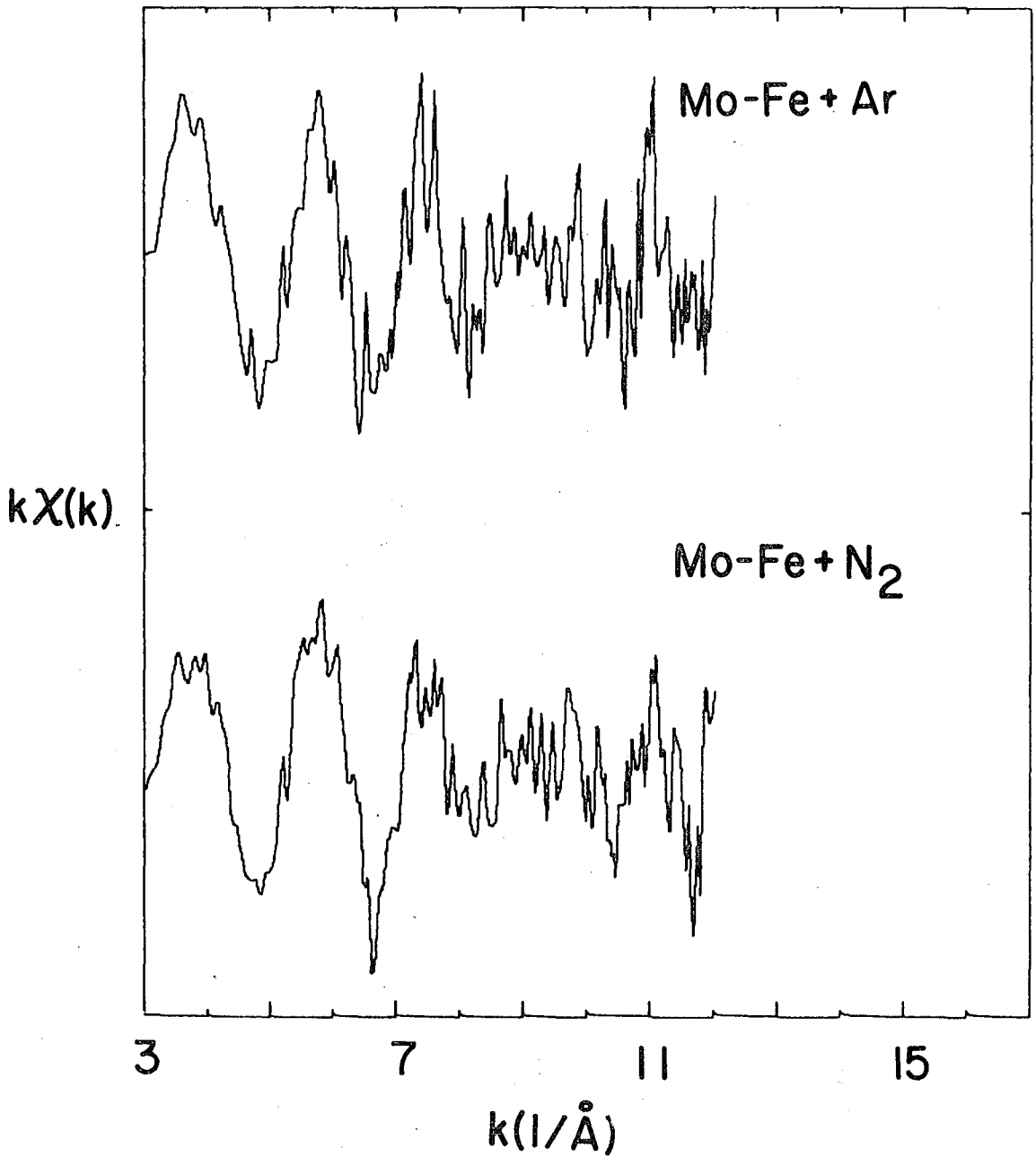

Figure 16

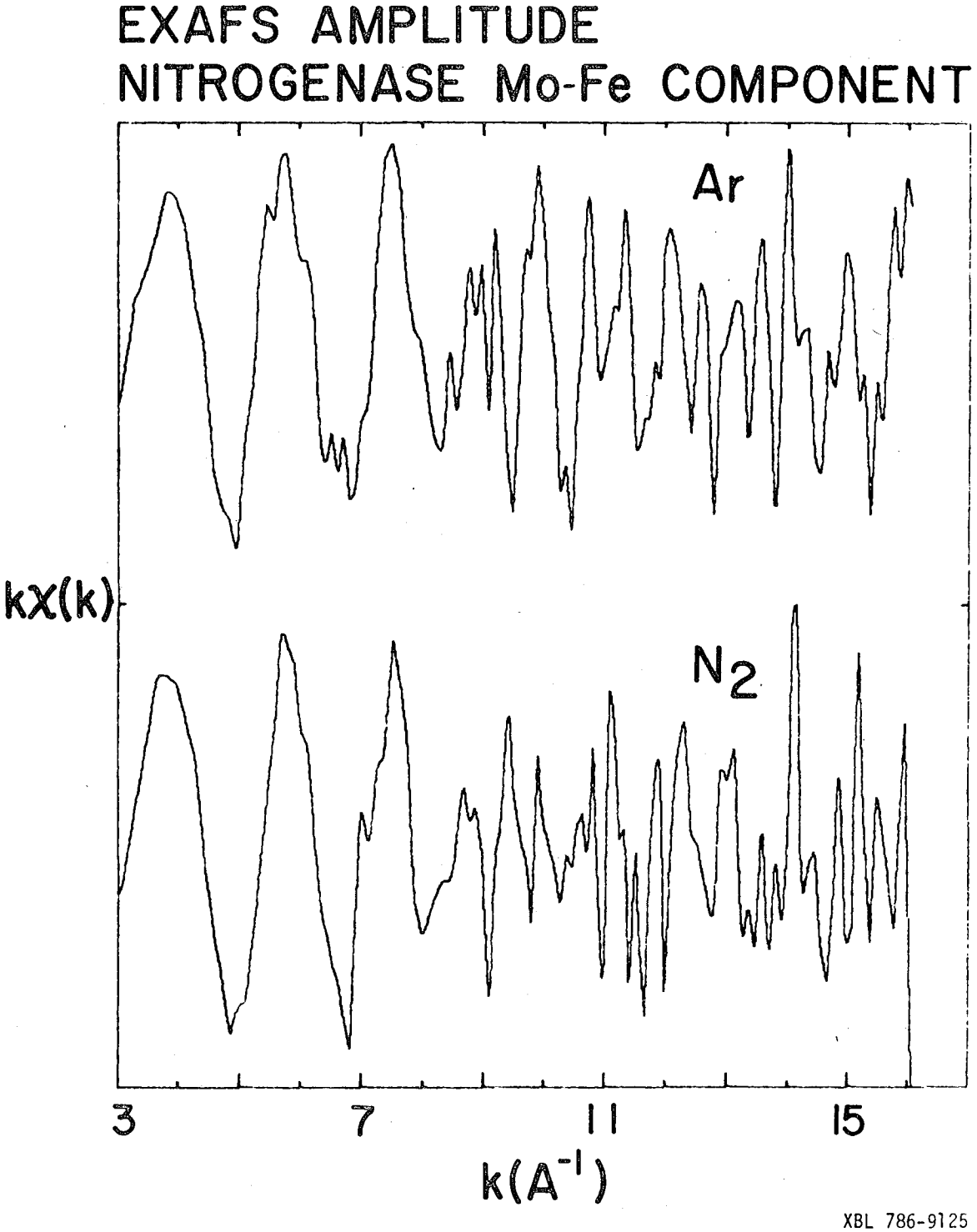
EXAFS AMPLITUDE
NITROGENASE Mo-Fe COMPONENT
Ar
N2
kχ(k)
3
7
11
15
k(A-1)
XBL 786-9125

Figure 17

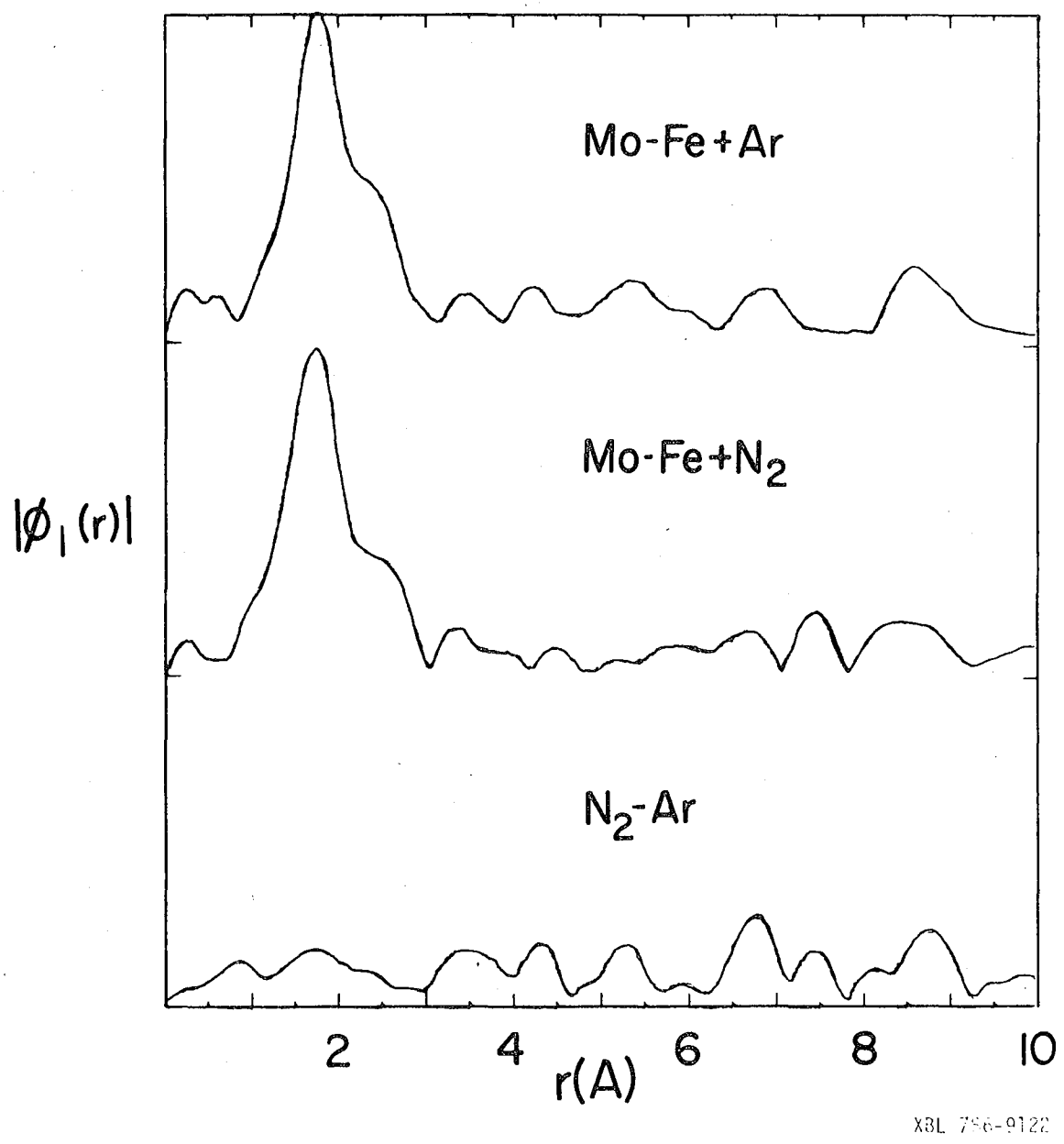

Figure 18

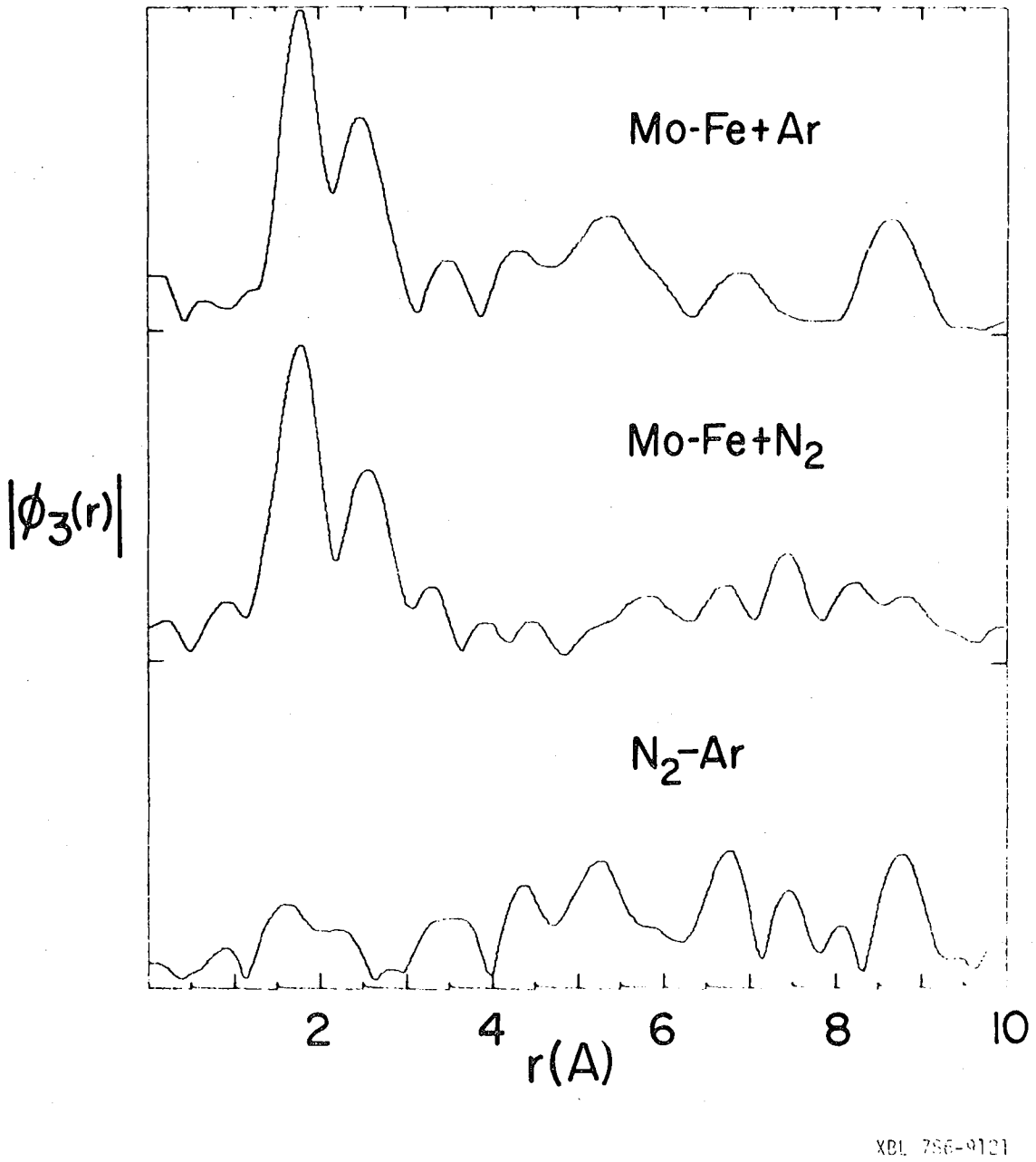

Figure 19

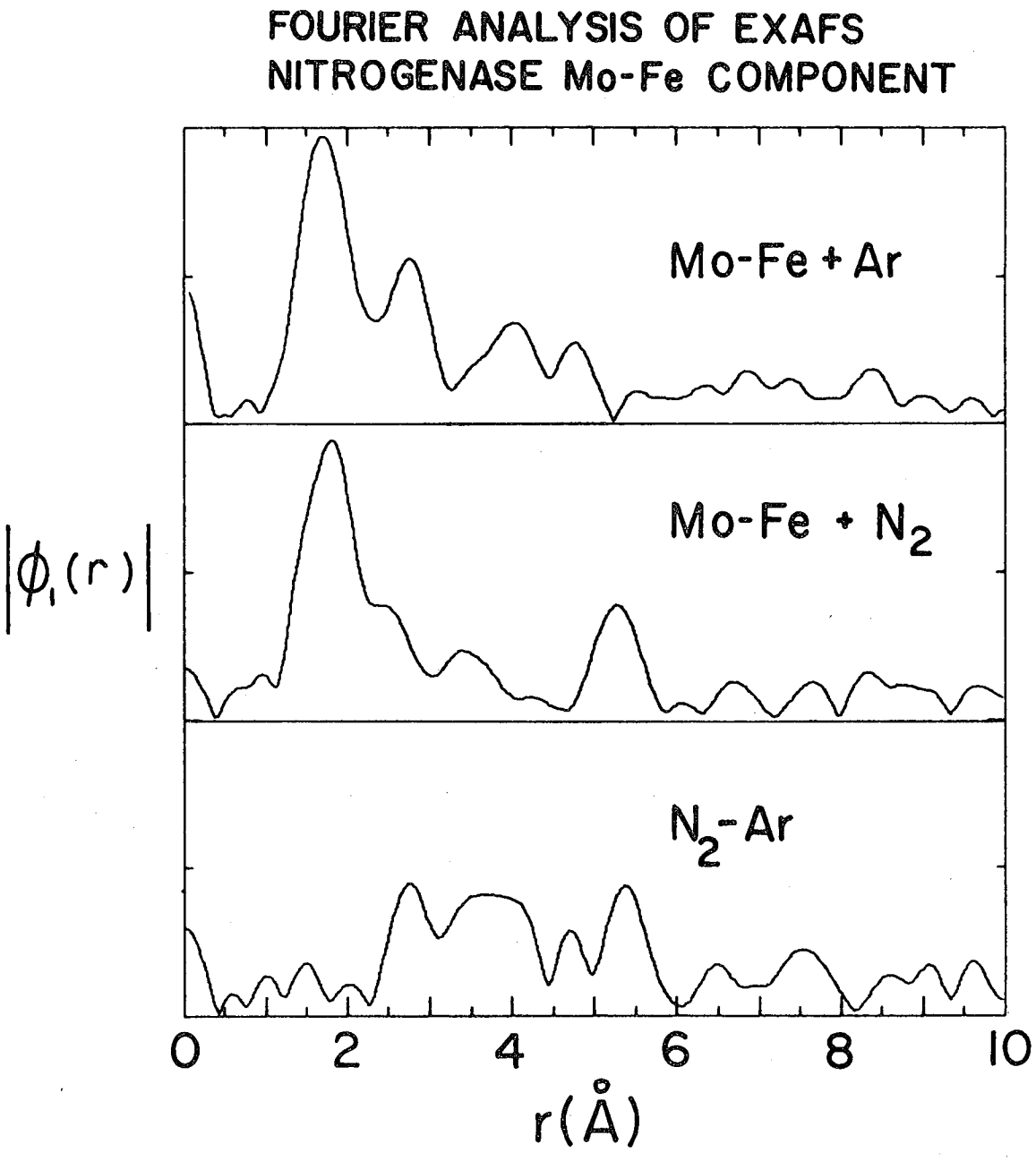
FOURIER ANALYSIS OF EXAFS
NITROGENASE Mo-Fe COMPONENT
Mo-Fe + Ar
Mo-Fe + N2
N2-Ar
|φ1(r)|
0
2
4
6
8
10
r(Å)
XBL783-3855

Figure 20

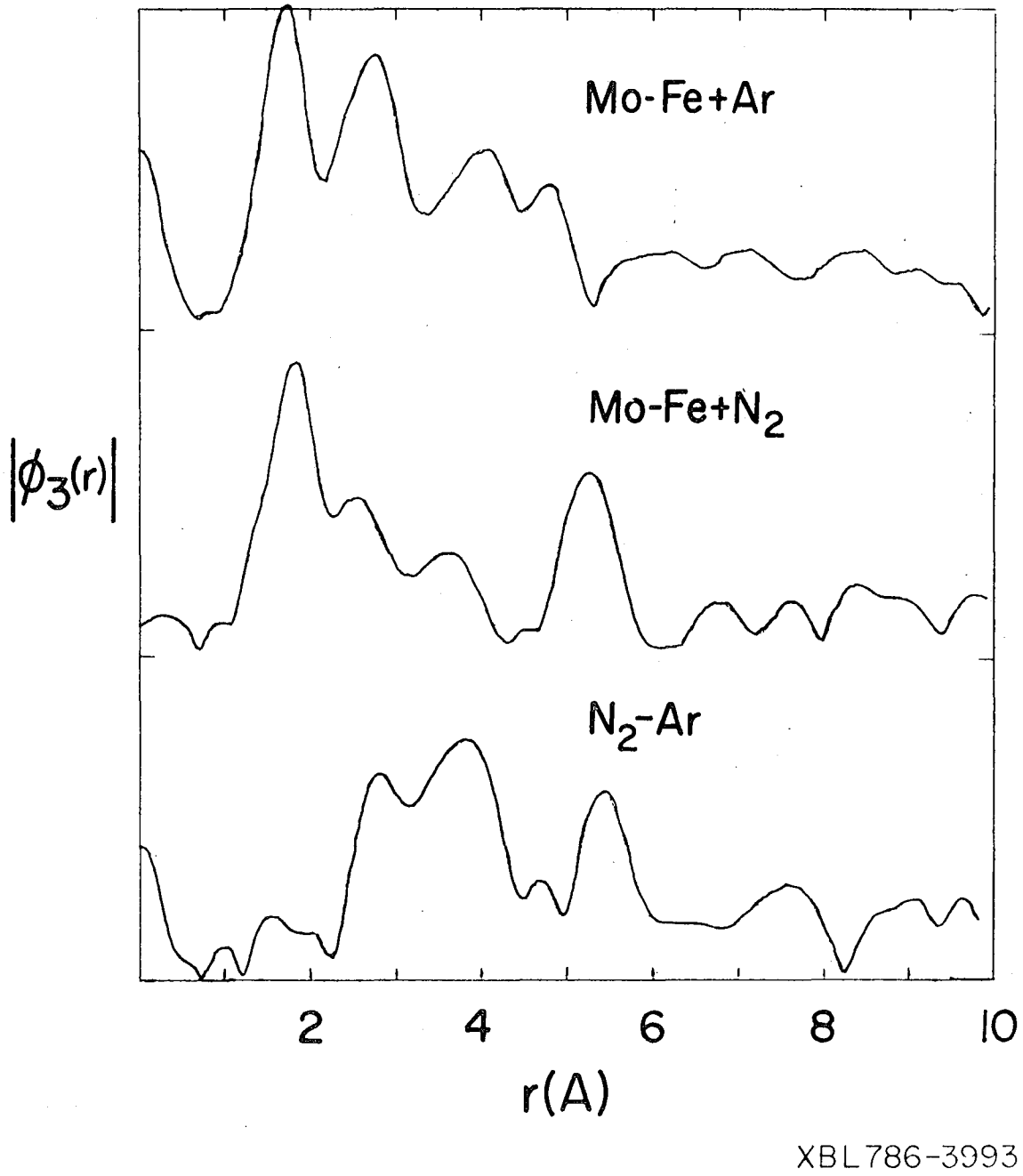

Figure 21

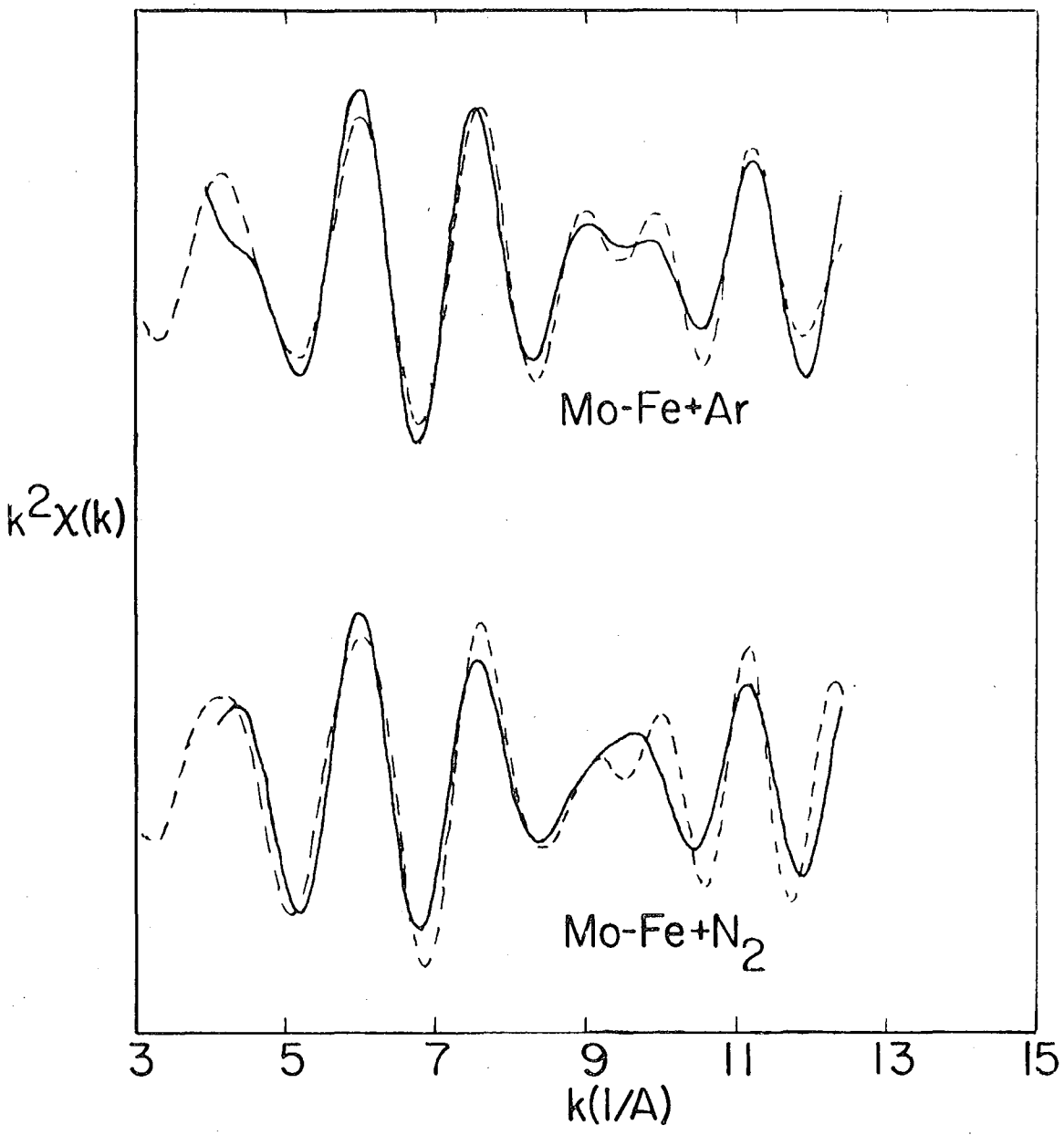

XBL 787-9911

Figure 22

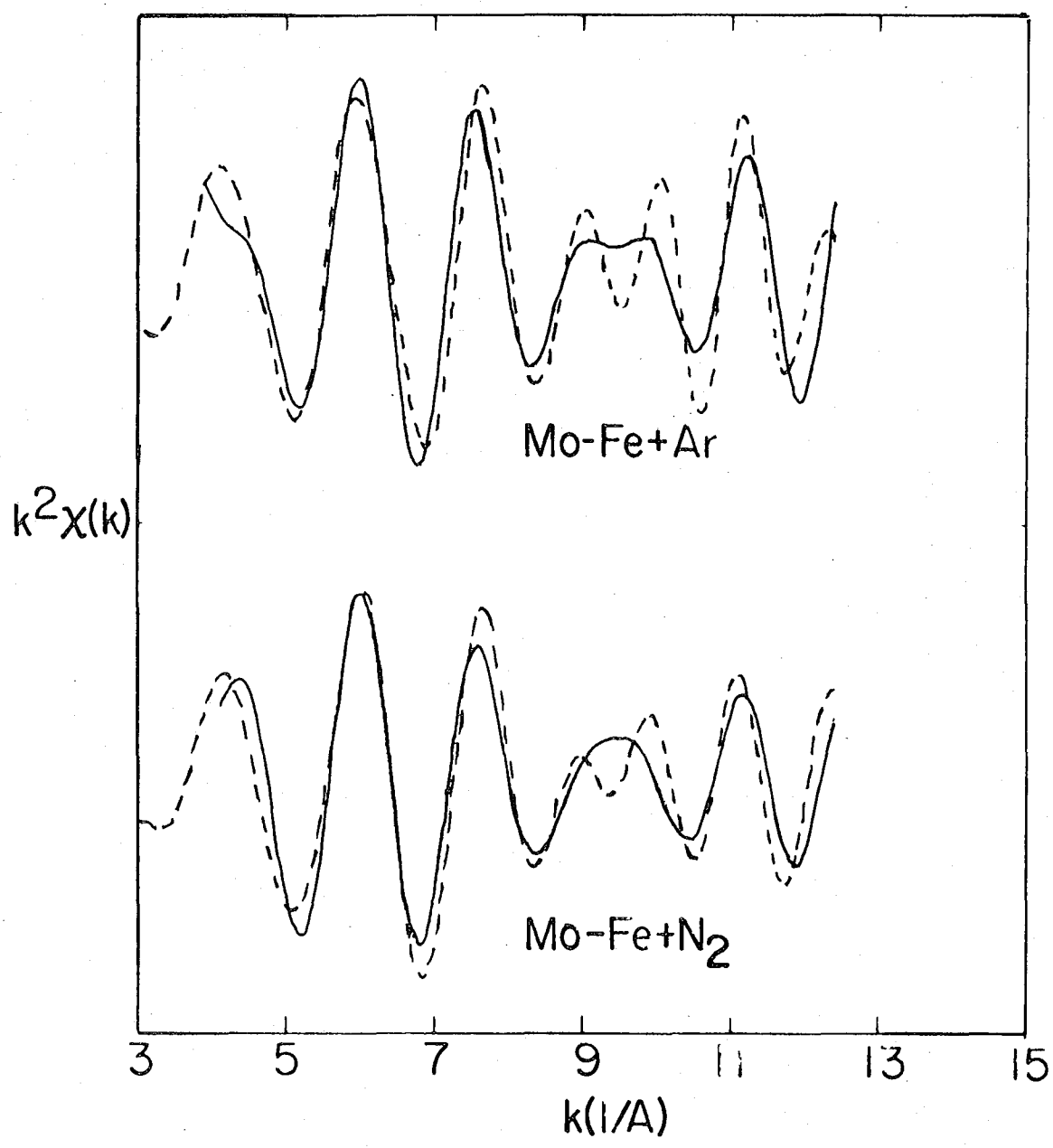

Figure 23

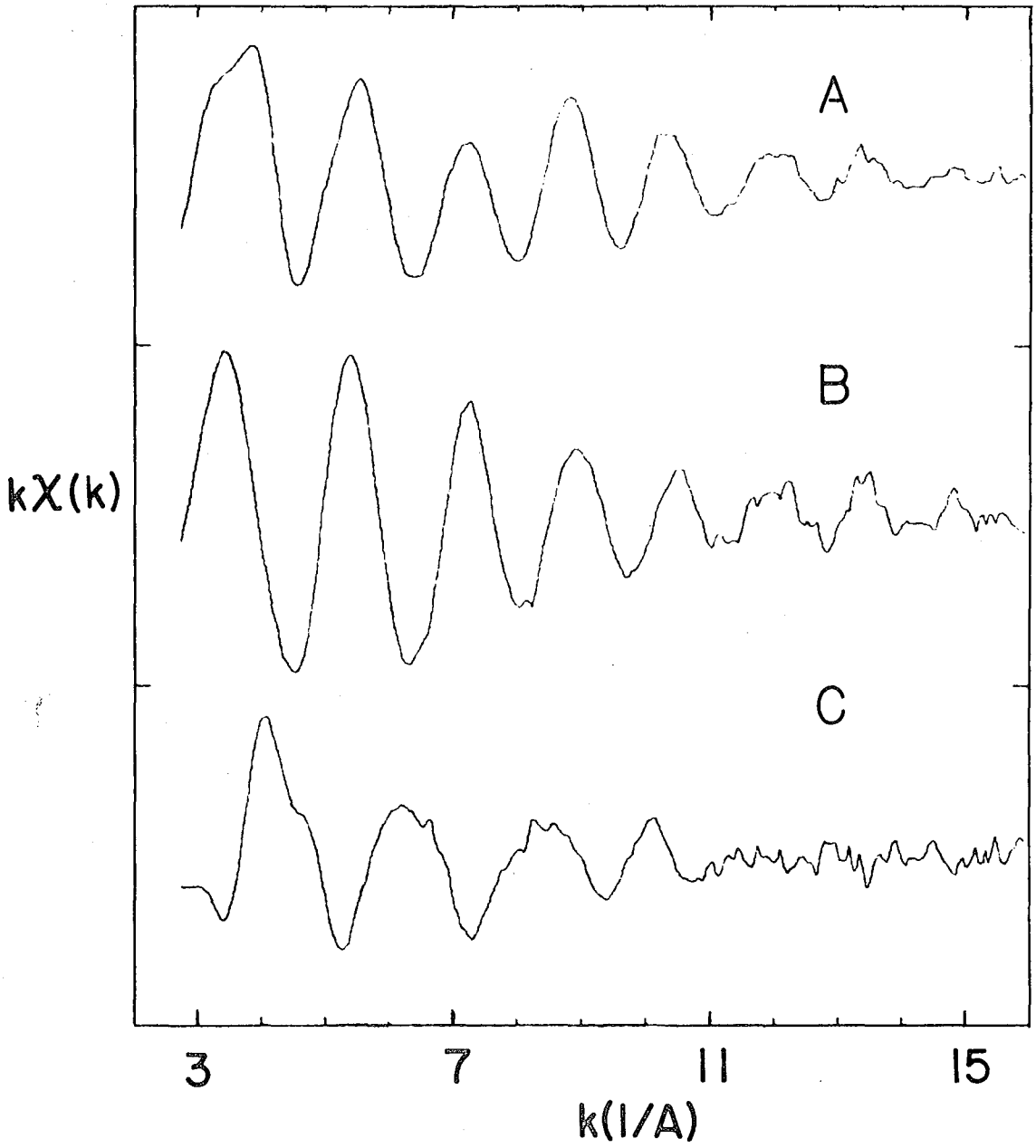

XBL 786-9124

Figure 24

Chapter IV

Experimental Considerations in X-Ray Absorption Spectroscopy

In this chapter, experimental considerations pertinent to the x-ray absorption spectroscopy of dilute molybdenum solutions will be discussed. The discussion will include a brief summary of the properties of the synchrotron radiation source, the fluorescence technique for the study of dilute species, experimental problems peculiar to the use of the synchrotron radiation source and techniques for the calibration of the x-ray monochromator.

A. The Synchrotron Radiation Source

The intense, broadband x-ray source that is occasionally available at the Stanford Synchrotron Radiation Laboratory has made it possible to perform useful measurements of the x-ray absorption spectra of metals in biochemical systems such as metalloproteins. The dependence of the x-ray beam intensity on the energy of the electrons in the storage ring has been discussed in detail by Lindau and Winick[1]. As an example, we have found that when the stored electrons have an energy of 3.4 GeV and are circulating with a beam current of 30 mA, the EXAFS II monochromator will provide a flux of 10^8 - 10^9 photons per second at x-ray energies between 19 and 21 KeV.

The fluorescence detection technique for EXAFS measurements was

employed in this work. In this method, the characteristic x-ray fluorescence of the element of interest , detected against a background of x-ray scattering, is used to monitor the photoabsorption coefficient. The high degree of polarization of the synchrotron radiation beam[1] is advantageous for fluorescence studies. When polarized x-rays are scattered, the intensity of the scattered x-rays is lowest along the axis of polarization of the exciting radiation.[3] X-ray fluorescence, on the other hand, is emitted isotropically. By observing the x-ray fluorescence along the axis of polarization of the exciting radiation, the ratio of x-ray fluorescence to x-ray scattering that strikes the detector in increased, resulting in an effective increase in the signal-to-noise ratio of fluorescence detection.

B. Time Dependence of the X-Ray Beam Intensity

The synchrotron radiation beam intensity is time dependent in both the fast and slow domains. The high frequency time structure [1] is of no concern in the present discussion. Under normal operating conditions, after injection of electrons into the storage ring, the x-ray beam is sufficiently stable for use in the measurement of absorption spectra. From this point onward, the beam intensity decays slowly with time, until data collection must be stopped for re-injection. Sudden, unexpected losses of beam intensity due to technical difficulties are not unusual. This type of time dependence makes it necessary to monitor beam intensity during the aquisition of data. For dilute samples, the improvement of the signal-to-noise ratio by signal averaging is best accomplished by averaging the results of several scans of 15-25 minute duration rather than by taking 1 scan with a very long counting time for each point. In this way, an unexpected loss of beam

intensity will only ruin one scan, rather than an entire data set. This is approach also minimizes background artifacts due to the non-linear response of the ionization chamber detection system to the time decay of the x-ray beam intensity.

C. Calibration of the X-Ray Monochromator

In the course of this study, it has been found that great care must be taken to insure that the x-ray monochromator is correctly and reproducibly calibrated. Careful calibration will insure that data sets obtained at different times will be comparable, and protects against monochromator instabilities that might arise during the collection of data. It is especially important to run calibration spectra at frequent intervals during the collection of a large set of scans that are to be averaged at a later date. In the event that drifts in the monochromator calibration occur during the collection of data, the energy scales of the various scans can be adjusted at a later date using the calibration spectra as energy standards.

The experience of this study indicates that changes in the energy calibration of the EXAFS II monochromator at the Stanford Synchrotron Radiation Laboratory come from two major sources. The first of these is mechanical malfunction of the monochromator mechanism. During the first 6 months of operation of the EXAFS II facility (July 1976 - December 1976), slippage in the monochromator drive mechanism caused very serious drifts in the monochromator calibration. This situation was allowed to persist until the monochromator drive mechanism broke down completely late in 1976. The offending parts were repaired and performance of the monochromator was greatly improved.

A second source of instability lies in the operation of the

storage ring. After each injection of electrons, the position of the stored beam near the EXAFS II port is adjusted or "steered" to produce maximum x-ray intensity at the EXAFS II experimental station. This causes changes in the x-ray source position form one injection to the next, resulting in small changes in the monochromator calibration. To offset this problem, it has become our practice to run a standard spectrum after each steering of the beam.

D. Standards for Calibration of the X-Ray Monochromator

A desirable specimen for calibration of the x-ray monochromator would be a chemically and physically stable material, of known composition and highly concentrated in the absorber of interest. In addition, the spectrum of the ideal standard specimen would have some feature whose position in the absorption spectrum could be unambiguously and precisely defined. The position of this feature could then be assigned a fixed energy.

It is common practice to use molybdenum metal foil as a standard specimen for studies of molybdenum containing compounds[4]. This practice was followed in the present work. In hindsight, however, molybdenum foil was found to have two major disadvantages from the point of view of its use as a standard material.

The first of these is the apparent variability in the absorption edge spectra of different pieces of molybdenum foil. In figure 1 the spectra of molybdenum foil samples obtained at different times at the Stanford facility are shown. To some extent, the differences in the spectra can be explained by variations in the monochromator resolution from run to run. However, there does seem to be some significant variation from sample to sample. Comparison of these spectra with

spectra obtained with conventional x-ray spectrometers[5] suggests that the differences between calculated predictions of edge structure[5] and experimental results may be partly due to the origin of the molybdenum sample used. In any event, the results shown in figure 1 suggest that a single piece of molybdenum foil be enshrined for use as a standard in all experiments and that caution be exercised when comparing the energy scales of spectra presented by different authors.

A second difficulty with the choice of molybdenum foil as a standard material lies in the use of the inflection point in the edge spectrum as a marker feature for the definition of the energy scale. The position of the inflection point is usually determined from the derivatives of the edge region spectrum.[4] The derivative of the spectrum at each energy is computed by fitting a polynomial to the data over some energy domain above and below the energy of interest, followed by evaluation of the analytical derivatives of the fitted function. The molybdenum foil edge has two distinct inflection points within a space of about 12 eV. As the domain of fitting for calculation of derivatives increases, or as the spectrometer resolution decreases, the apparent separation between the inflection points decreases. In figure 2, the second derivatives of an edge spectrum for several fitting domains are shown. The results in figure 2 indicate the dependence of the second derivative on the fitting domain. These derivatives should be useful for comparing the energy scale used in this work with that used in other published reports[4]. In this work, a standard domain of 10 eV above and below the energy of interest was used for the computation of derivatives. This rather broad domain allowed a common derivative method to be applied to both high and low resolution metal edge spectra as well as

to noisy single scan nitrogenase edge spectra.

E. Experimental Apparatus

The experimental apparatus used for absorption measurements has been described by Kincaid.[6] In the present work, argon filled ionization chambers were used for the measurement of incident and transmitted x-ray intensity. A 3 element silicon semiconductor detector was used for fluorescence measurements.[2] A block diagram of the apparatus is shown in figure 3.

F. Fluorescence Detection of X-Ray Absorption Spectra

The fluorescence detection technique is useful for the study of samples with low concentrations of the absorber of interest.[2] Both sodium iodide scintillation counters[8] and silicon semiconductor detectors have been successfully used for fluorescence studies. The x-ray radiation striking the fluorescence detector consists of the x-ray fluorescence of the element of interest and the background radiation composed of coherent (Thomson or Rayleigh) and incoherent(Compton) scattering as well as the x-ray fluorescence of the other elements in the sample. The signal-to-noise ratio of a fluorescence measurement is determined by the total count rate (photons/sec) accepted as data, the ratio of the count rate due to the x-ray fluorescence of interest to the total count rate and the counting time per data point.

The silicon solid state detector permits the partial resolution of the x-ray fluorescence of interest from the background radiation. Resolution is accomplished at the cost of having a lower maximum input count rate than that available with scintillators or with silicon detectors operated in a low resolution mode. For example, when the silicon detectors used in this work are operated in a high resolution

mode, the total input count rate is limited to 1.2×10^4 counts/sec in each of the 3 elements. This is to be contrasted with the 2×10^5 counts/sec rates that are obtainable with sodium iodide detectors.[8] The higher counting rates obtainable with sodium iodide detectors offset, to some extent, the low energy resolution of such detectors.

G. Niobium Fluorescence Filters

To maximize the signal-to-noise ratio of data collected in the fluorescence mode, the ratio of the count rate due to the fluorescence of the element of interest to the total count rate should be as high as possible. For studies of molybdenum K edge spectra, the fluorescence of interest occurs at 17.4 KeV, while the scattered x-rays have energies largely in excess of 19 KeV. The actual energy distribution of the scattered x-rays depends on the energy of the incident x-ray beam and the fluorescence detector geometry.

Because the niobium K edge is at 19 KeV, placing niobium filters between the sample and the fluorescence detector preferentially attenuates the intensity of the scattered x-rays. The radiation transmitted through the foils has an increased fraction of its total intensity due to molybdenum fluorescence. The use of this sort of filter, in a different context, has been described by Compton and Allison.[3]

When the storage ring at SSRL was operating at 3.4 GeV and 30 mA electron current, the radiation scattered from a 2 cm thick aqueous solution sample was usually intense enough to exceed the 1.2×10^4 counts/sec maximum rate of the silicon detectors. In practice, the detector was placed as close as possible to the sample, and by inserting successive layers of 0.001 in. thick niobium foil, the x-ray intensity was reduced such that the input count rate was less than 1.2×10^4

count/sec. A thickness between 0.004 in. and 0.008 in. of niobium foil was usually sufficient for this purpose. As the beam intensity decayed with time, layers of niobium foil would be removed to keep the detector operating at an input rate of 1.0×10^4 to 1.2×10^4 counts/sec.

The ratio of the change in fluorescence count rate at the absorption edge to the total count rate just above the absorption edge is an estimate of the fraction of the total count rate that is due to the fluorescence of the element of interest. For spectra with the same total count rate, an increase in this ratio provides an effective increase in the signal-to-noise ratio of the data. In 3 of the 4 data collections done during the course of this work the niobium foil filters were used. In table I, values of the ratio of the change in count rate at the edge to the total count rate above the edge are given for the 4 data collections. These results show that the use of the niobium filters did not produce a dramatic increase in the signal-to-noise ratio of the fluorescence data. In retrospect, the resolution of the silicon detector seems to be the most important factor in determining the signal-to-noise ratio of fluorescence data. It was noted, for example, that the resolution of the detector during the collection of the 10/76 data was considerably poorer than it was during the collection of the 5/77 data. This probably accounts for the lower signal-to-noise ratio of the 10/76 data.

H. Pulse Height Spectrum of the Radiation Striking the Fluorescence Detector

In figure 4, the pulse height spectrum of the output of a single element of the 3 element silicon semiconductor detector is shown. The sample being observed is a 2 cm thick solution of the Mo-Fe component of

nitrogenase with a molybdenum concentration of about 50 micrograms/ml. The sample is being excited with 20.2 KeV x-rays. The spectrum was obtained by feeding the output of the silicon detector pulse amplifier into a multichannel analyzer. The peaks in figure 4 are due to niobium fluorescence excited by scattered x-rays (channel 35), molybdenum x-ray fluorescence from the nitrogenase sample (channel 62), Compton (incoherent) scattering (channel 92) and Rayleigh (Thomson or incoherent) scattering (channel 131). The energy scale was defined by assigning an energy of 16.5 KeV (Nb K fluorescence) to channel 35 and 20.2 KeV (the energy of excitation) to channel 131. Intermediate energies were calculated by interpolation. When acquiring EXAFS data in the fluorescence mode, only pulses with heights roughly corresponding to channels 48 - 72 would be counted. A counting "window" was selected with a single channel analyzer whose output was fed into the EXAFS data acquisition computer.

When excited with 20.2 KeV x-rays, a point sample will Compton scatter (at 90^{o} to the incident beam) x-rays with an energy of 19.4 KeV.[3] In practice, the spectrum of x-rays Compton scattered from a sample of finite size and detected in a solid state detector will be asymmetrically distributed about the energy of maximum intensity, with a tail on the low energy side of the maximum.[7] In figure 4, only the low energy tail of the Compton scattering is visible because the niobium foil has greatly attenuated the intensity of x-rays with energies in excess of 19 KeV.

I. Comparison of Absorption and Fluorescence Data

Jaklevic et al.,[2] showed that, for thick samples with low concentrations of the absorber of interest, the fluorescence intensity is

proportional to the photoabsorption cross section of the element of interest. In figure 5, absorption and fluorescence mode spectra of a nitrogenase sample are compared. The pre-edge background absorbance of the absorption mode spectrum has been removed. The absorption edge and EXAFS are clearly visible in both types of data. The signal-to-noise ratios of fluorescence and absorption mode spectra are, in this case, comparable.

It will be noted that the absorption mode spectrum is marred by several discontinuties or "glitches". A particularly severe glitch occurs at about 20.25 KeV. Glitches are introduced by the x-ray monochromator crystal and their origin has been discussed by Kincaid[6]. Note that the glitch at 20.25 KeV is either absent or greatly reduced in magnitude in the fluorescence mode spectrum. This effect can be explained as follows. By examining the output of the incident intensity ionization chamber (I_0) as a function of x-ray energy, it was determined that the glitch at 20.25 KeV was a result of a sudden decrease in the x-ray intensity. The decrease represented a 0.3 % change in the total x-ray intensity. In principle, the two ionization chamber system is insensitive to changes in beam intensity. In practice, the two ionization chambers are not perfectly matched, and a sudden change in the intensity results in spurious change in absorbance, In figure 5, the absorbance due to the molybdenum in nitrogenase represents only 0.6 % of the total absorbance at 20.25 KeV. The magnitude of the glitch at 20.25 KeV is about 0.1 % of the total absorbance. It is only because the high photon flux of the synchrotron radiation source permits a very precise measurement of the absorbance that the glitch is detectable at all.

In the case of the fluorescence mode data, the measured quantity is F/I_0, the fluorescence intensity divided by the incident intensity. The three fluorescence detectors accept as data a total of 3×10^3 counts/sec. The I_0 ionization chamber absorbs roughly 10 % of the incident flux or 10^7 photons/sec. Assuming that the errors in the measurement of F and I_0 are dominated by photon counting statistics, the total error in F/I_0 will be clearly be dominated by the 2 % error in F. The error in F is roughly 7 times as large as would be the fluctuation in F due to a 0.3 % change in I_0. As a result, the glitch is buried in the statistical noise in F/I_0. In the data shown in figure 5, the fluorescence mode spectrum has the advantage that the interference due to glitches is greatly reduced in magnitude.

References

1. I. Lindau and H. Winick; Synchrotron Radiation: Sources and Research Applications, Stanford Synchrotron Radiation Laboratory Report No. 76/03 (1976).

2. J. Jaklevic, J.A. Kirby, M.P. Klein, A.S. Robertson, G.S. Brown and P. Eisenberger; Solid State Commun. (1977)23, 679 - 682.

3. A.H. Compton and S.K. Allison; X-Rays in Theory and Experiment, 2nd ed., D. Van Nostrand Co., N.Y.(1935).

4. S.P. Cramer, T. Eccles, F. Kutzler, K.O. Hodgson and L.E. Mortenson; J. Am. Chem. Soc.(1976)98, 1286 - 1287.

5. J.E. Muller, O. Jepson, O.K. Anderson and J.W. Wilkins; Phys. Rev. Lett.(1978)40, 720-722.

6. B.M. Kincaid; Ph. D. Thesis, Stanford University (1974).

7. R.D. Giaque, F.S. Goulding, J.M. Jaklevic and R.H. Pehl; Trace Element Analysis by X-Ray Fluorescence, Lawrence Berkeley Laboratory Report No. 647 (1972).

8. G.S. Brown, G. Navon and R.G. Shulman; Proc. Nat'l. Acad. Sci. - USA(1977)74, 1794 - 1797.

Table I

Fraction of Total Fluorescence Count Rates

Due to Molybdenum Fluorescence

Data Collection	Gas Phase	Channel	ΔF/F	F	Niobium Filters
3/76	Ar[1]	F1	0.25[2]	900[3]	Yes[4]
	N_2	F1	0.27	900	"
7/76	He	F1	0.14	1305	No
	"	F2	0.25	871	"
	"	F3	0.18	1081	"
	N_2	F1	0.14	1305	"
	"2	F2	0.26	789	"
	"	F3	0.18	1046	"
10/76	Ar	F1	0.13	760	Yes
	"	F2	0.13	757	"
	"	F3	0.15	678	"
	N_2	F1	0.15	682	"
	"2	F2	0.16	756	"
	"	F3	0.19	681	"
5/77	Ar	F1	0.26	565	"
	"	F2	0.19	671	"
	"	F3	0.32	568	"
	N_2	F1	0.27	593	"
	"2	F2	0.21	716	"
	"	F3	0.36	628	"

Notes for table I

1. The samples were solutions of the Mo-Fe component of nitrogenase equilibrated with the gases indicated.
2. ΔF/F is the ratio of the change in fluorescence count rate at the absorption edge to the total fluorescence count rate above the edge.
3. F is the total fluorescence count rate in counts/sec, accepted as data, measured just above the molybdenum absorption edge.
4. Niobium foil filters were used (yes) or not used (no) as described in the text.

Figure Captions

1. Edge spectra of molybdenum foil samples. (a) Data taken October 1976 on EXAFS II monochromator. (b) July 1976 - EXAFS II. (c) May 1977 - EXAFS II. (d) December 1976 - EXAFS II. (e) February 1976 - EXAFS I. The energy scale for each spectrum was defined by setting the energy of the edge inflection point to 20003.9 eV. The inflection points were found by fitting a third order polynomial to the data over a domain of 10 eV above and below the point of interest and then evaluating the second derivative of the fitted function.
2. Second derivatives of the absorption edge shown in trace (e) of figure 1. The derivatives were calculated as described in the text using the following fitting domains.(a) 1.75 eV; (b) 2.5 eV ; (c) 5.0 eV; (d) 7.5 eV and (e) 10 eV.
3. Block diagram of the apparatus used for EXAFS measurements.
4. Pulse height spectrum of the output of silicon semiconductor detector pulse amplifier. The sample is a solution of nitrogenase as described in the text. The spectrum shown was accumulated in a 2 minute counting period.
5. Comparison of absorption and fluorescence mode spectra of a nitrogenase sample. The spectra were collected simultaneously and represent 4.6 hours of actual counting time. The fluorescence spectrum is the average of the data collected by three detector elements. The background absorbance in the absorption mode spectrum was removed by fitting a polynomial to the pre-edge portion of the spectrum followed by extrapolation and subtraction of the fitted function from the entire data set.

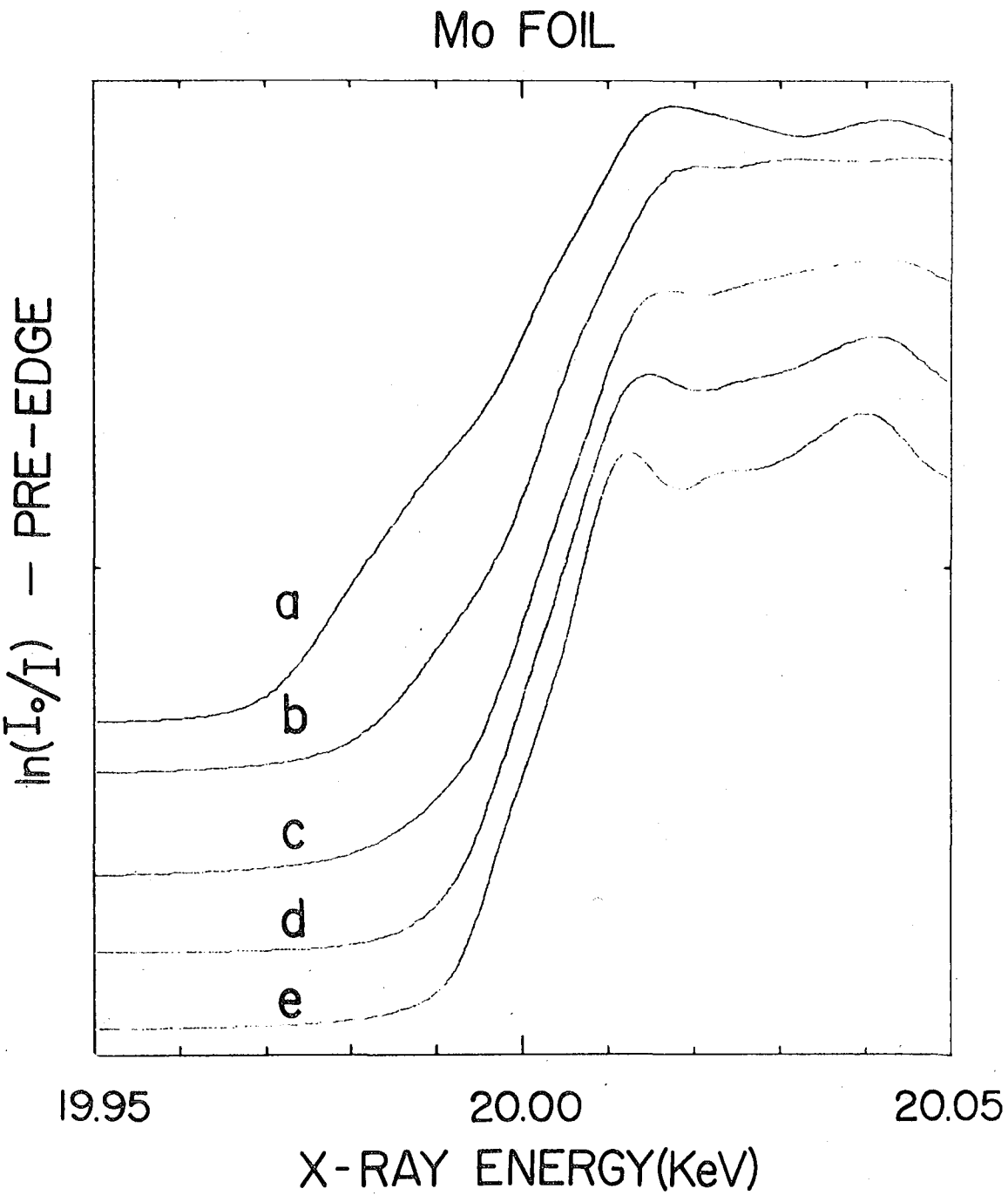
Mo FOIL
ln(I₀/I) - PRE-EDGE
a
b
c
d
e
19.95
20.00
20.05
X-RAY ENERGY(KeV)
XBL 786-3992

Figure 1

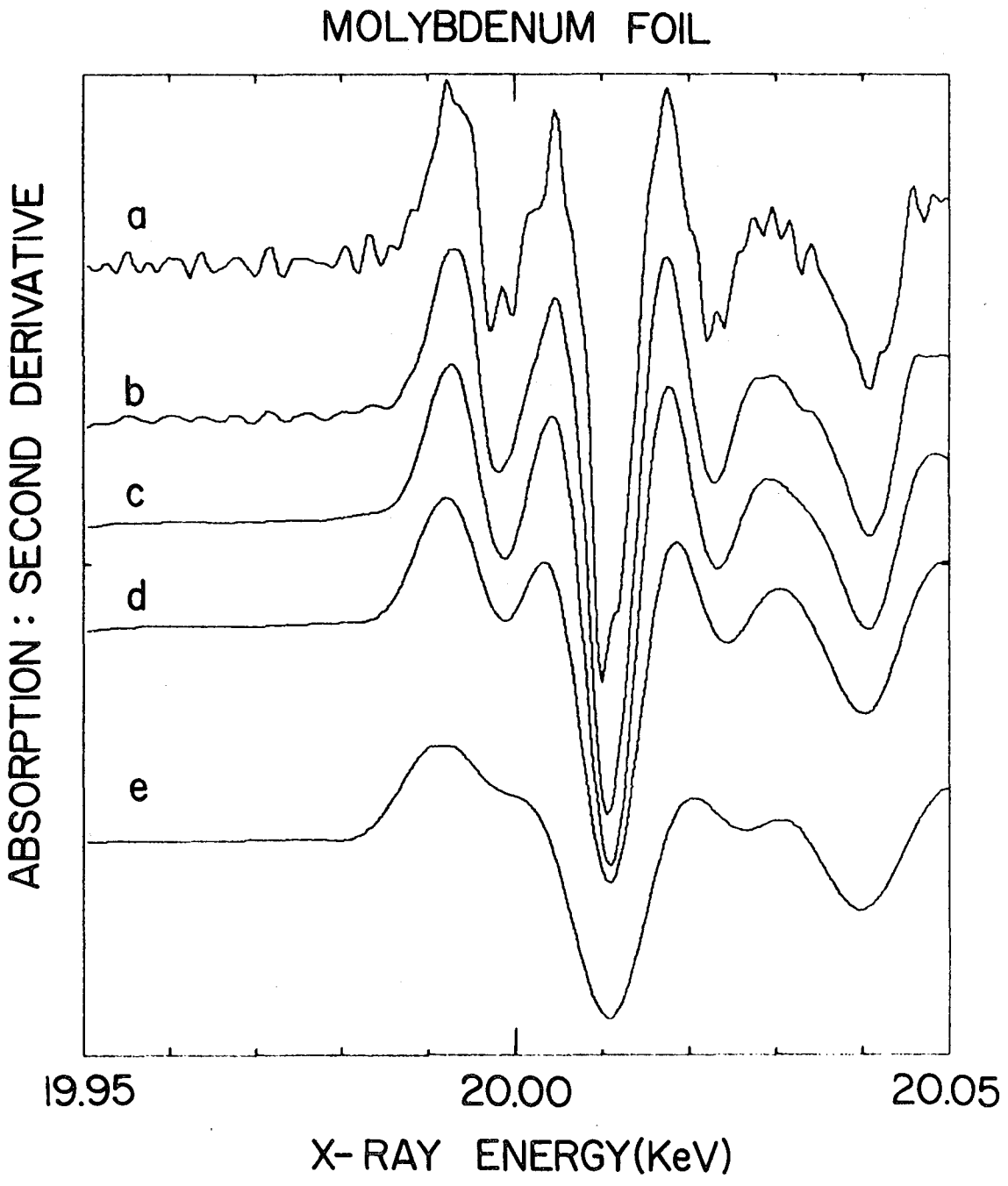

XBL 786-4039

figure 2

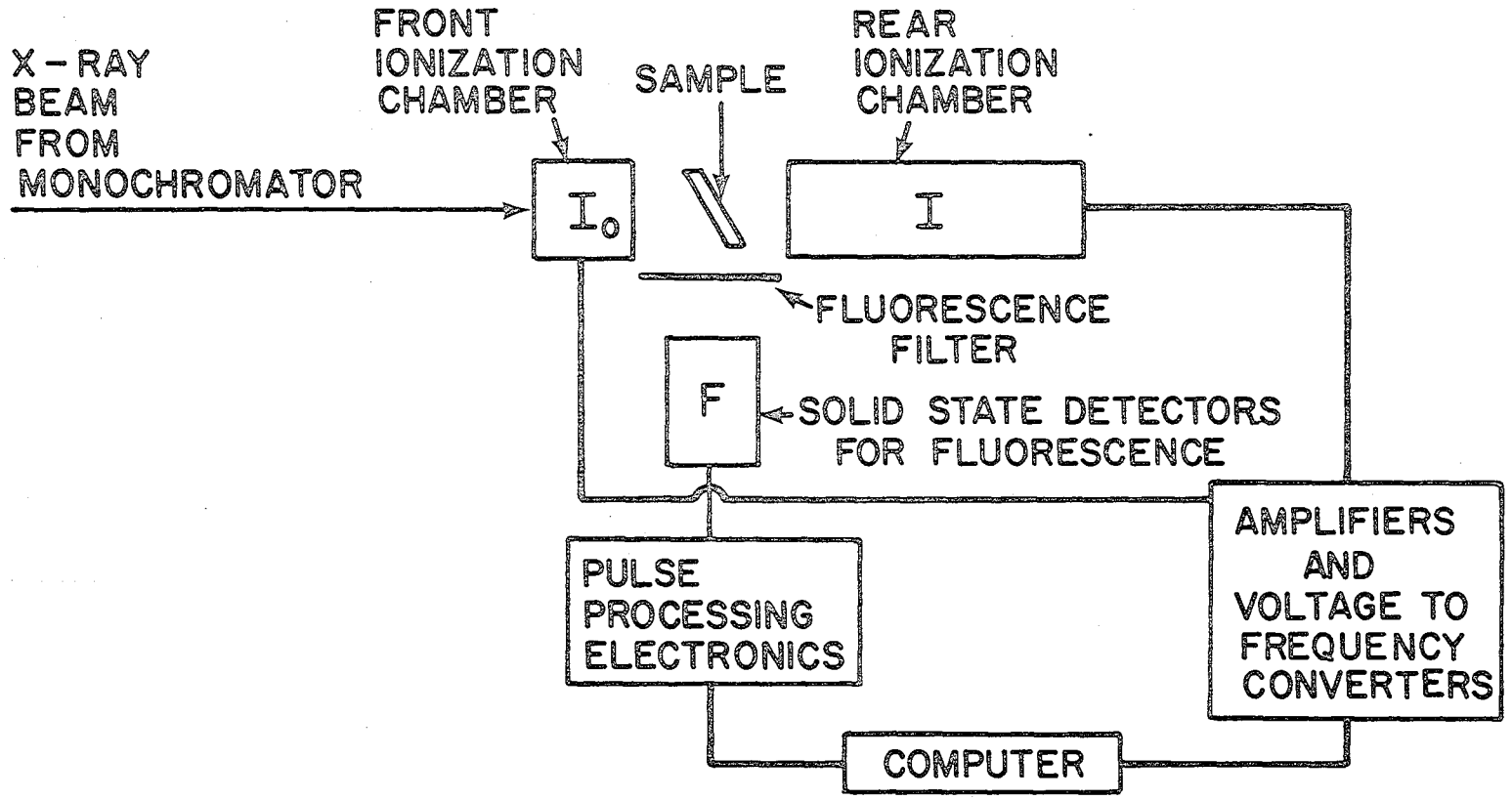

APPARATUS FOR EXAFS MEASUREMENT

XBL778-4525

Figure 3

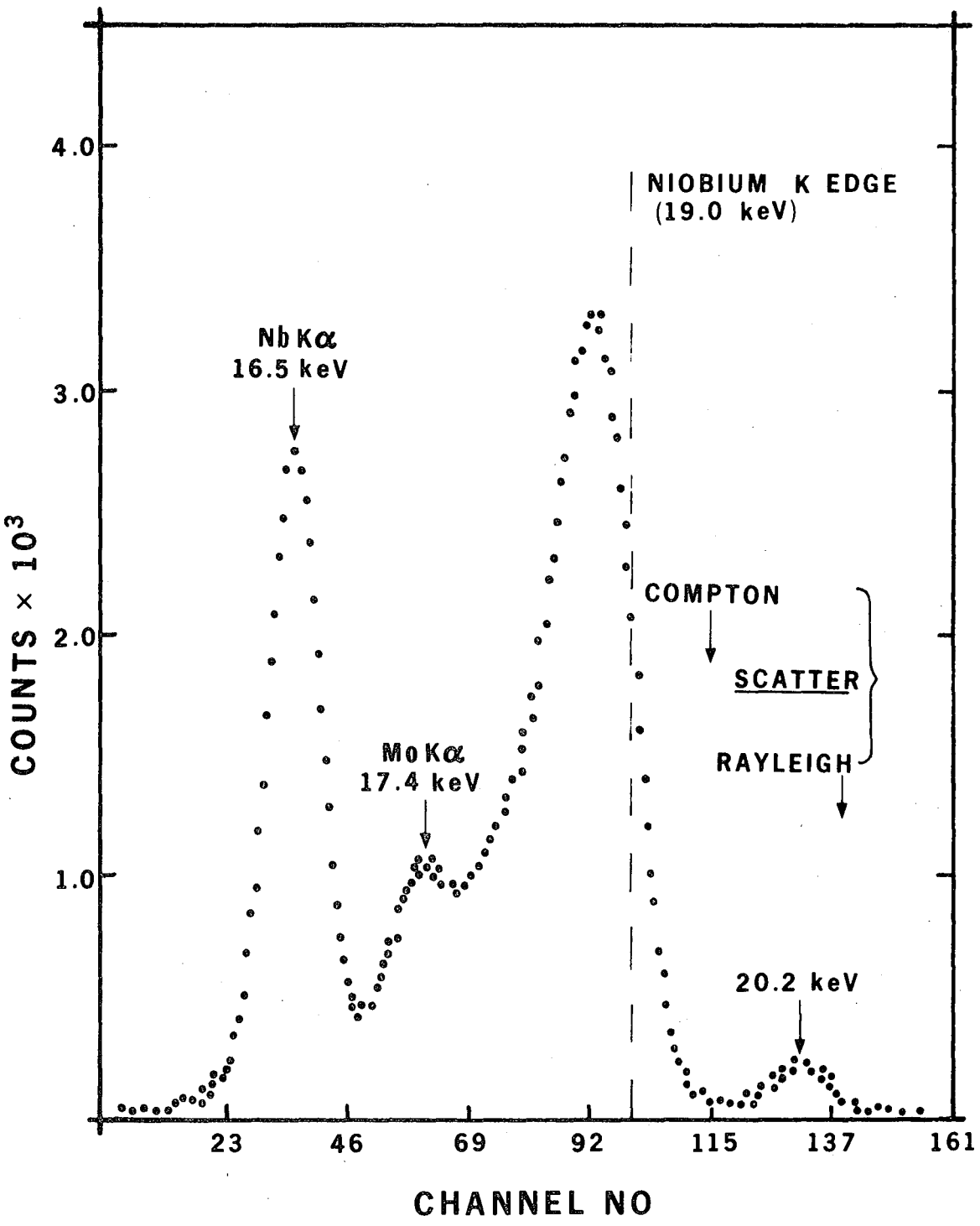

XBL 784-7969

Figure 4

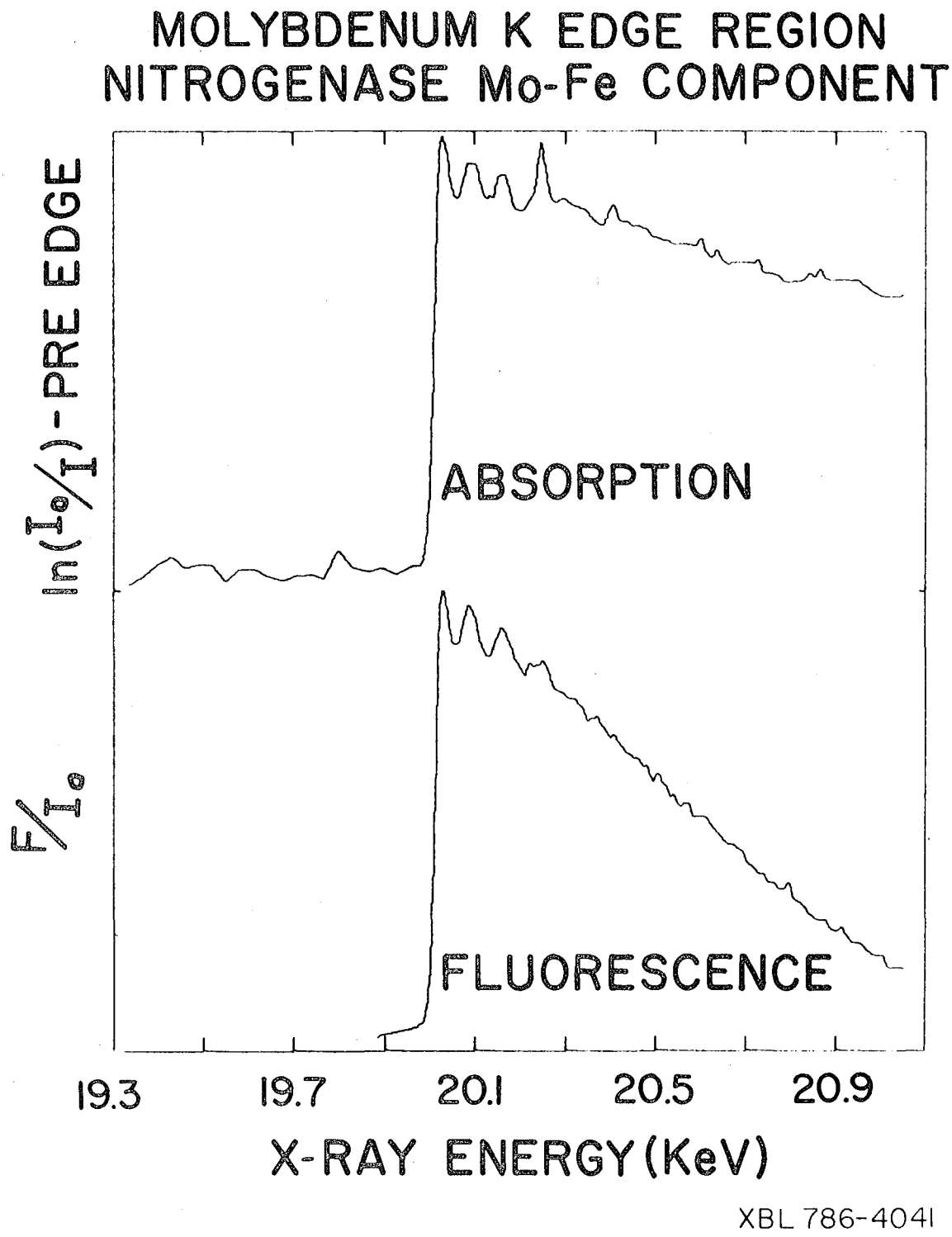
MOLYBDENUM K EDGE REGION
NITROGENASE Mo-Fe COMPONENT
ln(Io/I) - PRE EDGE
ABSORPTION
F/Io
FLUORESCENCE
19.3
19.7
20.1
20.5
20.9
X-RAY ENERGY (KeV)
XBL 786-4041

Figure 5

Chapter V

Factors Controlling The Precision of Measurements of X-Ray Absorption

The data collected in an experimental study of x-ray absorption spectra must be of sufficient precision to permit a meaningful interpretation of the results. The intense, broadband x-ray source available at the Stanford Synchrotron Radiation Laboratory (SSRL) has made it possible to make useful x-ray absorption measurements on samples with very low concentrations of the absorber of interest. Even with the high x-ray flux available at this facility, the signal-to-noise (S/N) ratio of spectra of metalloprotein samples frequently must be increased by spectrum averaging in order to obtain sufficiently precise data. This is particularly true for the measurement of the small changes in absorbance due to extended x-ray absorption fine structure (EXAFS). Because of the intense user demand for beam time at SSRL, there are definite limitations on the amount of time available for long term spectrum averaging.

In this chapter, the factors that determine the S/N ratio of an x-ray absorption spectrum will be considered. A simple formula for a "detectability factor" which is useful for assessing the relative difficulty of making measurements on samples of different compositions will be proposed. The discussion will center on the direct measurement

of x-ray absorption with the two ionization chamber system described by Kincaid[1]. The fluorescence detection technique[2], which is useful for studies of dilute absorbers, will be compared with the direct absorption method. Based on the assumption that the error in a measurement of the absorbance is dominated by photon counting statistics, an explicit formula describing the dependence of the error on the absorbance of the sample and of the two ionization chambers will be derived. In many cases, measurements at SSRL are made under less than optimum conditions of sample thickness and ionization chamber absorbance. The increase in the S/N ratio obtainable through optimization of the experimental conditions will be considered. Finally, the results of a limited experimental study of the dependence of the error in measurements of the absorbance on the sample thickness will be presented.

A. The Measurement of Absorbance

The linear absorption coefficient μ is defined by Lambert's law[3].

$$I_0/I = e^{-\mu x} \tag{1}$$

In equation 1, I_0 and I are the intensities of the incident and transmitted radiation, respectively, and x is the sample thickness. Experimentally, μx is determined with a two ionization chamber system(fig 1). I_0 is estimated by absorbing part of the incident radiation in the front ionization chamber. I is measured by the rear ionization chamber which, under ideal conditions, absorbs all of the transmitted radiation.

An alternative scheme for the measurement of μ is to monitor the fluorescence intensity F.[2]

$$F = \omega I_0 \frac{\mu_{PE}}{\mu} \left(1 - e^{-\mu x}\right) \tag{2}$$

where ω is the fluorescence yield, μ_{pe} is the absorption coefficient for K shell photoabsorption and μ is the total x-ray absorption coefficient. In equation 2, we have neglected effects due to the self-absorption of the emitted fluorescence by the sample matrix.

B. EXAFS Measurements on Dilute Systems

EXAFS is a modulation of μ in the energy region immediately above an absorption edge. The amplitude of EXAFS modulation is typically no larger than 10 % of the size of the sharp change in μ that occurs at the absorption edge. The relative amplitude of the modulation in μ is largely determined by the mole fraction of the absorber of interest in the sample. As the mole fraction of the absorber of interest decreases, we must make increasingly precise measurements of μ in order to obtain useful EXAFS data.

There is a great deal of interest in using synchrotron radiation sources for EXAFS studies of biochemical systems. The absorber of interest in such studies is usually a metallic element such as calcium, strontium, molybdenum or one of the first row transition metals. The metal content of biological materials is often only a small fraction of the dry weight of the sample.The detection of EXAFS therefore requires the measurement of very small changes in μ because the absorber of interest contributes only a small fraction of the total x-ray absorbance.

Although several interesting studies of metalloproteins have been carried out using lyophilized materials[4,5], a great deal of interesting biochemistry takes place only in aqueous solution. Due to the limited solubility of metalloproteins in water, the use of aqueous solution samples places an additional upper limit on the mole fraction of the

absorber of interest. In many solution samples, the overwhelming majority of the x-ray absorbance is due to the solvent.

The difficulties associated with the study of aqueous solution samples are illustrated by the example of the molybdenum in nitrogenase. A 100 mg/ml solution of nitrogenase in water conatins about 60 micrograms of molybdenum per ml. At this concentration, μ changes by 0.6 % at the molybdenum K edge. The modulations in μ due to EXAFS are smaller still. This example demonstrates that the study of EXAFS in aqueous metalloprotein systems requires a very precise determination of μ .

To some extent, the precision of x-ray absorption measurements may be increased by spectrum averaging. However, the beam time available for data collection at SSRL is strictly limited. When assessing the feasibility of a proposed x-ray absorption study, it is therefore important to consider how much time will be required for adequate data collection.

In order to make a meaningful estimate of the difficulty of a proposed experiment, estimates of the size of the modulations in μ due to EXAFS and the size of the errors in the measurement of μ are needed. These quantities can be used to estimate a S/N ratio for the measurement of μ . If an experiment must be conducted under conditions that give a low S/N ratio, longer data collection times will be required.

It is also useful to consider what an experimenter may do to optimize the S/N ratio of data collected on existing x-ray absorption equipment at SSRL and how much is to be gained through such efforts. There are four experimental conditions which are to some extent under the control of the experimenter. The sample thickness and the absorbance of the front and back ionization chambers are largely under the

direct control of the experimenter. To a smaller extent, the experimenter may increase the total available x-ray flux by requesting beam time when the storage ring is operating at a high energy and current. In studies of biological samples, solubility limits generally put a ceiling on the concentration of the absorber of interest. Beyond stating that the concentration of the absorber of interest should be as high as possible, we will not consider absorber concentration as a variable that is subject to optimization.

C. The S/N Ratio of an X-Ray Absorption Measurement

In obtaining EXAFS data, the absorbance μx, or some other function of μ, such as the fluorescence intensity, is measured as a function of x-ray energy. The question of defining the S/N ratio of an EXAFS measurement can be reduced to the consideration of two independent quantities. As outlined above, these are the size of the modulations in μx due to EXAFS and the size of the errors in the experimental determination of μx. The precision of a measurement of μx may depend on the magnitude of μx, but it does not depend on the fraction of μx due to the absorber of interest. The calculation of the error in a measurement of μx may therefore be formulated in a manner applicable to a sample of arbitrary composition. The precision of a measurement of μx necessary for the adequate detection of EXAFS obviously depends on the composition of the sample. The example of the absorbance due to molybdenum in a solution sample of nitrogenase is a case in point. The size of the modulations in μx due to EXAFS can be considered on a sample to sample basis. Both the error in the measurement of μx and the size of the modulation in μx due to EXAFS are conveniently expressed on a relative scale, i.e. as a fraction of the value of μx.

D. An Estimator of EXAFS Detectability

The ab initio calculation of EXAFS modulation amplitudes [1] could be used to estimate the size of the modulations in μx due to EXAFS. However, the difficulty of this approach precludes its general application. A more practical scheme may be to recognize the fact the EXAFS is a modulation of the cross section for photoabsorption in the energy range above an absorption edge. The amplitude of EXAFS modulation is therefore some fraction of the size of the edge jump, which we define as the contribution of the K shell photoabsorption cross section of the element of interest to the total absorption coefficient above the absorption edge.

The exact amplitude of EXAFS modulation depends on the sample temperature, the structure around the absorbing atom and the x-ray energy. However, the size of the modulation in μx due to EXAFS could be estimated as being roughly 5 - 10 % of the size of the edge jump.

The ratio of the edge jump to the total absorption coefficient above the absorption edge may be written as

$$D = \frac{\mu_A - \mu_B}{\mu_A} = \frac{\mu_{PE}}{\mu_A} \qquad (3)$$

where μ_A is the total absorption coefficient above the absorption edge and μ_B is the absorption coefficient without the contribution of μ_{PE}, the K shell photoabsorption coefficient of the element of interest. D is related to "edge jump ratio" S, which is commonly used in the literature of x-ray analysis[6], by equation 4.

$$D = 1 - 1/S \qquad (4)$$

Using tabulated data[7], μ_A and μ_B may be easily calculated for a sample of arbitrary composition. D represents the fraction of the total absorption coefficient that is due to photoabsorption by the element of interest. The relative size of the modulation in μx due to EXAFS will be no larger than 0.1D. For instance, if a sample had a D value of 0.5, the modulation of μx due to EXAFS would represent about a 5 % change in the value of μx.

In table I, the D values for several neat metallic elements and for dilute aqueous solutions of the same elements are given. The results show that while the D values for the neat elements are all similar, dilution of the metals in water causes a large decrease in D with the decrease being most marked for the elements of lower atomic number. This trend is a result of the absorption coefficient of water, which increases rapidly with decreasing x-ray energy. The results in table I illustrate some of the advantages of using D as an estimator of EXAFS detectability. The value of D for a given sample increases with the concentration of the absorber of interest, reaching a maximum when the mole fraction of the absorber of interest reaches 1.0. The smaller values of D for the aqueous solutions reflect the problems associated with detecting EXAFS in dilute systems by the absorption technique, especially for elements of lower atomic number.

Fluorescence detection of EXAFS is useful for studies of dilute systems. This technique measures the photoabsorption cross section of the element of interest by monitoring the x-ray fluorescence excited by the synchrotron radiation beam. A solid state detector is placed at approximately a 90° angle to the incident x-ray beam(fig. 1). The radiation striking this detector consists of x-ray fluorescence

as well as x-rays scattered from the sample. Both silicon semiconductor[2] detectors and sodium iodide scintillation detectors[4] have been successfully used for fluorescence detection of EXAFS. Silicon detectors allow partial energy resolution of scattered and fluorescent x-ray radiation at the expense of a lower maximum count rate than that available with sodium iodide detectors.

For both types of fluorescence detectors, the experimental task can be reduced to the detection of a small amount of fluorescence against a background of x-ray scattering. Because EXAFS is a modulation of the photoabsorption cross section of the element of interest, the modulation due to EXAFS in the intensity of the radiation striking the fluorescence detector is some fraction of the increase in intensity that occurs at the absorption edge.

The ratio of the fluorescence edge jump to the total intensity above the edge is given by

$$D_F = \frac{\omega \mu_{pE}}{\omega \mu_{pE} + \mu_{SC}} \qquad (5)$$

where ω and μ_{pE} are as in equation 2 and μ_{SC} is the total scattering coefficient of the sample. As in the case of the absorption D factor (eqn. 3), the relative changes due to EXAFS in the intensity of the radiation striking the detector will be no larger than 10 % of D_F. Two experimental factors not considered in equation 5 have the effect of increasing D_F. First, the synchrotron radiation beam is strongly polarized in the plane of the electron beam orbit in the storage ring. The fluorescence is observed roughly along the axis of polarization of the incident radiation. The fluorescence is emitted isotropically but

the intensity of the scattered radiation is lowest along the axis of polarization of the exiciting radiation.[3] This has the effect of increasing the ratio of detected fluorescence to detected scattering. A further increase in the effective D_F may be realized through the partial energy resolution of fluorescent and scattered radiation. D_F should therefore be considered a conservative estimator of fluorescence detectability. Using a silicon semiconductor detector, we found that for observations of molybdenum x-ray fluorescence, the experimental ratio of the fluorescence edge jump to the total intensity above the edge was 10 to 30 times larger than the D_F calculated on the basis of the sample composition.

D_F values for samples of different composition can be compared and reflect the relative difficulty of EXAFS detection using the fluorescence technique. Listed in table II are D_F values for several neat metallic elements and for dilute aqueous solutions of the same elements. The neat metal D_F values are all roughly equal. Dilution of the metals in water causes a large decrease in D_F. As the atomic number of the absorber of interest decreases for 42(Mo) to 20(Ca) D_F decreases slowly. This decrease is a result of the slow increase in the scattering coefficient of water as the x-ray energy decreases.

It is important to note that while the D value for the aqueous solutions decreases by a factor of 17 as the absorber is changed from molybdenum to calcium, the D_F values decrease by only a factor of 2. This is due to the fact that the absorption cross section of water increases much more rapidly with decreasing x-ray energy than the scattering cross section (fig. 2). As a result, the sensitivity of the fluorescence technique for EXAFS studies of aqueous solution samples

is not strongly dependent on the absorption edge energy of the absorber of interest. Conversely, absorption studies of solution samples are much more difficult at lower edge energies.

It should be stressed that values of D and D_F for the same sample are not directly comparable in terms of the S/N ratio of the spectra obtained by the absorption and fluorescence techniques. In order to make a meaningful comparison of the performance of the two methods, an estimate of the precision of measurements made by each technique is needed.

E. Calculation of the Error in Absorption Measurements

We will now present a method for the calculation of the error in a measurement of μx by the absorption technique. Our approach will be similar to that of Kincaid[1], who assumed that the errors in the measurement of I_0 and I were dominated by the statistical fluctuations in the numbers of photons detected in the front and rear ionization chambers. Kincaid[1] calculated optimum values for μx and for the absorbance of the front ionization chamber for the ideal case of 100 % absorbance by the rear ionization chamber. Beyond the statement that the S/N ratio as a function of μx and front chamber absorbance was flat near its maximum, no quantitative dependence of the S/N ratio on the experimental variables was presented.

In the present work, a formula for the error in a measurement of μx is derived. The dependence of the error on the absorbance of the sample and the front and rear ionization chambers is shown explicitly. The primary measured quantities in the experiment are the currents in the front and rear ionization chambers. The statistical errors in the primary measured quantities will be propagated through a calculation of

μx. The error in μx will be expressed on a relative scale, i.e., as a fraction of the value of μx. The relative error E is defined by

$$E = \frac{\Delta(\mu x)}{\mu x} \tag{6}$$

where $\Delta(\mu x)$ is the error in a measurement of μx.

We assume that the statistics of the ionization chamber currents are dominated by the random fluctuations in the photon count rate[1]. Accordingly, the average number of photons counted during a measurement in the front and rear ionization chambers, M_F and M_R respectively, have standard deviations given by

$$\Delta M_R = (M_R)^{\frac{1}{2}} \tag{7a}$$

$$\Delta M_F = (M_F)^{\frac{1}{2}} . \tag{7b}$$

We define the absorbance of the front and rear ionization chambers, F and R respectively, such that

$$F = \mu_F x_F \qquad \text{and} \qquad R = \mu_R x_R \tag{8}$$

where μ is the absorption coefficient and x is the thickness of the appropriate ionization chamber. M_F and M_R can be expressed as functions of F, R, μx and N, the total number of photons hitting the front ionization chamber during the measurement.

$$M_F = N(1-e^{-F}) \tag{9a}$$

$$M_R = Ne^{-F}e^{-\mu x}(1-e^{-R}) \tag{9b}$$

To calculate μx we need to know the flux incident on, and transmitted by the sample. These are called I_o and I, respectively.

$$I_o = M_F e^{-F}(1-e^{-F})^{-1} = Ne^{-F} \tag{10a}$$

$$I = M_R(1-e^{-R})^{-1} = Ne^{-F}e^{-\mu x} \tag{10b}$$

The standard deviations of I_o and I are given by equations 11a and 11b.

$$\Delta I_o = e^{-F}(1-e^{-F})^{-1}\Delta M_F \tag{11a}$$

$$\Delta I = (1-e^{-R})^{-1}\Delta M_R \tag{11b}$$

To calculate the error in μx, the errors in M_R and M_F are propagated by a power series technique.[8]

$$\mu x = \ln\left(I_o / I\right) \tag{12a}$$

$$\Delta(\mu x) = \left[\left(\frac{\partial \ln[I_o/I]}{\partial I_o}\right)^2(\Delta I_o)^2 + \left(\frac{\partial \ln[I_o/I]}{\partial I}\right)^2(\Delta I)^2\right]^{1/2} \tag{12b}$$

$$\Delta(\mu x) = \left[\frac{1}{N(1-e^{-F})} + \frac{e^F e^{\mu x}}{N(1-e^{-R})}\right]^{1/2} \tag{12c}$$

The relative error in μx is given by

$$E = \frac{\Delta(\mu x)}{\mu x} = \frac{1}{\mu x \sqrt{N}} \left[\frac{1}{(1-e^{-F})} + \frac{e^{F} e^{\mu x}}{(1-e^{-R})} \right]^{1/2} \quad (13)$$

Equation 13 shows that E decreases as $(N)^{-\frac{1}{2}}$, a result expected from the original assumption of Poisson photon counting statistics. If any one of the variables F, R or μx is zero, then the relative error becomes very large. As F or μx becomes very large, the relative error becomes very large. As R increases, E decreases to a constant value. These results are consistent with the intuitive feeling that a reasonable measurement of μx cannot be made if no radiation is absorbed in the sample or in either of the two ionization chambers.

A comparison of D and E for a given set of experimental conditions provides an estimate of the difficulty of detecting EXAFS for a particular sample. For instance, if D = 0.005 and E = 0.001, the edge jump will be approximately 5 times as large as the noise level. The EXAFS will be less than or equal to the noise level. Assuming that the E = 0.001 value was calculated for a 1 second measurement, at least 100 seconds of data per measurement would be needed to obtain EXAFS modulations 5 times the size of the noise level. On the other hand, for a metal foil sample with D = 0.8, a one second measurement would probably provide reasonably good data with EXAFS modulations 80 times bigger than the noise.

F. Optimization of Experimental Conditions

In the example described above, the sample with D = 0.005 yielded data with a S/N ratio of less than 1 for the detection of EXAFS. Assuming that this value is unacceptable, what can be done to improve it?

The brute force approach would be to increase N, as indicated in the example above. An increase in N can be accomplished by performing the experiment at a higher storage ring energy or by taking data for a longer period of time or by a combination of these techniques. In view of the scarcity of high energy beam time and the competition among users for the available beam time, the approach of increasing N has definite limitations.

Another strategy is to decrease E by optimizing the values of μx, F and R. Kincaid[1] has calculated optimum values for μx and F of 2.58 and 0.245, respectively, for the case of complete absorption of the transmitted radiation in the rear ionziation chamber. By a combination of changing the lengths of the ionization chambers, the chamber gas compositions and the sample thickness it is possible for the experimenter to operate at optimum values of F, R and μx. In many cases, however, experimenters at SSRL do not bother to construct ion chambers of special lengths for their experiments. The need to operate the standard SSRL ion chambers as continuously flushed chambers often makes the custom mixing of ionization chamber gases very expensive. It would be useful, therefore, to have a quantitative estimate of what happens to the S/N ratio as we depart form the optimum experimental conditions.

In figure 3, the dependence of E on μx for $N = 10^8$ is shown. The shapes of the curves are not dependent on N, but their ordinate values are scaled by $(N)^{-\frac{1}{2}}$. A family of curves is presented for a front chamber absorbance of F = 0.11 (90 % transmittance(T)) with R values as indicated. The minimum value of E decreases 700 % as R changes from 0.01 (99 %T) to 2.31 (10 %T). It should be noted that the minima in the error curves become broader as R gets larger, making the S/N ratio less

sensitive to the sample thickness. In table III, the minimum values of E versus μx for several values of R with F = 0.11 are listed.

In figure 4, R has been set at 2.3 (10 %T) and E versus μx has plooted for several values of F. Examination of this figure and the data in table IV shows that the relative error in μx is not as sensitive to the choice of F as it is to the choice of R.

In table V, the results of an optimization of μx and F for several fixed values of R are presented. Comparison of these results with those presented in table III shows that not much is to be gained by the optimization of F once R has been chosen. It should be noted that within the resolution of the present calculation (1 %T) the optimum values of F and μx approach those given by Kincaid[1] as R becomes large.

The results presented in the preceeding paragraphs serve as a guide to how much is to be gained by striving for optimum experimental conditions. As an example, suppose that for a high D sample such as a metal foil or a neat, low molecular weight compound, that data of acceptable S/N ratio can be obtained in 30 minutes under ideal experimental conditions (R = 2.3, F = 0.25 and μx = 2.5). Consider the effect of changing R to 0.36 (70 %T). The present calculations indicate that the S/N ratio should decrease to 62 % of its original value. In practice, to obtain data of the same quality as that collected in 30 minutes of ideal condition operation, the data collection time would have to be increased to 75 minutes. For high D samples, an increase in data collection time of this magnitude could probably be tolerated and the merits of spending a lot of money or effort to get R back up to 2.3 would be questionable. Now consider the effect of a similar change in R on a measurement of the absorption spectrum of a low D metalloprotein

sample requiring 4 hours of beam time per spectrum. It should be clear that in this case, significant amounts of time could be saved by the optimization of experimental conditions. An experimenter contemplating any extended study of low D samples would do well to expend some effort to see that the experimental conditions are optimized. This is especially true for studies requiring large amounts of scarce high energy beam time.

G. Experimental Dependence of E on μx

In order to test the hypothesis that E is dominated by photon counting statistics, the absorbance μx, and the standard deviation in μx of a 0.2 M $FeCl_3$ solution were measured for 20 different values of μx ranging from 0.8 to 6.5. Using a variable thickness solution cell, the absorbance was measured above and below the iron K edge at 7.112 KeV for 10 sample thicknesses. The SSRL EXAFS II monochromator, ion chambers and amplifier system were used. Nitrogen was used as the ion chamber gas in both the front and rear chambers, giving F and R values of 0.14 and 0.43 respectively. No extraordinary precautions were taken to reduce electronic noise in the system and the apparatus was in the condition in which the typical SSRL user would probably find it.

The outputs of I_0 and I voltage to frequency converters were counted 6 times for 7 seconds per count at each value of μx. Offset readings were taken with the beam shutters closed and were subtracted from the shutters-open count rates to give a net count rate. The net count rates were converted to voltages assuming that 10.0 V = 1 X 10^6 counts/second. Ionization chamber currents were calculated by multiplying the voltages by 10^{-G} where G is the gain setting of the Kiethly electrometer amplifier. The number of electrons collected was cal-

culated and converted to the number of photons absorbed by dividing by 209, which is the number of electrons produced per absorption of a 7.112 KeV photon in nitrogen gas.[10] The numbers of photons absorbed in the front and rear ionization chambers were converted to flux incident on and flux transmitted by the sample as per equations 10a and 10b.

The absorbance, μx, was calculated for each measurement of the incident and transmitted intensity as per equation 12a. The mean value of μx and the standard deviation of the mean value were calculated for each set of 7 measurements at a given energy and sample thickness. In figure 5 the experimentally determined values of E are plotted as a function of μx. In the same figure, the predicted dependence of E on μx is shown for R = 0.43, F = 0.14 and N = 2.7×10^8, which was the average total flux per 7 second counting period during the experiment. The experimentally determined relative error had values as high as 15 times the predicted error with a median value of 2.2 times the predicted error. This limited set of data shows that the standard deviation of an experimentally determined value of μx can be expected to be of the same order of magnitude as the error predicted on the basis of photon counting statistics. However, these results are insufficient both in scope and precision to serve as experimental confirmation of equation 13.

H. Summary

In this chapter, some of the factors which control the S/N ratio of experimental measurements of x-ray absorption have been considered. The calculation of the detectability factors D and D_F was discussed. D and D_F values are useful when assessing the difficulty of a proposed EXAFS study. When measuring EXAFS in a series of samples of different absorber concentrations, D and D_F values can be used as a guide for the

efficient allocation of data collection time among the various samples. The effects of sample and ionization chamber absorbance on the errors in absorption measurements were discussed. The presence of broad minima in the relative error functions showed that for high D samples, wide variation in the experimental conditions can be tolerated. For dilute samples, significant time savings can be effected by optimization of experimental conditions. In an experimental study, the errors in measurements of the absorbance were found to be of the same order of magnitude as the errors expected on the basis of photon counting statistics.

References

1. B.M. Kincaid; Ph. D. Thesis, Stanford University (1974).

2. J. Jaklevic, J.A. Kirby, M.P. Klein, A.S. Robertson, G.S. Brown and P. Eisenberger; Solid State Commun.(1977)23, 679 - 682.

3. A.H. Compton and S.K. Allison; X-Rays in Theory and Experiment, 2nd Ed., D. Van Nostrand & Co. Inc.,N.Y. (1935), p. 9.

4. G.S. Brown, G. Navon and R.G. Shulman; Proc. Nat'l. Acad. Sci.-USA (1977)74, 1794 - 1797.

5. S.P. Cramer, T.K. Eccles, F.W. Kutzler, K.O. Hodgson and L.E. Mortenson; J. Am. Chem. Soc.(1976)98, 1287 - 1288.

6. R.O. Muller; Spectrochemical Analysis by X-Ray Fluorescence, Plenum Press, N.Y.(1972), p. 15.

7. W.H. McMaster, N. Kerr Del Grande, J.H. Mullet and J.H. Hubbell; Compilation of X-Ray Cross Sections, UCRL-50174, Sec. II Rev. I, Nat'l. Technical Information Service, Sringfield, Virginia(1969).

8. P.R. Bevington; Data Reduction and Error Analysis for the Physical Sciences; McGraw-Hill Book Co.,Inc., N.Y.(1969) p. 57.

9. E.U. Condon and H. Odishaw; Handbook of Physics; McGraw-Hill Book Co. Inc., N.Y.(1967) p. 9-107.

10. W. Bambynek, B. Crasemann, R.W. Fink, H.-U. Freund, H. Mark, C.D. Swift, R.E. Price and P. Venugpala-Rao; Rev. Mod. Phys. (1972) 44, 716 - 813.

Table I

D Values for Neat Metals and Aqueous Solutions

Element(Z)	K Edge Energy[1] (KeV)	D Value	
		Neat Metal	Aqueous Sol'n (6.25×10^{-4} M)
Ca(20)	4.038	8.88×10^{-1}	2.96×10^{-4}
Mn(25)	6.540	8.80×10^{-1}	7.68×10^{-4}
Fe(26)	7.112	8.74×10^{-1}	8.84×10^{-4}
Cu(29)	8.979	8.69×10^{-1}	1.42×10^{-3}
Zn(30)	9.659	8.63×10^{-1}	1.66×10^{-3}
Mo(42)	19.999	8.45×10^{-1}	5.27×10^{-3}

Table II

D_F Values for Neat Metals and Aqueous Solutions

Element(Z)	Fluorescence Yield (K Shell)[2]	D_F Value	
		Neat Metal	Aqueous Sol'n (6.25×10^{-4} M)
Ca(20)	0.163	9.86×10^{-1}	5.20×10^{-3}
Mn(25)	0.313	9.86×10^{-1}	8.45×10^{-3}
Fe(26)	0.342	9.85×10^{-1}	8.72×10^{-3}
Cu(29)	0.443	9.84×10^{-1}	1.04×10^{-2}
Zn(30)	0.480	9.84×10^{-1}	1.11×10^{-2}
Mo(42)	0.760	9.79×10^{-1}	1.11×10^{-2}

Notes for tables I and II

1. Edge energies and cross section data for the calculation of D and D_F values were taken from reference 7.
2. Fluorescence yield values were taken from reference 9.

Table III

Minima in $E(\mu x)$ for F = 0.11, $N = 10^8$ and Various R Values

R(%T)[1]	$E_{min} \times 10^3$
2.30(10)	0.195
1.61(20)	0.204
1.21(30)	0.213
0.92(40)	0.226
0.69(50)	0.243
0.51(60)	0.264
0.36(70)	0.295
0.22(80)	0.353
0.11(90)	0.468
0.05(95)	0.668
0.01(99)	1.45

Table IV

Minima in $E(\mu x)$ for R = 2.30, $N = 10^8$ and Various F Values

F(%T)	$E_{min} \times 10^3$
2.30(10)	0.445
1.61(20)	0.325
1.21(30)	0.269
0.92(40)	0.234
0.69(50)	0.213
0.51(60)	0.199
0.36(70)	0.190
0.22(80)	0.187
0.11(90)	0.195
0.05(95)	0.219
0.01(99)	0.314

Notes for tables III and IV

1. % T means the per cent of the radiation that strikes the ion chamber that is trnasmitted through it.

Table V

Optimization[1] of F and μx for Fixed Values of R and N = 10^8

R(%T)[2]	Optimum F(%T)	Optimum μx(%T)	$E_{min} \times 10^3$
4.61(1)	0.261(77)	2.55(8)	0.180
2.30(10)	0.248(78)	2.52(8)	0.187
1.61(20)	0.221(80)	2.52(8)	0.196
1.20(30)	0.211(81)	2.49(8)	0.207
0.92(40)	0.198(82)	2.46(9)	0.220
0.69(50)	0.186(83)	2.46(9)	0.238
0.36(70)	0.186(83)	2.30(10)	0.293
0.22(80)	0.128(88)	2.29(10)	0.352
0.11(90)	0.094(91)	2.23(11)	0.468
0.05(95)	0.073(93)	2.15(12)	0.663
0.01(99)	0.030(97)	2.08(12)	1.410

Notes for table V

1. Equation 13 was used as a model for optimization of F and μx. A value of F was chosen and μx was varied to find the minimum value of E. A new value of F was then chosen and the optimization of μx was repeated. This procedure was repeated until the global minimum E was found.
2. % T means the per cent of radiation transmitted through the sample or ionization chamber.

Figure Captions

1. Schematic diagram of the EXAFS detection apparatus, showing the arrangement of detectors for incident, transmitted and fluorescence radiation.
2. The x-ray absorption coefficient for water in the energy range 1 - 25 KeV. The curve labeled "absorption + scattering" is the total attenuation of x-rays by scattering and photoabsorption. The curve labelled "scattering" describes the attenuation of x-rays due to scattering.
3. The relative error in μx as a function of μx. Curves were calculated for $N = 10^8$, $F = 0.11$ and R as indicated.
4. The relative error in μx as a function of μx. Curves were calculated for $N = 10^8$, $R = 2.3$ and F as indicated.
5. A comparsion of the experimental dependence of the relative error in μx on μx with the calculated prediction (smooth curve). The plotted points are the relative error values for the measurement of the absorbance of various thicknesses of a 0.2 M $FeCl_3$ solution.

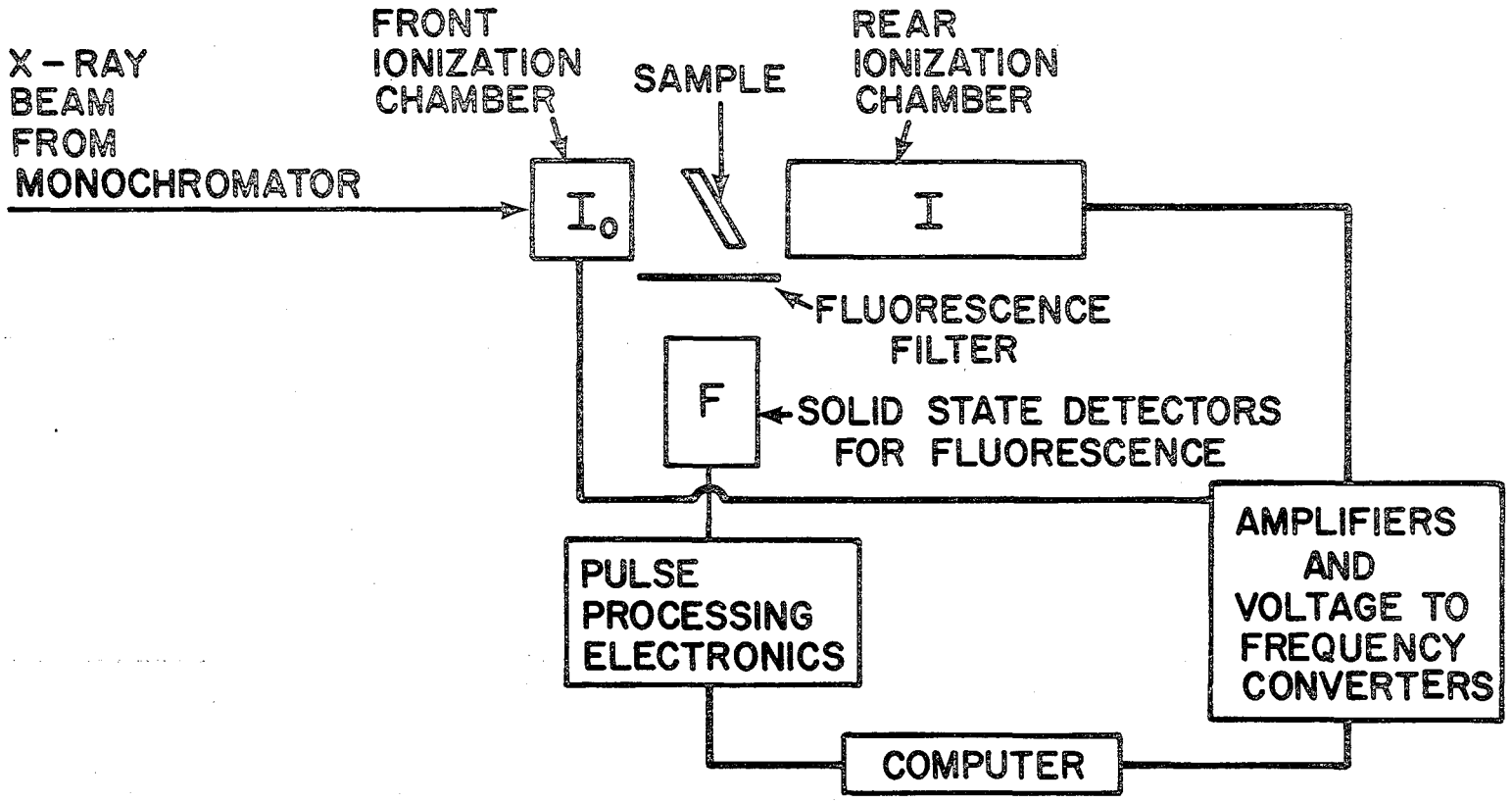

APPARATUS FOR EXAFS MEASUREMENT

XBL778-4525

Figure 1

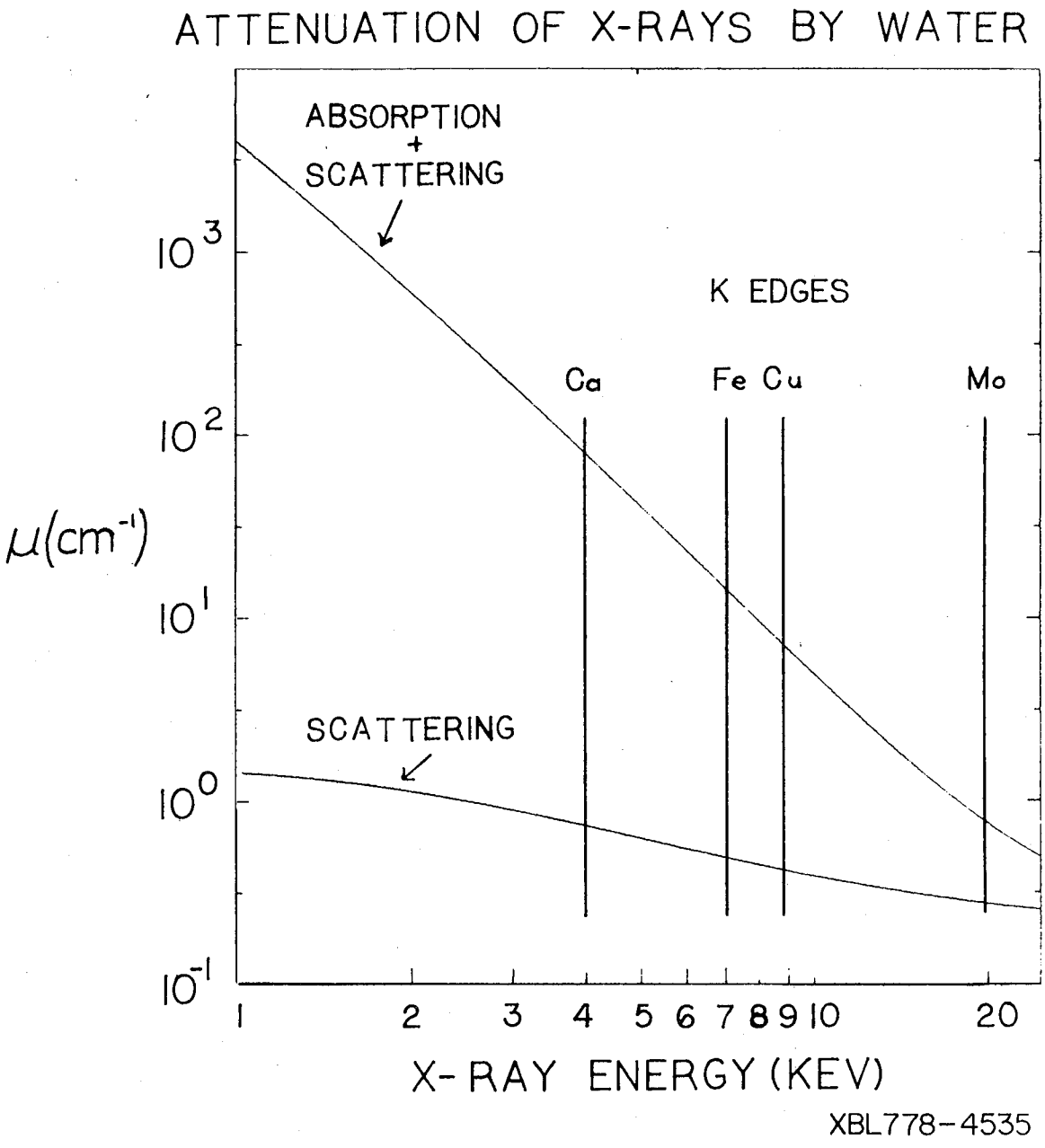
ATTENUATION OF X-RAYS BY WATER
ABSORPTION
+
SCATTERING
SCATTERING
K EDGES
Ca
Fe
Cu
Mo
μ(cm⁻¹)
10³
10²
10¹
10⁰
10⁻¹
1
2
3
4
5
6
7
8
9
10
20
X-RAY ENERGY (KEV)
XBL778-4535

Figure 2

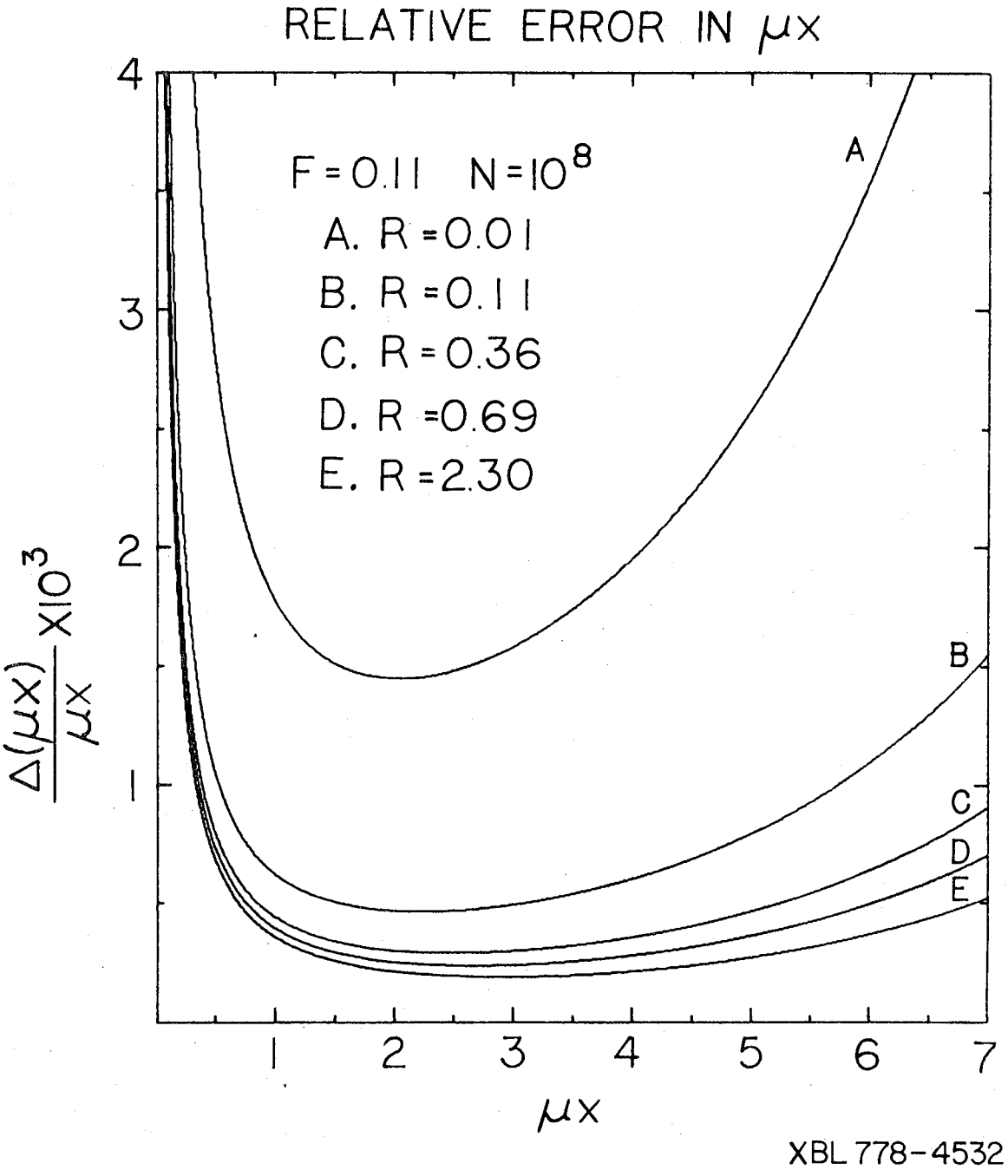
RELATIVE ERROR IN μx
F = 0.11 N = 10^8
A. R = 0.01
B. R = 0.11
C. R = 0.36
D. R = 0.69
E. R = 2.30
A
B
C
D
E
Δ(μx)/μx X10^3
μx
1
2
3
4
5
6
7
XBL 778-4532

Figure 3

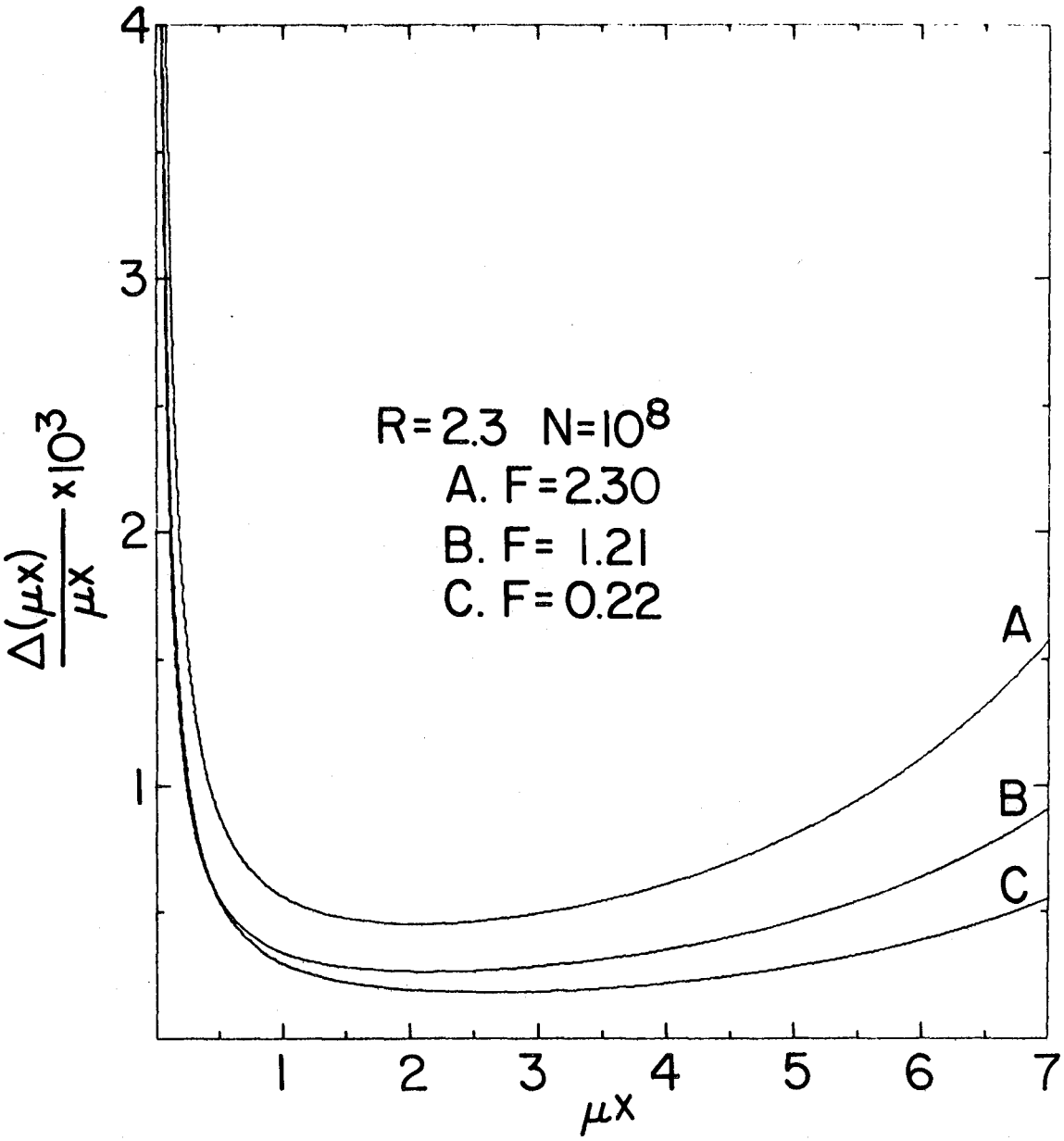

XBL 786-4037

Figure 4

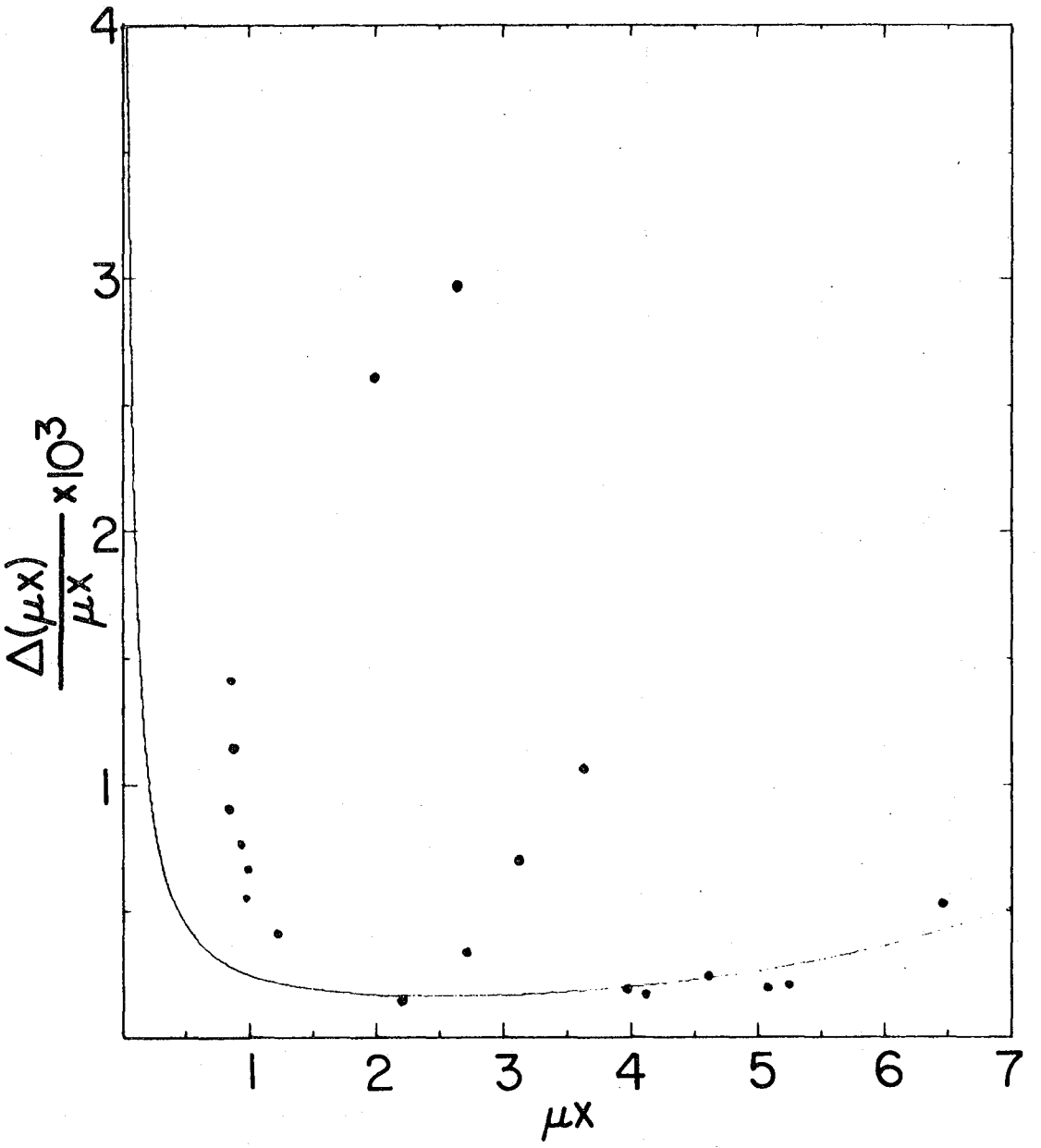

XBL 786-4035

Figure 5

Chapter VI

Growth of Azotobacter for Nitrogenase Production

The nitrogenase used in this work was prepared from Azotobacter vinelandii. The growth of hundred-gram quantities of this organism is required for the routine purification of nitrogenase components. The determination of optimum culture conditions for the production of nitrogenase was not the primary purpose of this work. However, considerable effort was expended in trying to obtain batches of Azotobacter cells with reproducibly high levels of nitrogenase. Efforts to establish growth conditions for reproducible Azotobacter grown in a bench scale fermentor were not completely successful. However, the experience gained during many trial fermentations serves as a basis for the discussion of the growth of Azotobacter for nitrogenase production.

Azotobacter are obligate aerobes and are noted for their remarkably high respiration rate.[1] Nitrogenase, on the other hand, is an enzyme that is irreversibly inactivated by oxygen. Therfore, when growing Azotobacter for the production of nitrogenase, a balance must be struck between the high oxygen demand of the organism's respiration and the inactivation of nitrogenase by over- aeration. The sensitivity of Azotobacter cultures to over-aeration is markedly increased when N_2 is

the sole source of nitrogen.[2] In the following paragraphs, we will describe the procedure used for growing Azotobacter in a bench scale fermentor and discuss the effects of growth conditions on the nitrogenase content of the harvested cells.

A. Bacterial Strain

The nitrogenase used in this work was prepared from Azotobacter vinelandii strain OP. Sample cultures of this organism were obtained from Dr. Duane Yoch of the University of California at Berkeley and from Dr. Winston Brill of the University of Wisconsin at Madison. The properties of cells subcultured from either source appeared to be identical.

B. Growth Medium

The medium used for the growth of Azotobacter was a modifed Burk's nitrogen free medium as described by Strandberg and Wilson[3]. The medium contained, per liter of solution; sucrose, 20 g; KH_2PO_4, 0.2 g; K_2HPO_4, 0.8 g; $MgSO_4 \cdot 7H_2O$, 0.2 g; $CaCl_2 \cdot 2H_2O$, 0.09 g; $FeCl_3$, 4.9 mg; and $Na_2MoO_4 \cdot 2H_2O$, 0.25 mg. Sucrose was added as a solid. Appendix I contains recipes for the preparation of stock solutions of inorganic salts used for media preparation. To prevent the formation of precipitates during sterilization, the phosphates were autoclaved separately. After sterilization, the phosphates were combined with the other ingredients.

Inorganic salts used for media preparation were reagent grade. A series of tests showed that the use of commercial grade sucrose had no effect on the nitrogenase content of the cells. Unless otherwise specified, commercial grade sucrose was used for media preparation.

C. Maintenance of Azotobacter Cultures

Azotobacter cultures were maintained on agar plates of Burk's medium. Appendix II gives a recipe for the preparation of the agar medium.

Agar plates were streaked with a growing suspension of Azotobacter. Incubation of the plates at 30 C for one week yielded dense, light brown colonies of bacteria. The plates were then wrapped in aluminum foil and stored in a refrigerator until needed.

It is interesting to note the Azotobacter excrete a bright yellow-green pigment into the agar when grown on this medium. Formation of this pigment can be supressed by the addition of citrate to the medium. Apparently, the yellow-green pigment is connected with bacterial iron metabolism. The production of a yellow-green pigment in lqiuid culture under low iron conditions has been reported in the literature.[4]

D. Procedure for Large Scale Liquid Culture

Large scale liquid culture of Azotobacter was carried out in three stages. A 50 ml starter culture was used to innoculate a 1 liter culture. The 1 liter culture was used as an innoculum fo a 10 liter batch culture grown in a bench top fermentor. By adding another 10 liters of sterile medium after harvesting the bacteria, the fermentor may be operated semi-continuously yielding a batch of cells every 9 - 12 hours. Details of the growth procedure are described below.

An agar plate maintenance culture was used to innoculate 50 ml of sterile medium in a 125 ml Erlenmeyer flask. The flask was then shaken for 24 - 36 hours at 30 C. This culture was used to innoculate the 1 liter culture.

One liter of medium was sterilized in a two liter reagent bottle. The bottle was sealed with a 3-hole rubber stopper. The stopper was fitted with a thermometer, a coarse fritted glass sparger for aeration and an air exit tube. The air inlet and outle tubes were fitted with glass wool filters to protect the sterility of the medium. The 1 liter

culture was innoculated with the 50 ml starter and was incubated, with aeration, for 24 hours at 30 C.

The New Brunswick Scientific (New Brunswick, N.J. 08903) Magnaferm fermentor with a 14 liter glass vessel was used for large scale liquid culture of Azotobacter. Dissolved oxygen was monitored with a Beckman model 39065 polarographic oxygen sensor. Optical densities of fermentor grown cultures were measured with a Klett-Summerson colorimeter with a KS-62 (red) filter.

For use in the fermentor the oxygen sensor was mounted on the end of a 10 inch long plastic rod that was stuck through a rubber stopper. Because the sensor is not autoclavable, the sensor and its mounting rod were disinfected with a 0.13 % solution of Zephiran Chloride (Winthrop Laboratories, N.Y.,N.Y. 10016) followed by rinsing with distilled water. After the fermentor, containing 9 liters of medium, was autoclaved and had cooled to room temperature, the oxygen sensor was inserted through the pH electrode port in the fermentor head plate. The sensor and its mounting rod were secured by firmly pressing the rubber stopper into the electrode port.

The oxygen sensor was calibrated before the beginning of the first batch of a fermentor run. The fermentor and its contents were equilibrated at 30 C. The fermentor vessel was gassed with 4 lpm N_2 with 600 rpm stirring. After an equilibration period of several minutes the output of the sensor was read and the 0 % air saturation level was defined. The vessel was then gassed with air at 4 lpm and 600 rpm stirring. The sensor output for 100 % air saturation was noted. We assumed a linear response between 0 % and 100 % saturation. It was found that changing the stirring speed from 100 to 800 rpm produced less than a 5 %

change in the output at 100 % saturation.

After temperature equilibration and oxygen sensor calibration, the fermentor was innoculated by pouring the 1 liter culture into the fermentor vessel through the innoculation port on the fermentor head plate. Aeration was started according to one of the three aeration procedures described in the discussion section. After 9 - 12 hours the culture was in exponential growth was an optical density of 100 - 170 Klett units. The culture was then harvested by siphoning the medium directly into the inlet of a Sharples continuous centrifuge. After the harvest, a small amount of medium was left in the fermentor vessel. This served as the innoculum for the next batch. 10 liters of sterile medium were added through a sterile addition port in the fermentor head plate to start the growth of the next batch.

In a series of batches grown in the fermentor, the first batch usually took the longest time to grow to harvest density. This was apparently due to a delay in the onset of exponential growth after innoculation. The time for succeeding batches to grow could be decreased by leaving a larger innoculum in the vessel after harvesting, or increased by lowering the temperature by a few degrees.

After harvesting, the cell paste was scraped out of the Sharples centrifuge bowl and placed into plastic jars for freezing at -20 C. In some instances the cell paste was frozen by dropping into liquid nitrogen. The brittle cake of frozen cells was then broken up into small pieces for storage at -20 C. Tests have shown that for short term storage, freezing in liquid nitrogen has no effect on the nitrogenase extracted from the cells. Liquid nitrogen freezing has one advantage in that the cells are frozen in small lumps which are easier to handle than

the the large cakes obtained by freezing the cells in a regular freezer. It has been reported that after many months in the freezer, Azotobacter cells become highly resistant to breaking by the osmotic shock methods used in this work.[5]

E. Discussion

In this section we will attempt to distill the experience gained in growing more than 70 batches of Azotobacter vinelandii in the Magnaferm fermentor into a useable set of growth conditions. It must be emphasized that we have found that Azotobacter will grow vigorously under a variety of conditions, but in some cases the cells obatined provide crude extracts with low nitrogenase specific activity. As a result, we have found the correct growth of Azotobacter to be the most crucial step in the preparation of nitrogenase from that organism. Some progress has been made in defining growth conditions for reproducible batches of Azotobacter grown in the Magnaferm fermentor. We have not been completely successful in obtaining batch-to-batch uniformity in the nitrogenase content of Azotobacter cells. In light of the success that other laboratories have reported in this regard[6,7], our results were particularly frustrating.

We have used the nitrogenase specific activity of the cell free crude extract as a measure of the quality of Azotobacter cell batches. This technique allows a rapid determination of the amount of nitrogenase present in a crude extract. The results presented in table I show that the specific activity of the crude extract is a good indication of how much molybdenum-iron component can be isolated from a given batch of crude extract.

For purposes of discussion, we will classify batches of Azoto-

bacter according to the nitrogenase specific activity of the cell free crude extract obtained from each batch. Extracts with specific activity less than 30 are classified as "poor". In general, the amount of nitrogenase obtainable from these extracts is not worth the effort required to purify it. Extracts with specific activity between 30 and 40 are classified as " acceptable" and extracts with specific activity in excess of 40 are classified as "good". In our experience, a batch of crude extract with acceptable or good specific activity will yield 1 mg of purified molybdenum-iron component protein for every gram of cell paste used. The highest crude extract specific activities we have observed have been between 55 and 60.

In experimenting with different growth conditions, our main effort was directed towards establishing the optimum conditions of aeration of the fermentor grown cultures. Early experiments indicated that the concentrations and sources of the other nutrients in the medium were not responsible for the batch-to-batch variations we observed. Comparison of cells subcultured from two independent sources of Azotobacter vinelandii indicated that contamination of our strain of Azotobacter was not a factor. In early experiments with carboy-grown batches of Azotobacter, we observed that the pH of our crude extracts was sometimes as low as 6.5, altough the buffer used was at pH 7.4. Discussion of this result with workers at the University of Wisconsin[6] lead us to conclude that it was a symptom of Azotobacter that had been oxygen starved during growth. This lead to experimentation with aeration conditions and to the use of the Magnaferm fermentor, a device that allows very vigorous aeration. In general, of all the conditions used for the growth of aerobic microorganisms, aeration conditions are the most difficult to

specify and reproduce. In a rapidly growing culture, the supply of oxygen to the organsims is determined not only by the rate of air flow into the vessel per volume of medium, but also by the degree of dispersion of the air, the method and speed of stirring and the geometry of the fermentor.

In this work, we have tried three distinct approaches to the aeration of Azotobacter cultures grown in the Magnaferm fermentor. These approaches will be described below, along with a brief discussion of their relative merits.

The first method that was tried was the constant aeration method, which we will refer to as method A. In method A, the fermentor batch is started at a constant airflow rate and stirring speed. The initial airflow rate and stirring speed are maintained throughout the growth of the batch. The initial aeration conditions must be sufficiently vigorous to insure a non-zero oxygen concentration throughout the growth of the batch, This is the simplest sort of aeration to describe in detail. Several groups have reported success with this method for fermentor and carboy grown cultures.[8,11]

In method B, the culture is started on a low initial airflow and stirring speed. When exponential growth starts, the airflow and stirring speed are increased to a level which is maintained for the remaining growth of the batch. In this work, typical initial aeration conditions were 1 lpm air with 300 rpm stirring. The aeration was increased when the culture reached a density of about 40 Klett units. Typical final aeration conditions were 3 lpm air with 400-600 rpm stirring. The method B aeration technique gives some consideration to the known sensitivity of low density Azotobacter cultures to over-aeration.[2]

The third aeration technique that we employed was the controlled aeration method, which we will call method C. In method C, a constant, lower than saturation level of oxygen tension is maintained throughout the growth of the batch. This was accomplished by manually adjusting the airflow and stirring speed in response to the output of the dissolved oxygen sensor. It might be expected that an optimum oxygen tension exists for the growth of Azotobacter under nitrogen fixing conditions. The optimum oxygen tension would balance the respiratory requirements of Azotobacter against the sensitivity of nitrogenase to inactivation by oxygen. The work of Drozd and Postgate[9] suggests that such an optimum oxygen tension does in fact exist. However, it is not clear how to relate the in vivo acetylene reduction activities reported by Drozd and Postgate to the actual nitrogenase level in the cell. With our present equipment, the manual control of dissolved oxygen was sufficiently tedious and imprecise that a systematic study of the yield of nitrogenase as a function of dissolved oxygen concentration during growth was impractical. The fact that nearly constant operator attention is required to use method C aeration with our present equipment is a definite disadvantage.

The first point to note when comparing aeration techniques for the growth of Azotobacter is that the oxygen demand of a rapidly growing culture of Azotobacter is very high. Even with very vigorous aeration, the dissolved oxygen concentration of an exponentially growing culture of Azotobacter will be sufficiently lower than saturation. In figure 1, the oxygen tension and optical density of an Azotobacter culture grown with type A aeration are plotted as a function of time. This plot shows that even with very vigorous aeration (16 lpm air with 800 rpm stirring)

the oxygen concentration begins to drop as soon as exponential growth begins.

Figure 2 shows the growth of an Azotobacter culture under method C aeration. Although the exponential phase slopes of figures 1 and 2 are similar, it should be noted that the onset of exponential growth occurs about 9 hours earlier in figure 2. This result is consistent with the report that a sudden increase in aeration of a growing culture of Azotobacter will cause a lag of several hours before the resumption of growth.[10]

In table II, the results of a number of batch cultures of Azotobacter in the fermentor are listed. The aeration conditions are specified as being type A,B or C. On the basis of crude extract specific activities, these results do not clearly establish which aeration method is the technique of choice. Type B or C aeration tends to get the culture growing faster and these methods are preferred for that reason. The results obtained with type C aeration were not consistently better than those obtained with type B aeration. It is possible that automatic control of the dissolved oxygen level might give better results than our present manual control method. With our present equipment, the results of type C aeration do not justify the tedium necessary to implement that technique.

F. Summary

Notwithstanding a lack of complete reproducibility of the results presented in table II, we can make some generalizations about what sort of aeration conditions are most likely to be successful. Using type B or C aeration, the best results were obtained with a final airflow of 2 - 4 lpm with 300 - 500 rpm stirring. A very definite improvement in

crude extract specific activities occurred when the maximum aeration rate was lowered from 16 lpm air with 600 - 800 rpm stirring.

The nitrogenase content of Azotobacter is apparently a function of the culture density at the time of harvest. The Magnaferm fermentor will support very dense growth of Azotobacter. We have observed optical densities well in excess of 300 Klett units. Cell growth data shows that single phase exponential growth can be supported to a density of about 130 - 160 Klett units. We did not establish a maximum density for exponential growth in these experiments. We have obtained crude extracts with good or acceptable specific activities from cell batches harvested at densities from 100 - 200 Klett units. Our best batches were harvested at densities below 160 Klett units. Above a harvest density of 200 Klett units, the specific activity of crude extracts suffers a marked decrease. With the exception of one batch (#42), we have never recorded a crude extract specific activity in the good class for a cell batch whose harvest density was in excess of 210.

From the data presented in table II, it is not possible to clearly distinguish between the effects of high harvest density and oxygen starvation on the nitrogenase content of Azotobacter. In many cases, batches that were grown to a high harvest density were also anerobic for several hours before harvesting. For the present discussion, "anerobic" will mean an apparent dissolved oxygen concentration of zero even in the presence of aeration. In other words, the bacteria are consuming oxygen faster than it can be dissolved in the medium. Periods of anerobicity of 3 or more hours, at any harvest density, led to a marked reduction of crude extract specific activity. In a few instances, we have obtained crude extracts of acceptable specific activity from cell

batches that were harvested at low density even after 1 - 3 hours of anerobicity.

References

1. J.W.T. Wimpenny; Symposia of the Society for General Microbiology, S.J. Pirt and P.M. Meadow, eds.(1969)19, 161-199.

2. H. Dalton and J.R. Postgate; J. Gen. Microbiol.(1969)54,463-473.

3. G.W. Strandberg and P.W. Wilson, Can. J. Microbiol.(1968)14, 25-31.

4. W.A. Bulen and J.R. LeComte; Biochem. Biophys. Res. Commun.(1962) 9, 523-528.

5. L.C. Davis; personal communication.

6. V.K. Shah; personal communication.

7. J.R. Postgate; personal communication.

8. J.M. Rivera-Ortiz and R.H. Burris; J. Bacteriol.(1975)123, 537-545.

9. J. Drozd and J.R. Postgate; J. Gen. Microbiol.(1970)63, 63-73.

10. C.W. Jones, J.M. Brice, V. Wright and B. Ackrell; Fed. Eur. Biochem. Soc. Lett.(1973)29, 77-81.

11. V.K. Shah,L.C. Davis,J.K. Gordon, W.H. Orme-Johnson and W.J. Brill; Biochem. Biophys. Acta(1973)292, 246-255.

Table I

Relation of Crude Extract Specific Activity[1] to Yield[2] and Specific Activity[3] of the Mo-Fe Component of Nitrogenase Isolated From Azotobacter vinelandii

Crude Extract Specific Activity	Mo-Fe Component Specific Activity	Mo-Fe Component Yield
51	1649	158
44	1555	125
41	1548	134
41	1775	108
39	1759	108
27	1326	21
23	1428	32

1. The units of crude extract specific activity and Mo-Fe component specific activity are nanomoles of ethylene produced per minute per milligram of protein.
2. Yield is given in units of mg of protein. The data were taken from seven separate preparations, each starting with about 9 g of crude protein.
3. Assay techniques are described in the chapter on the nitrogenase assay.

Table II

Summary of Growth Experiments with the Magnaferm Fermentor

Batch #	Crude Extract Specific Activity	O.D. at Harvest (Klett units)	Type of Aeration	Comments [1,2,3]
1	23	208	A	28 ^{o}C, 16 lpm air, 500 rpm, Burk's medium.
2	29	193	A	28 ^{o}C, 16 lpm air, 400 rpm, S+W+0.2 g/l NaCl + citrate.
3	4	280	A	28 ^{o}C, 16 lpm air, 400 rpm, S+W+0.2 g/l NaCl + citrate.
4	27	179	A	28 ^{o}C, 10 lpm air, 600 rpm, S+W+citrate.
5	34	195	A	16 lpm air, 600 rpm, S+W+citrate.
6	36	182	A	16 lpm air, 600 rpm, reagent grade sucrose.
7	16	274	A	16 lpm 25% O_2 - 75% N_2, 600 rpm, S+W+citrate.
8	14	136	A	16 lpm 25% O_2 - 75% N_2, 600 rpm, S+W+citrate, went anerobic before harvest.
9	22	151	A	16 lpm air, 500 rpm, S+W+citrate.
10	23	142	A	16.5 lpm air, 600 rpm, 8 liters total volume.
11	23	145	A	16 lpm air, 600 rpm, 8 liters total volume.
12	32	127	A	16 lpm, 600 rpm, tank air.
13	17	145	A	16 lpm air, 600 rpm.
14	12	155	A	16 lpm tank air, 600 rpm, Fe-Mo solution made fresh.
15	11	125	A	16 lpm tank air, 600 rpm, Fe-Mo solution made fresh, S+W+citrate.
16	13	138	A	16 lpm tank air, 600 rpm, S+W+citrate.
17	7	70	A	16 lpm, 600 rpm.

Table II(cont'd)

Batch #	Crude Extract Specific Activity	O.D. at Harvest (Klett units)	Type of Aeration	Comments
18	5	70	A	16 lpm, 600 rpm (first use of O_2 sensor).
19	15	63	A	16 lpm, 700 rpm.
20	3	77	A	16 lpm, 700 rpm, S+W+ 1 ppm Mo and 3 ppm Fe Mo-Fe sterilized separately.
21	13	135	A	16 lpm, 800 rpm, Fe-Mo added non-sterile.
22	14	85	A	16 lpm, 700 rpm, Mo-Fe added non-sterile, 3 ppm Fe.
23	39	136	C	800 rpm.
24	27	118	C	30% saturation maintained, went anerobic 1 hour before harvest.
25	40	160	B	2 lpm, 800 rpm.
26	42	179	B	2 lpm, 800 rpm.
27				Individual batch assay data not available.
28				"
29				"
30				"
31				"
32				"
33	41	124	C	3.5 lpm, 800 rpm, activity is average of #33-35
34	41	150	B	3.5 lpm, 800 rpm.
35	41	139	B	3.5 lpm, 800 rpm.
36	32	200	B	3.5 lpm, 800 rpm.

Table II(cont'd)

Batch #	Crude Extract Specific Activity	O.D. at Harvest (Klett units)	Type of Aeration	Comments
37	59	175	C	3 lpm air, 800 rpm.
38	46	155	B	25 ^{o}C, 2.5 lpm at start, 2.0 lpm at end.
39		132		Assay data not available.
40	39	130	C	800 rpm, 15%-50% saturation maintained.
41	44	170	B	25 - 27 ^{o}C.
42	41	250	B	3 lpm, 800 rpm, 25^{o}C, went anerobic 2 hours before harvest.
43	56	105	C	3 lpm, 800 rpm(final conditions).
44	46	164	C	3 lpm, 800 rpm(final conditions).
45	56	128	A	2 lpm, 800 rpm.
46	34	141	C	2 lpm, 800 rpm(final conditions).
47		270		Assay data not available.
48		169		"
49	34	117	A	3 lpm, 800 rpm, 23^{o}C.
50		210		Assay data not available.
51	34	120	A	3 lpm, 800 rpm, 27 ^{o}C.
52		118		Assay data not available.
53	36	136	B	2 lpm, 450 rpm initially, increase at end to 650 rpm.
54	43	133	B	2 lpm, 450 rpm, went anerobic 3 hours in mid-run, 4 lpm air, 700 rpm final conditions.
55	38	157	A	3 lpm, 600 rpm.

Table II(cont'd)

Batch #	Crude Extract Specific Activity	O.D. at Harvest (Klett units)	Type of Aeration	Comments
56	30	133	B	2 lpm, 450 rpm initially, at O.D. = 57 increase stirring to 550, at O.D. = 133 increase to 600 rpm.
57	31	185	B	2 lpm, 450 rpm, increase after 3 hours to 550 rpm, went anerobic 2 hours before harvest.
58	43	167	B	2 lpm, 450 rpm, at O.D. = 44 set stirring to 500 rpm, 8 hours later set to 650 rpm.
59	35	205	B	2 lpm air, 450 rpm, after 3 hours set to 600 rpm went anerobic 2 hours before harvest.
60	21	161	A	3 lpm, 600 rpm.
61	21	151	B	2 lpm, 600 rpm, at O.D. = 94 set to 3 lpm, at O.D.= 140 set to 650 rpm.
62	23	110	A	3 lpm, 600 rpm.
63	26	122	A	3.5 lpm, 600 rpm.
64	27	151	A	Went anerobic three hours before harvest.
65	44	143	B	2 lpm, 450 rpm, at O.D.=30, set to 550 rpm, at O.D.=60 set to 600 rpm, with 3 lpm, argon induce.
66	58	146	C	28^{o}C, 2.5 lpm, 450 rpm, at O.D.=74 increase temperature to 30^{o}C, stirring to 550 rpm, at O.D.=89 increase stirring to 600, at O.D.=104 increase air ti 3 lpm, argon induce.
67	10	220	A	2.5 lpm, 450 rpm, went anerobic 4 hours before harvest, argon induce.
68				Assay data not available.
69	24	146	C	2 lpm, 450 rpm, at O.D.= 50 set to 3 lpm, 600 rpm, at O.D. = 140, argon induce.

Table II(cont'd)

Batch #	Crude Extract Specific Activity	O.D. at Harvest (Klett units)	Type of aeration	Comments
70	28	144	C	3 lpm, 550 rpm; at O.D. = 47 , 500 rpm; at O.D. = 95, 600 rpm; argon induce at O.D.=132.
71	28	132	C	2.75 lpm, 400 rpm; at O.D.= 108, 600 rpm, 3.25 lpm; at O.D.=123, argon induce.

Table II(cont'd)

Explanatory Notes for Table II

1. Unless otherwise specified, fermentor batches were grown at 30 ^{o}C using the modified Burk's medium described in reference 3. Any modifications of this medium are indicated by S+W.... and indicating the addition. The normal total volume of the batch was 10 liters. The normal source of air was a diaphragm pump compressor that supplies house compressed air.
2. Citrate, when used, was added to the medium at the same concentration as iron.
3. Some early experiments were done with Burk's medium. This medium differs from the modified Burk's in that it contains 0.2 g/l NaCl and 3ppm Fe and 1 ppm Mo.
4. A limited series of test of the "argon induction of nitrogenase" effect was performed. In these experiemnts the cells were grown to mid-exponential phase when the gas atmosphere in the fermentor was changed to 20% O_2 - 80% argon. The idea is to stimulate the production of nitrogenase by starving the cells for N_2. This technique was suggested by John Benneman of the University of California.

Appendix I

Stock Solutions

The following stock solution were prepared for use in the routine preparation of media.

1. Fe-Mo solution : Dissolve 0.126 g $Na_2MoO_4 \cdot 2H_2O$ and 4.11 g $FeCl_3 \cdot 6H_2O$ in water and dilute to 500 ml. Add 1.0 ml per liter of medium.
2. Mg solution : Dissolve 50 g $MgSO_4 \cdot 7H_2O$ in water and dilute to 250 ml. Add 1.0 ml per liter of medium.
3. Ca solution : Dissolve 22.5 g $CaCl_2 \cdot 2H_2O$ in water and dilute to 250 ml. Add 1.0 ml per liter of medium.
3. Phosphate solution : Dissolve 262 $K_2HPO_4 \cdot 3H_2O$ and 50 g KH_2PO_4 in water and dilute to 1 liter. Add 4.0 ml per liter of medium.

Appendix II

Agar Medium

To prepare enough agar medium for 20 Petri dishes (10 cm diameter) mix 18 g Difco Bacto-Agar with 300 ml water. Prepare 300 ml of solution with enough sucrose and salts for 600 ml medium. As with the preparation of liquid medium, prepare the phosphates for sterilization in a separate flask. Autoclave all three solutions. While the solutions are still warm, combine them and pour the mixture into the bottoms of 20 sterile Petri dishes. Cover the dishes and allow them to set before moving the plates.

Figure Captions

1. Plot of the optical density and dissolved oxygen level for an Azotobacter vinelandii culture in exponential growth. Aeration is by method A with 16 lpm air and 800 rpm stirring.
2. Plot of the optical density as a function of time for an Azotobacter vinelandii culture in exponential growth. Aeration is by method C.

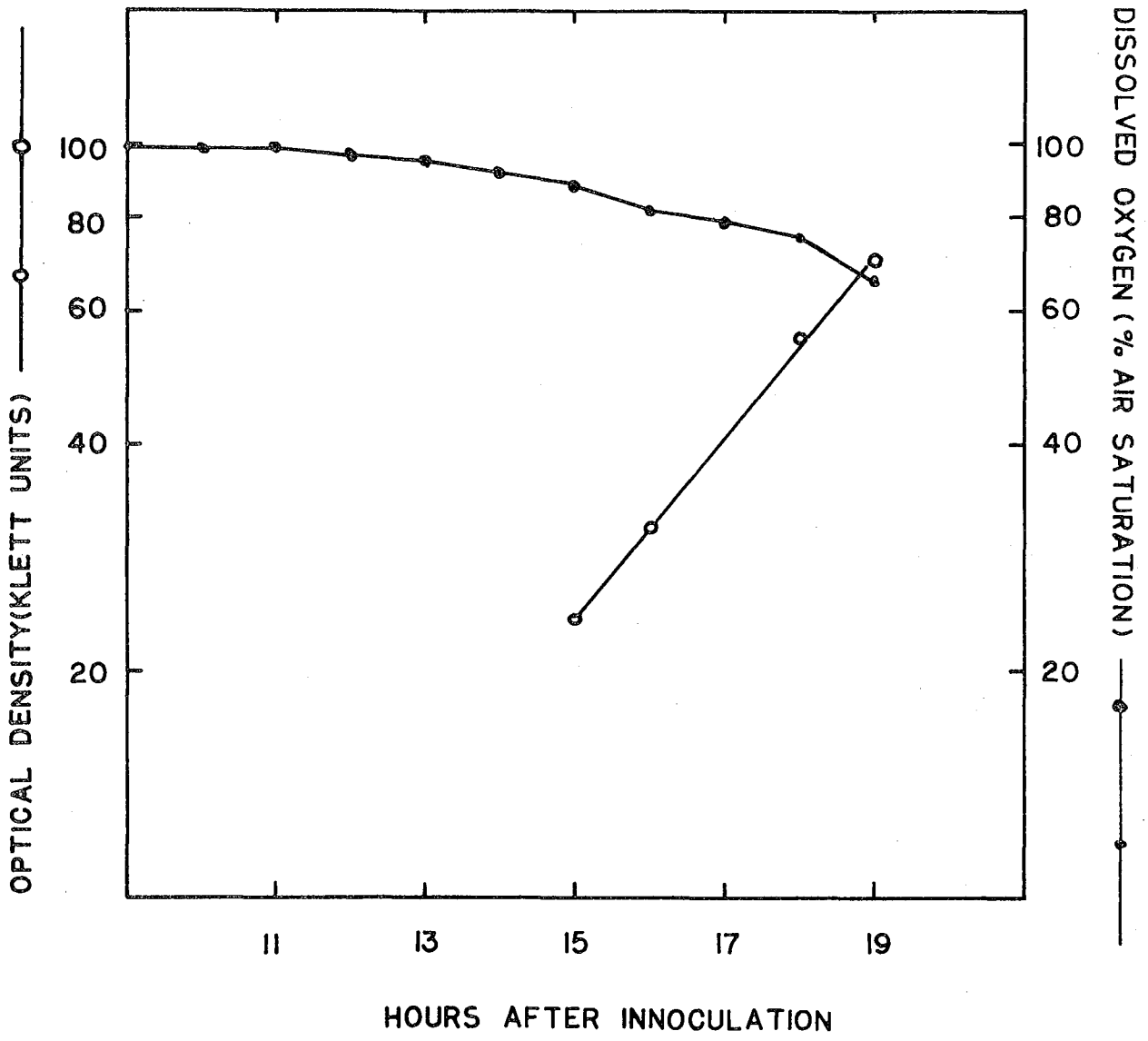
OPTICAL DENSITY(KLETT UNITS)
100
80
60
40
20
DISSOLVED OXYGEN (% AIR SATURATION)
100
80
60
40
20
11
13
15
17
19
HOURS AFTER INNOCULATION
XBL781-3775

Figure 1

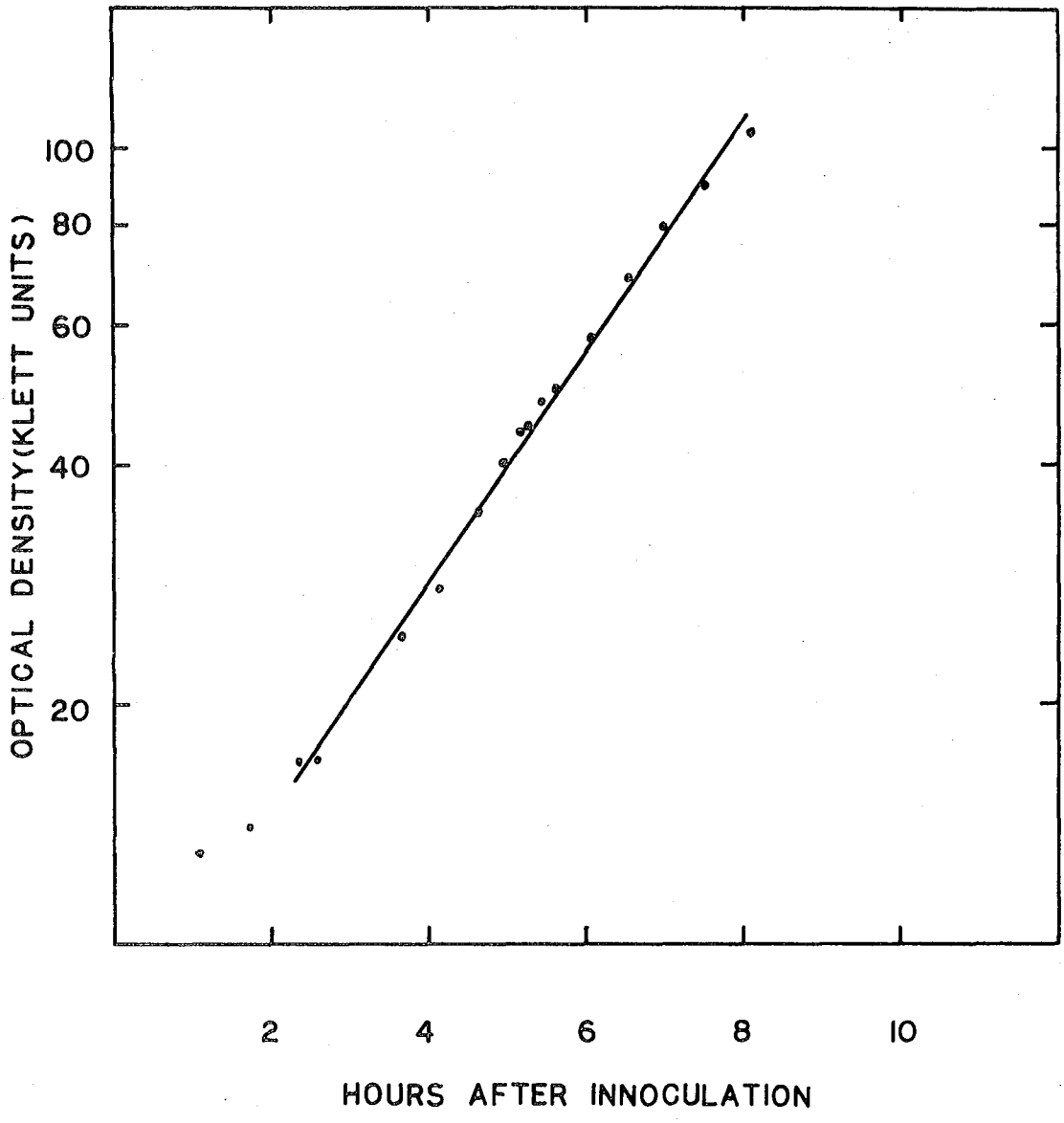

XBL 781-3776

Figure 2

Chapter VII

Procedures for the Preparation of Nitrogenase

In this section, we will describe the procedures employed for the preparation of the nitrogenase components used in this work. The purification procedure that was used follows very closely the method developed by Shah and Brill.[1] For the sake of completeness and clarity, the details of the procedures used will be reported in the following paragraphs. Concise summaries of the procedures are presented in a series of flow charts in appendix I of this chapter.

A. General Anerobic Technique

Because of the well known oxygen sensitivity of nitrogenase components, an anerobic environment must be maintained at all times. All buffers used in this work were sparged with nitrogen or argon gas before use. For small scale procedures, anerobic buffers were prepared in 60 ml septum stoppered bottles by several cycles of evacuation and filling with argon gas. Unless otherwise specified, all buffers used in this work contained 0.4 mg/ml sodium dithionite which was added as a solid to the oxygen free buffer just before use. Buffer reservoirs for column chromatography procedures were continuously sparged with nitrogen gas. Gases used during the handling

of nitrogenase components were rendered oxygen free by passing them over a column of BTS catalyst (BASF Chemical Corp.).

When it was necessary to store nitrogenase preparations between steps in the purification procedure, the following technique was used. Nitrogenase fractions, in 60 ml septum stoppered bottles, were subjected to several cycles of evacuation and filling with argon gas. The bottles were then frozen by placing them in the freezer. When the samples had to be thawed, the bottles were again evacuated and filled with argon and were then rapidly thawed by immersion in warm water.

B. Buffers

The buffer used for the preparation of Azotobacter nitrogenase was 0.025 M Tris-HCl, pH 7.45. Throughout the rest of this chapter, this buffer will be referred to as DTRIS. In several steps in this procedure, various concentrations of NaCl will be used in this buffer. For example, a buffer that is 0.25 M in NaCl and 0.025 M in Tris-HCl at pH 7.45 will be referred to as 0.25 M NaCl-DTRIS.

For routine buffer preparation, a stock solution of 0.25 M Tris-HCl was prepared at a pH of 7.3 - 7.4. NaCl was added as necessary as a 2.0 M solution in distilled water. The pH of Tris solutions was foumd to be dependent on the ionic strength of the solution. As a result, it was necessary to make a final pH adjustment after Tris and NaCl stock solutions had been added and the buffer diluted to about 90% of its final volume. A 1.0 M solution of NaOH was used for pH adjustment. Unless otherwise specified, this and all other procedures were carried out at room temperature.

C. Cell Fracture Procedure

Azotobacter vinelandii cells were broken by a modification of the osmotic shock technique of Robrish and Marr.[2] The cell free extracts provided by this procedure are less sensitive to oxygen than are more highly purified nitrogenase preparations.[3] Therefore, the strictly anerobic conditions usually maintained in the handling of nitrogenase may be relaxed to some extent.[3] The large centrifuge bottles used in the course of the cell fracture procedure were occasionally opened to the air for the purpose of adding buffers or decanting supernatant fluids. To minimize contact with atmospheric oxygen the bottles were flushed with a stream of nitrogen gas while they were uncapped. The crude extract solution was manipulated under a stream of nitrogen until it could be transferred to septum stoppered bottles. In some early experiments, the cell breakage procedure was performed in a glove box under a nitrogen atmosphere. The cell breakage procedure was considerably more time consuming and tedious when performed in this fashion. We observed no decrease in the crude extract nitrogenase specific activity when we switched to the procedure described below.

A typical nitrogenase preparation started with breaking open approximately 100 g of Azotobacter cells. The osmotic shock procedure was conveniently performed in batches using 30 g of cell paste per batch. Several 30 g batches could be processed simultaneously. The volumes of buffer described below will pertain to the processing of one batch.

30 g of frozen cell paste were broken up into small chunks. The chunks were placed in a 250 ml plastic centrifuge bottle along with a magnetic stirring bar. The cells were covered with 120 ml of DTRIS.

The bottle was placed on a magnetic stirrer and the contents were stirred until the cells were thoroughly suspended in the buffer. The magnetic stirring bar was then removed. The cells were pelleted by centrifugation at 8000 X g for 30 minutes. For a Sorvall GSA rotor, 8000 X g is approximately 7000 rpm.

After centrifugation, the supernatant was poured off and the cells were resuspended in 120 ml of 4 M glycerol DTRIS. The suspension, in a capped centrifuge bottle, was stirred on a magnetic stirrer for 40 - 50 minutes. After removing the stirring bar, a few crystals of DNAase II (Sigma Chemical Corp.) were added. The cells were pelleted by centrifugation at 8000 X g for 20 minutes.

After centrifugation, the glycerol containing supernatant was poured off along with any loosely sedimented material. 120 ml of DTRIS were measured out into a nitrogen flushed graduated cylinder. The cell pellet was broken up with a spatula and three magnetic stirring bars were added to the bottle. The measured DTRIS was quickly poured into the centrifuge bottle. The bottle was capped and immediately shaken with great vigor for about 15 seconds. After shaking, the suspension in the bottle was usually quite viscous. After removing the stirring bars with a magnet, a few crystals of DNAase II were added to the suspension. Centrifugation at 13000 X g (10,000 rpm in the Sorvall GSA rotor) pelleted cell debris and unbroken cells. The supernatant was decanted into a graduated cylinder under a flush of nitrogen. The total extract volume was noted and the extract was parceled out into 60 ml septum stoppered bottles for storage.

We have observed that crude extracts that are very dark brown in

color usually have a fairly high nitrogenase specific activity. Although we have noted some inconsistencies in the correlation of extract color with nitrogenase content, we usually find that extracts that are light brown in color have low nitrogenase specific activities.

D. Chromatographic Techniques

In this section we will describe aspects of chromatographic technique common to all of the column chromatography procedures used in the preparation of nitrogenase. The details of the equipment used are reported for completeness, although other types of apparatus may give satisfactory performance.

Glass chromatographic columns with plastic end fittings (Kontes Glass Co., Berkeley,California) 25 cm X 2.5 cm were used for ion exchange and gel filtration chromatography. The outlet tubes of the columns were fitted with male Luer fittings for connection to disposable hypodermic needles. The tops of the columns were sealed with large, sleeve-type septum stoppers. The top septa were usually pierced by three or four needles. Two of the needles provided an inlet and outlet for flushing the column dead space with nitrogen gas. The third and fourth needles were used as inlets for samples to be loaded onto the columns or for eluting buffers. Fractions were collected in 60 ml septum stoppered bottles that had been filled with argon . To prevent pressure buildup in the bottles, the fractions were collected while the bottles were flushed with a slow stream of nitrogen. The nitrogen was vented to the outside air. Connections between the buffer reservoirs or gas sources and columns or fraction bottles were made with polyethylene spaghetti tubing. Eluting buffers were dispensed from 500 or 1000 ml aspirator bottles. Fritted glass spargers were used for the

deoxygenation of buffers and for the maintenance of anerobic conditions inside buffer reservoirs.

The large sample used in the first chromatographic separation on DEAE cellulose was dispensed from an 800 ml separatory funnel. The outlet of the funnel was mated to a glass "Y" connector fitted with two male Luer connections. Using disposable hypodermic needles and spaghetti tubing, the separatory funnel was connected to the chromatographic columns. The smaller samples used in the later chromatographic steps were loaded by injection directly into the dead space at the top of chromatographic columns.

The media used for chromatographic work were Whatman DE-52 microgranular DEAE cellulose and Bio-Rad Laboratories P-6 Biogel. The preparation and pouring of columns of these materials were carried out as per the instructions of the manufacturers. Particular care was taken to insure that the DEAE cellulose was properly equilibrated with DTRIS prior to use.

E. Initial Separation of Components I and II

The intial separation of nitrogenase components I and II was carried out on two DEAE cellulose columns operated in parallel. Two columns of DEAE cellulose (20 cm X 2.5 cm) were prepared. Each of the columns was washed overnight with 500 ml of DTRIS containing 1.0 mg/ml sodium dithionite. The frozen samples of crude extract (about 9 g of crude protein, at 20 mg/ml) were thawed as described above. Immediately prior to use, the columns were washed with 100 ml of DTRIS containing 0.4 mg/ml sodium dithionite. It should be noted at this point that as the dithionite-containing buffer passes down the column bed, the DEAE cellulose turns from its usual pale yellow color to a pure white. This

color change can be used to indicate when the column is in a fully reduced state.

The separatory funnel for dispensing the crude extract was flushed with nitrogen. The tubing from the separatory funnel to the chromatographic columns was rendered oxygen free by flushing with nitrogen followed by filling with DTRIS containing dithionite. The thawed crude extract was poured into the separatory funnel. A flush of nitrogen was maintained over the top of the crude extract throughout the procedure.

The sample was then loaded onto the columns. 20 ml of sample were loaded onto each of the columns followed by washing with 30 ml of DTRIS. This procedure was repeated until all of the sample had been loaded onto the colums. This method allows loosely adsorbed material to be washed off and permits the loading of larger amounts of nitrogenase onto the columns. By the completion of the sample loading procedure the top third of the columns beds were dark brown in color and the lower part of the column beds were pale brown or reddish in color. Washing with DTRIS was continued until the eluate was clear. This required about 100 ml of DTRIS per column.

Components I and II were eluted by stepwise increases in the NaCl concentration. The columns were washed with 0.1 M NaCl DTRIS. After 70 - 90 ml of 0.1 M NaCl DTRIS had passed through each column, the main dark area was about halfway down the column bed. At this point, washing with 0.25 M NaCl DTRIS was started.

A very dark band formed at the 0.25 M NaCl front. This band contained component I and was collected anerobically as a single fraction. This fraction will be referred to as AvI-1D. After most of the dark brown band had been eluted, washing with 0.5 M NaCl DTRIS was initiated.

A greenish-gray band formed at the 0.5 M NaCl front and was collected as a single fraction. In some preparations, the greenish-gray band appeared to have a brown leading edge. The greenish-gray fraction contained component II and small amounts of component I and it was referred to as AvII-1D.

F. Heat Treatment of Component I

Contaminating heat sensitive proteins were removed from the AvI-1D fraction by a heat treatment step. The argon atmosphere in the septum stoppered bottles containing the AvI-1D was replaced with hydrogen. A 52 ^{o}C water bath was prepared. The bottles containing the AvI-1D were immersed, with gentle agitation, in the hot water bath, After 5 minutes, a gray, scummy precipitate had formed. The bottles were placed in an ice bath to cool.

Removal of the gray precipitate was accomplished by anerobic centrifugation. Centrifuge bottles for this purpose were constructed according to the following design suggested by V.K. Shah.[3] A Beckman polycarbonate centrifuge bottle assembly (part # 338827, intended for use in the 60Ti rotor) provided the basic materials. This size tube can be adapted to fit the Sorvall SS-34 rotor. A hole big enough for a 20 gauge hypodermic needle was drilled into the cap insert of the centrifuge bottle cap assembly. (See figure 1.) The sleeve part of a small septum stopper was cut off and the stoppper was stuck into the well of the cap insert. When the cap insert was placed in the centrifuge bottle and the screw on cap was tightened, pressure on the rubber septum made a good compression fit seal. This tube may be evacuated and flushed with an oxygen free gas and filled or emptied with a long hypodermic needle. This sort of centrifuge bottle was used for all the

small scale anerobic centrifugations that were done in the course of the nitrogenase preparation.

The heat treated AvI-1D was loaded into a hydrogen filled anerobic centrifuge bottle. The gray precipitate was pelleted by centrifugation at 10,000 X g (10,000 rpm in the Sorvall SS-34 rotor) for 30 minutes at 0 C. After centrifugation, the supernatant was withdrawn with a long needle and stored under an argon atmosphere.

The next step was concentration of the heat treated component I solution prior to a second chromatography procedure. Amicon Corporation (Lexington, Massachusetts) stirred ultrafiltration cells were used for all concentration steps in this work. The stirred ultrafiltration cell provided an ideal geometry for anerobic technique. The cell could easily be flushed with oxygen free gas and then rendered anerobic by washing the ultrafiltration membrane with 20 - 30 ml of buffer containing dithionite. For concentration of component I, an Amicon XM50 membrane was employed. The cell was assembled, flushed with argon or nitrogen, and filled with 0.25 M NaCl DTRIS. 20 - 30 ml of this buffer were then forced through the membrane under 10 - 30 psi pressure. Any remaining buffer was then removed under a rapid flush of oxygen free gas. After loading the sample into the cell by means of a long needle, the cell was sealed and sample concentration was started. As concentration of the sample progressed, the filtrate was collected in a graduated cylinder. In this way, the volume of liquid remaining in the cell could be monitored. When the sample was concentrated to a volume of approximately 20 ml, enough DTRIS was added to make the final NaCl concentration 0.15 M. The sample was then removed from the cell and deposited in a septum stoppered bottle for storage.

The concentration procedure described above was adapted, as necessary , for the other sample concentrations performed during the purification of nitrogenase. For the concentration of component II, an Amicon UM20 membrane was employed.

G. Further Purification of Component I

Further purification of component I was effected by a second stepwise elution from a column of DEAE cellulose. A 20 cm X 2.5 cm column of DE-52 DEAE cellulose was equilibrated with 0.15 M NaCl DTRIS. The column was reduced by washing with 500 ml of 0.15 M NaCl DTRIS containing 1 mg/ml sodium dithionite followed by 100 ml of the same buffer containing 0.4 mg/ml sodium dithionite. The concentrated sample of AvI-1D was applied to the top of the column. The column was then washed with about 90 ml of 0.15 M NaCl DTRIS. When the main dark brown band was 3/4 of the way down the column bed, washing with 0.25 M NaCl DTRIS was started. A dark brown band developed and was collected anerobically as one fraction. This fraction will be referred to as AvI-2D.

H. Crystallization of Component I

Component I was crystallized out from the AvI-2D fraction. component I is quite soluble in cold 0.25 M NaCl DTRIS. The solubility of component I is at a minimum in warm 0.04 M NaCl DTRIS. Further decreases in the NaCl concentration result in an increase in the solubility of component I.[3]

The AvI-2D solution was concentrated in an Amicon cell to a total volume of 4 - 8 ml, or until the flow rate through the ultrafiltration cell was reduced by protein coating of the membrane. The solution was then diluted in the ultrafiltration cell by the addition of enough DTRIS to lower the NaCl concentration to 0.04 M. In a few minutes, a dense

growth of tiny crystals appeared in the ultrafiltration cell. The volume of the solution was reduced until coating of the membrane by a film of protein crystals restricted the flow of liquid through the membrane. The solution, whose volume was now 4 - 10 ml, was transferred to a hydrogen filled anerobic centrifuge tube. The centrifuge tube was then soaked in a 38 ^{o}C bath for one hour.

The crystals were collected by centrifugation in a room temperature centrifuge at 20,000 X g (17,000 rpm in the Sorvall SS-34 rotor) for 25 minutes. Centrifugation yielded a very dark brown, but not turbid, supernatant along with a black pellet covered by a thin layer of white material. After removal of the supernatant liquid, the pellet was broken up by means of a long needle stuck into the centrifuge tube. The pelleted material was resuspended in 3 volumes of room temperature 0.042 M NaCl DTRIS. A vortex mixer was used to effect complete disintegration of the pellet. After resuspension of the pellet, the liquid in the centrifuge tube was dirty brown in color and very turbid. The resuspension was centrifuged, again at room temperature, at 20,000 X g for 30 minutes. After centrifugation, the supernatant, which was transparent in appearance and pale brown in color, was removed. The pellet, which was black and covered with a thin layer of white material, was resuspended in 5 ml of ice cold 0.25 M NaCl DTRIS. As before, a long needle and a vortex mixer were used to disintegrate the pellet. The resuspension, which was dark brown in color, was cleared of debris by centrifugation at 20,000 X g for 20 minutes in a 0 ^{o}C centrifuge. After centrifugation, the transparent, dark brown supernatant was removed with a long needle and deposited in a septum stopppered bottle. The pellet consisted of the white material described earlier and some small black particles. It was

discarded. The bottle containing the supernatant was subjected to several cycles of evacuation and filling with argon. Unless the solution of component I was to be used immediately, it was frozen in the form of small pellets by dropping into liquid nitrogen. The pellets were stored in a liquid nitrogen freezer. Crystallized fractions of component I will be referred to as x-AvI.

I. Further Purification of Component II

Removal of the last traces of component I from the AvII-1D fraction was accomplished by a second stepwise elution from DEAE cellulose. A 20 cm X 2.5 cm column of DE-52 DEAE cellulose was prepared and reduced with 0.25 M NaCl DTRIS. The AvII-1D was concentrated to a final volume of 10 - 15 ml and then diluted to 0.25 M NaCl with DTRIS. The diluted AvII-1D was then applied to the top of the column and washed in with 90 ml of 0.25 M NaCl DTRIS. This was followed by washing with 0.35 M NaCl DTRIS. A gray - green band, closely followed by a brown band, developed at the 0.35 M front. The two bands were collected as one fraction. This fraction will be referred to as AvII-2D.

The 0.35 M NaCl concentration of the AvII-2D fraction was reduced by desalting on a column of Bio-Gel P-6. The inhibitory effect of high ionic strength on the rate of acetylene reduction by nitrogenase[6] makes the removal of NaCl desirable.

A 20 cm X 2.5 cm column was of Bio-Gel P-6 was prepared and reduced with 500 ml of DTRIS containing 1 mg/ml sodium dithionite. The AvII-2D was concentrated to 5 - 10 ml by ultrafiltration. After washing the Bio-Gel column with 100 ml of DTRIS containing 0.4 mg/ml sodium dithionite, the concentrated AvII-2D was loaded onto the column. The component II was eluted with DTRIS and collected anerobically. Collection

of the fraction was stopped after most of the dark green band had been eluted. Spot testing of the eluate for chloride with silver nitrate solution showed that the desalted AvII-2D solution was much less concentrated in chloride than was the origical sample. The collected fraction, which was referred to as AvII-2D-DES, was concentrated to a volume of 5 ml and stored frozen in liquid nitrogen.

J. Summary

Using the techniques described in the preceeding paragraphs, and starting with a good batch of Azotobacter cells, the experienced operator can obtain 100 - 150 mg of crystallized component I in 3 day's time. In table I, we show the results of a nitrogenase preparation where the specific activity and yield of component I were measured at each step in the procedure. In figure 2, we show the visible absorption spectrum of a solution of component I. The yield and specific activity of our preparation of component I are similar to those reported in the literature.[1] The visible wavelength absorption spectrum of our preparation of component I is identical to that reported in the literature.[1]

References

1. V.K. Shah and W.J. Brill; Biochem. Biophys. Acta(1973)305, 445 - 454.

2. S.A. Robrish and A.G. Marr; Bacteriol.(1962)83, 158 - 164.

3. V.K. Shah; personal communication.

Table I

Results of a Preparation of Component I from Azotobacter vinelandii

Fraction	Total Protein (mg)	Specific Activity	Yield = Specific Activity x Total Protein
Crude Extract	8979	41	368139
AvI-1D	990	321	317790
AvI-2D	435	811	353271*
x-AvI	134	1548	207060

* The yield of AvI-2D appears to be in excess of 100%. After this datum was obtained, it was found that the AvII used in the assay was contaminated with component I. This resulted in a spuriously high value of the specific activity of the AvI-2D fraction.

Appendix I

Flow Charts for the Purification of Nitrogenase

In the following pages, we present six flow charts which give a schematic representation of the nitrogenase purification procedure. The charts serve to illustrate the genealogies of the various fractions discussed in the description of the purification procedures. Some experimental details are given in the charts, allowing them to to be used as quick references during the actual performance of the purification sequence.

Chart A

Overall Scheme of Nitrogenase Purification Procedure

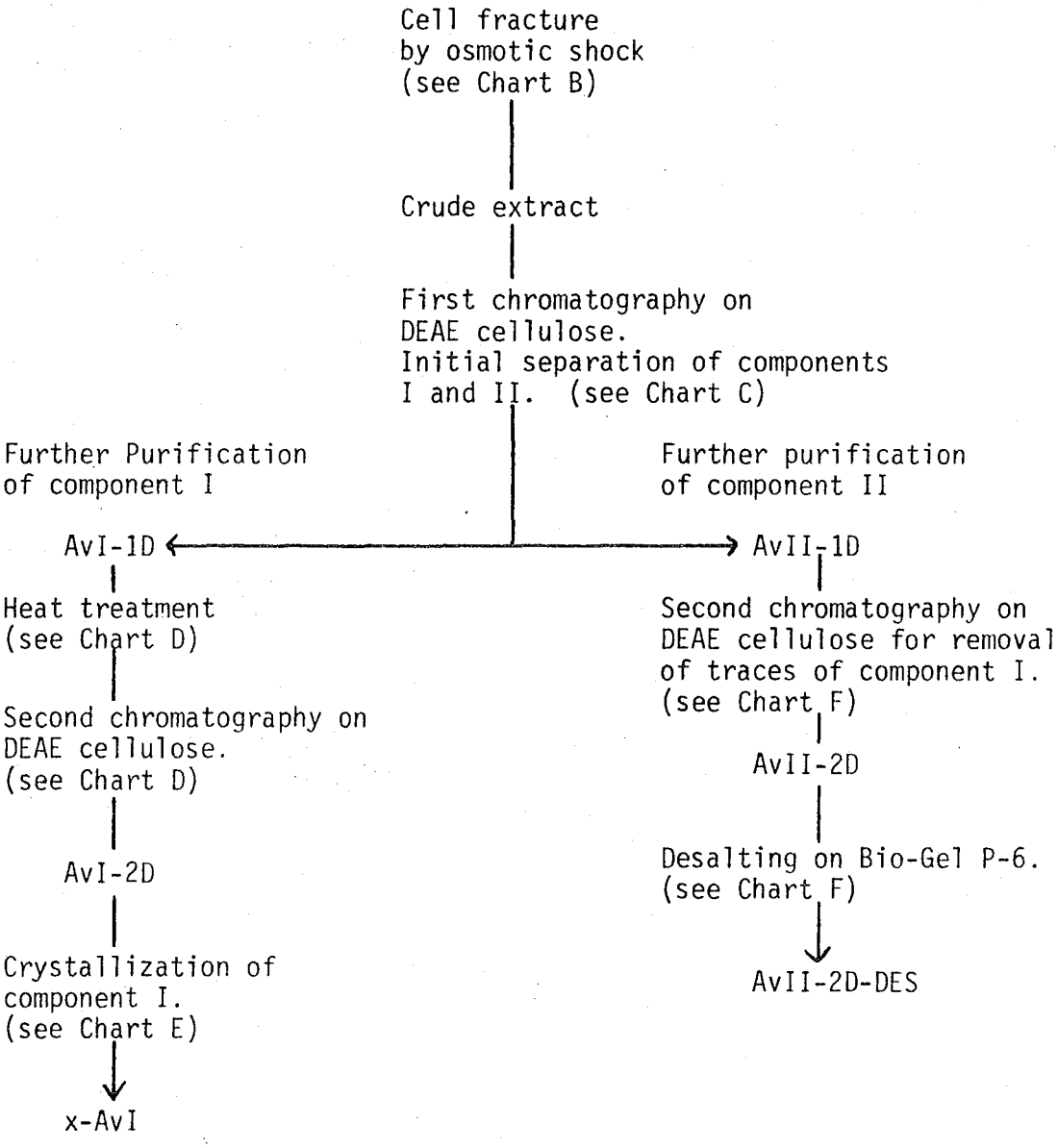

Chart B

Cell Fracture Procedure

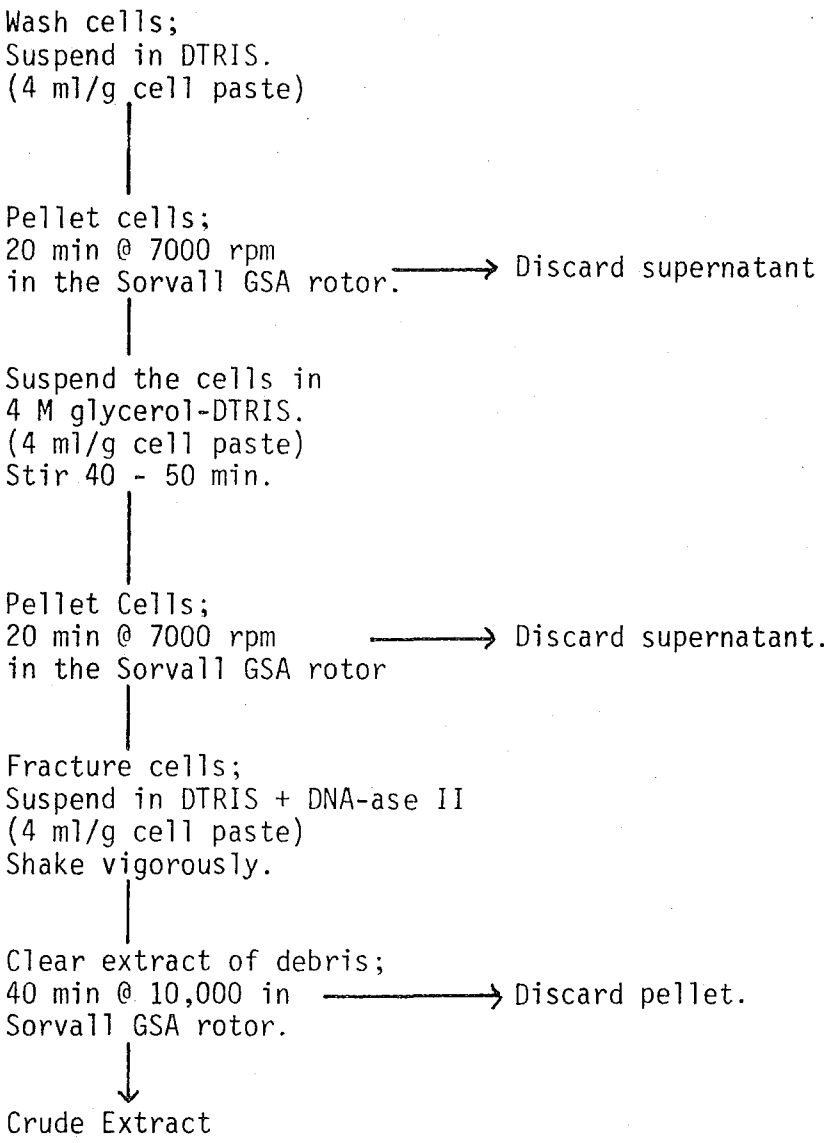

Chart C

First Chromatography Step

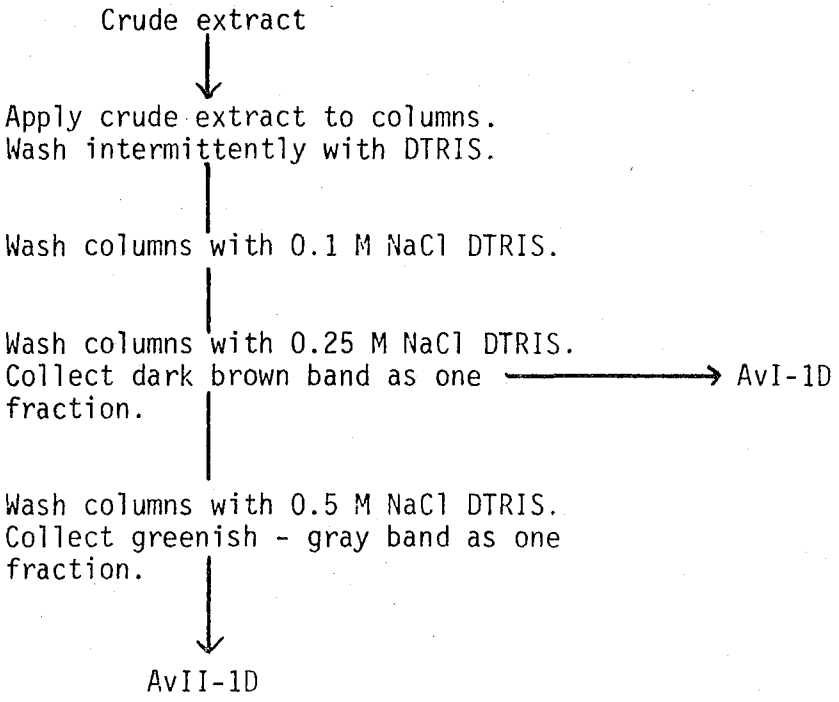

Chart D

Further Purification of Component I

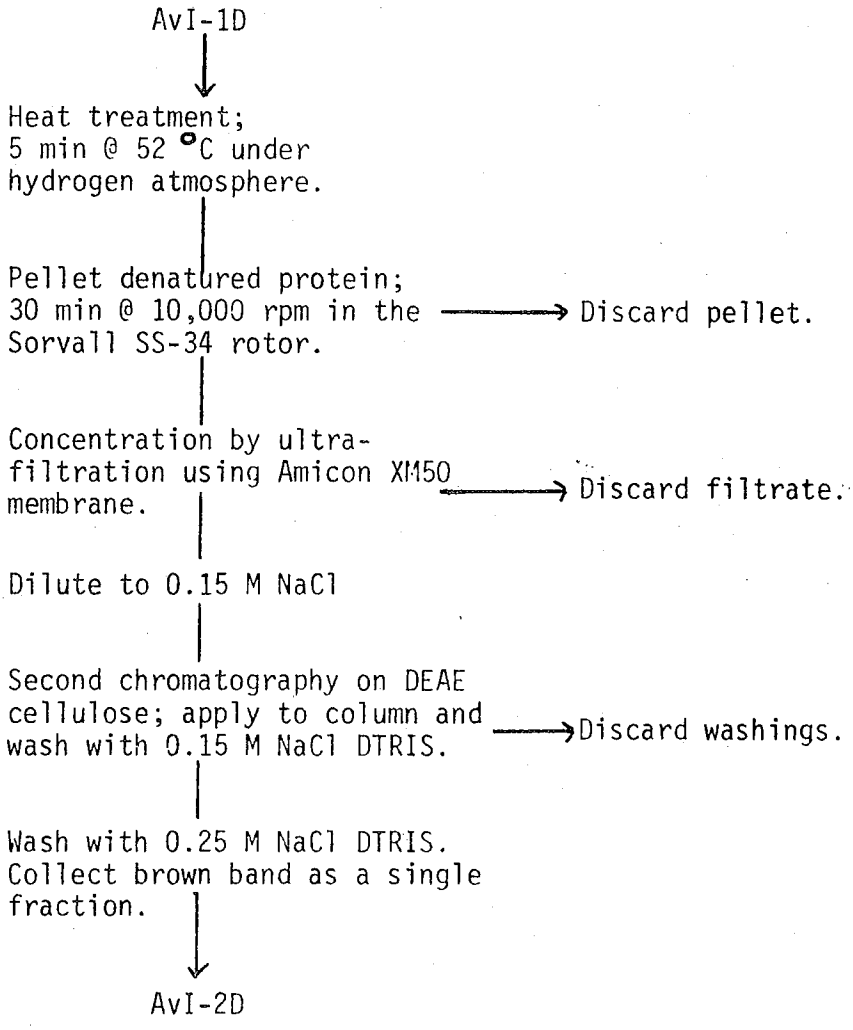

Chart E

Crystallization of Component I

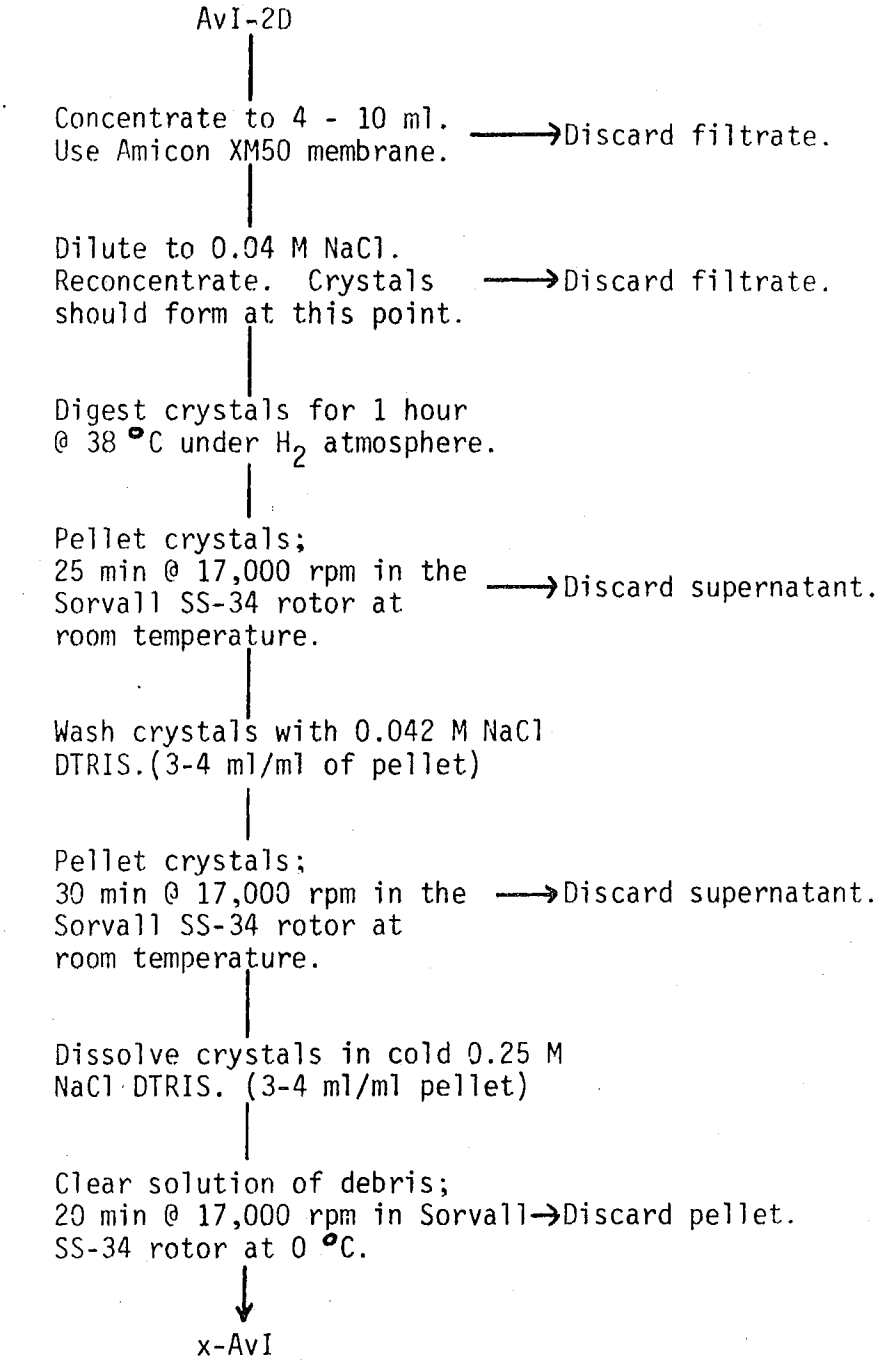

Chart F

Further Purification of Component II

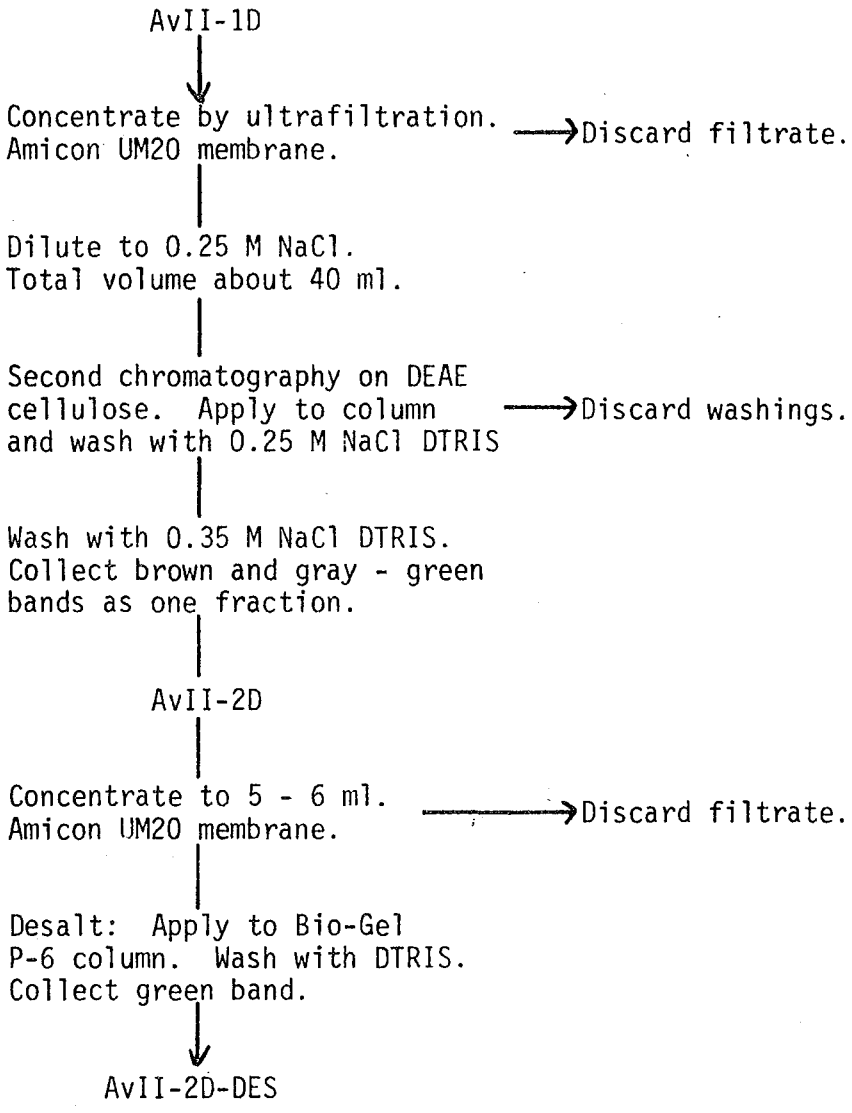

Figure Captions

1. Anerobic centrifuge tube used for small scale centrifugation. Design suggested by V.K. Shah.
2. Visible spectrum of a solution of crystallized Mo-Fe protein. Spectrum was taken at room temperature, protein concentration was equal to 1.6 mg/ml, buffer was 0.25 M NaCl 0.025 M Tris-HCl, pH 7.45.

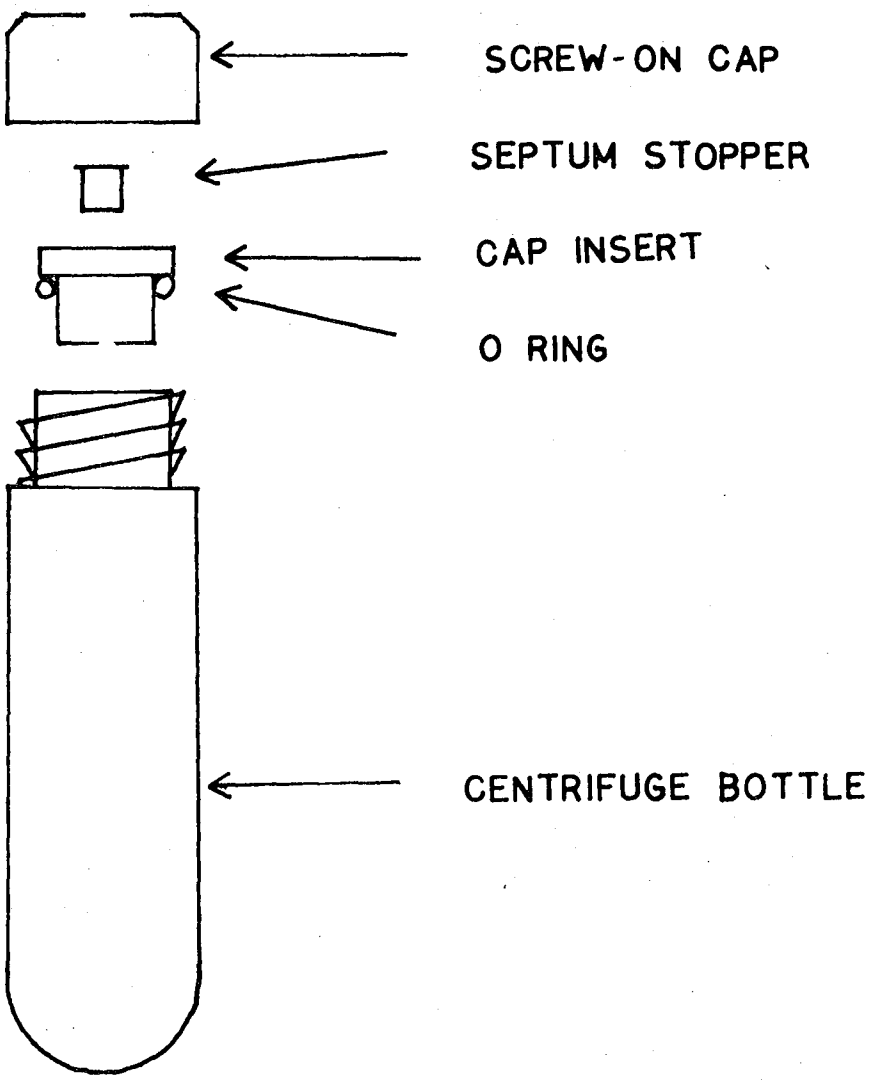

XBL 786 – 3999

Figure 1

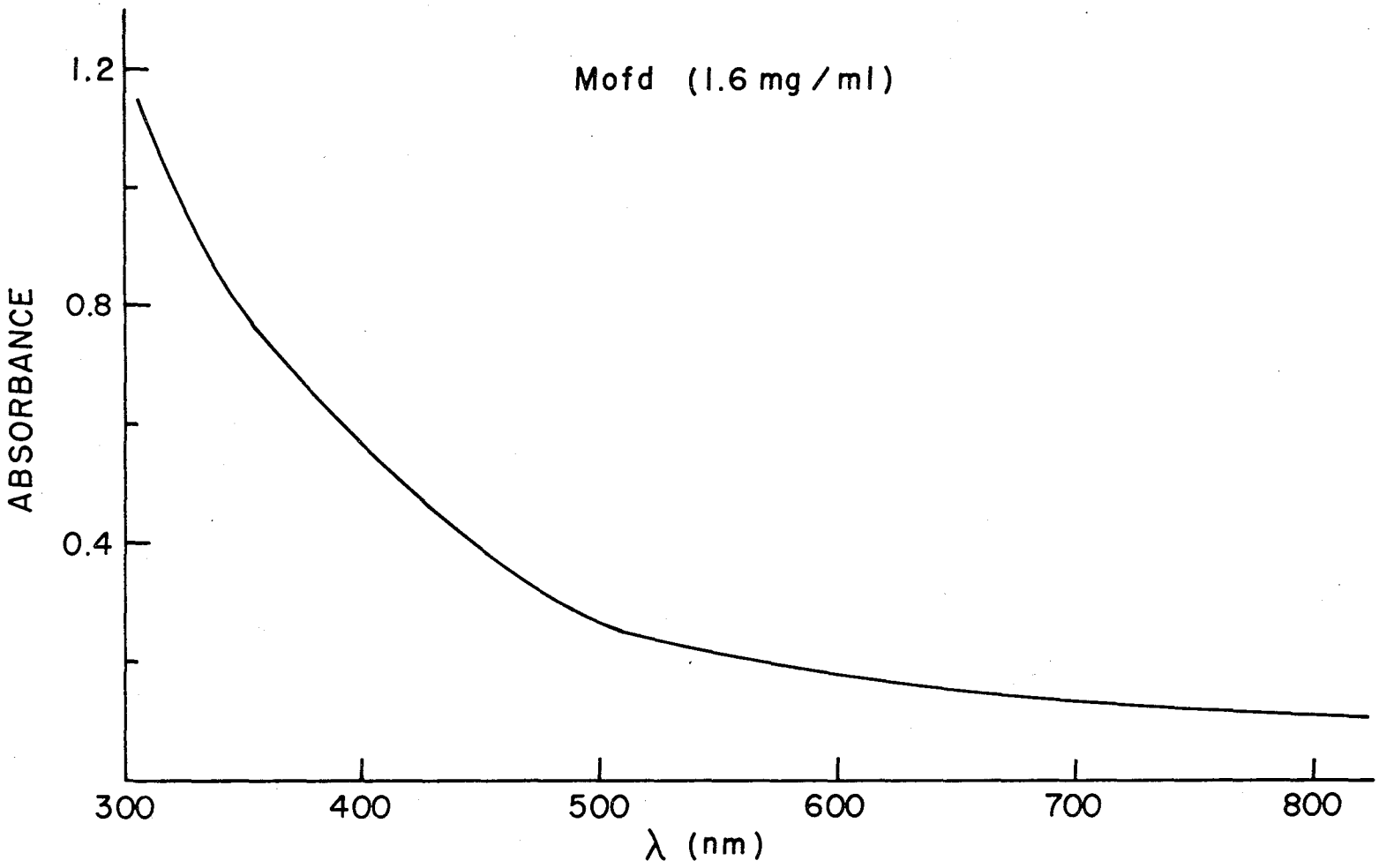

XBL755-5235

Figure 2

Chapter VIII

Nitrogenase Assay Techniques

The specific activity of the nitrogenase used in this work was determined by the acetylene reduction assay. The conditions used were similar to those reported by Shah, Brill and Davis[1]. In this chapter, the details of the assay procedures used will be described for the sake of completeness.

In addition to the presence of both nitrogenase components, the reduction of nitrogenase substrates will not occur without a suitable reductant, ATP and a divalent metal ion such as magnesium. Sodium dithionite has found wide application as a reductant for in vitro studies of nitrogenase [2]and was used exclusively in this work. During the turnover of nitrogenase, substrate quantities of ATP are converted into ADP. Since high levels of ATP and low levels of ADP inhibit nitrogenase reductions, an ATP generating system is commonly employed in order to maintain a constant, low level of ATP. In this work, a mixture of creatine phosphate, creatine phosphokinase, ATP and magnesium chloride was used as an ATP generator.

A. Equipment and Reagents

Acetylene reduction assays were carried out in micro - Fernbach flasks of 5 ml nominal volume. The actual stoppered dead volumes of the

flasks were determined individually. The dead volumes ranged from 5.5 to 7.4 ml. The flasks were permanently numbered for purposes of identification.

The standard assay reaction mixture had a total liquid volume of 1.0 ml and contained the indicated amounts of the following reagents: ATP, 2.5 micromoles; creatine phosphate, 30 micromoles; creatine phosphokinase, 0.1 - 0.2 mg; magnesium chloride, 5 micromoles; Tris-HCl (pH 7.4) 20 micromoles and sodium dithionite, 20 micromoles. All biochemicals were obtained from the Sigma Chemical Corporation. Inorganic salts were reagent grade chemicals.

Sodium dithionite was added to the reaction mixture as a 0.1 M solution prepared in 0.013 M NaOH. The solution was prepared by weighing out 348 mg of sodium dithionite into a septum stoppered bottle. 30 - 40 ml of 0.013 M NaOH solution were measured out into a second septum stoppered bottle. Both bottles were subjected to several cycles of evacuation and filling with oxygen free argon gas. Using a hypodermic needle and syringe, 20 ml of the NaOH solution were transferred into the bottle containing the sodium dithionite. The dithionite solution was prepared immediately prior to its use in the nitrogenase assay.

We found that it was convenient to prepare a stock solution containing all the ATP, magnesium chloride, creatine phosphate, creatine phosphokinase and buffer needed for the assay. This solution was referred to as the ATP generator or ATPg for short. The ATPg was prepared so that 0.2 ml of it would provide sufficient quantites of reagents for a total assay volume of 1.0 ml. The concentrations of the reagents in the ATPg are as follows: ATP, 0.0125 M; creatine phosphate, 0.15 M; creatine phosphokinase, 0.5 - 1.0 mg/ml; magnesium chloride,

0.025 M; Tris-HCl, 0.1 M; and bovine serum albumin, 1 mg/ml. Solids were dispensed gravimetrically using the water contents given by the manufacturer as a basis for the calculation of formula weights. Magnesium chloride was dispensed as a 1.0 M solution of $MgCl_2 \cdot 7H_2O$. Bovine serum albumin was added to prevent the denaturation of the creatine phosphokinase that, according to the manufacturer, occurs in solutions of low total protein concentration. In practice, ATPg was made up in 25 ml batches and stored frozen in 4 ml aliquots until needed.

To prepare the ATPg, the following procedure was employed. The magnesium chloride solution was added to the creatine phosphate solid, followed by the addition of the Tris-HCl as a 0.25 M solution of pH 7.8 - 7.9. The solid ATP, creatine phosphokinase and bovine serum albumin were then added to the creatine phosphate - magnesium chloride - buffer mixture. Distilled water was then added to dilute to the proper volume. When this procedure was followed, dilution of 0.2 ml of the ATPg to 1.0 ml with distilled water yielded a solution of pH 7.4 - 7.5.

Commercial welding acetylene was used without further purification. We found that commercial grade acetylene contains less ethylene than "reagent grade " acetylene. Acetylene was dispensed with a gas tight syringe from a water displacement reservoir. As a precaution against the contamination of the acetylene by small amounts of oxygen, the acetylene was added to the anerobic, dithionite containing assay mixture before enzyme components were added. The intial pressure of acetylene in the assay flasks was 0.06 - 0.08 atm.

For the measurement of the total protein concentration of nitrogenase preparations, the biuret reagent of Gornall was prepared.[3] For 1000 ml of the reagent, 31.2 g of NaOH was dissolved in 800 ml of water.

To this solution, 6.25 g of potassium sodium tartarate and 1.04 g of potassium iodide were added. The solution was then cooled to 4 C. 2.39 g of $CuSO_4 \cdot 5H_2O$ were added to the cooled solution which was then stirred overnight in a 4 C coldroom. After filtration through a fritted glass filter, the solution was diluted to 1000 ml. A biuret "blank" solution was prepared in the same fashion without any $CuSO_4 \cdot 5H_2O$.

B. Measurement of Total Protein Concentration

Total protein concentrations were determined by the biuret method of Gornall[3]. Bovine serum albumin (Sigma Chemical Corp., crystallized and lyophillized) was used as a protein standard. A 25 mg/ml solution of bovine serum albumin (BSA) was prepared gravimetrically in 0.025 M Tris-HCl at pH 7.45. The standard solution, which was stored in the refrigerator, had to be replaced periodically due to the formation of a white precipitate.

The biuret determination was carried out according to the following procedure. For the determination of crude extract protein, 4 BSA samples containing between 1 and 5 mg of protein were prepared. Samples of the crude extract (0.2 ml each) were prepared in duplicate. One of the crude extract samples was mixed with 5.0 ml of the biuret blank reagent. The remaining crude extract sample and and the standard samples were each mixed with 5.0 ml of the blue biuret reagent. After 15 minutes, the absorbance of the samples at 543 nm was measured using a Cary 14 spectrophotometer. A sample of the blue biuret reagent without any added protein was used as the reference solution for the samples that contained the blue biuret reagent. Water was used as the reference sample for the biuret blank sample. As a correction for the effects of any turbidity in the crude extract, the absorbance of the

biuret blank sample was subtracted from the absorbance of the unknown sample. After correction of the absorbance values for dilution, a calibration curve of standard sample absorbance versus amount of BSA in the standard samples was plotted. The amount of protein in the unknown sample was determined from the calibration curve. The determination of the protein concentrations of more highly purified samples of nitrogenase was carried out as described above, but with the use of smaller samples. Standard samples for these determinations typically contained between 0.2 and 2.0 mg of BSA. The more sensitive Cary 118 spectrophotometer was used to measure the smaller absorbances obtained in these determinations. It was not usually necessary to do a turbidity correction on purified samples of nitrogenase.

C. Conduct of the Nitrogenase Assay

The apparent specific activity of crude extracts of Azotobacter is dependent on the concentration of protein in the assay solution[1]. Above protein concentrations of 3.2 mg/ml, the rate of acetylene reduction is directly proportional to the protein concentration. Because of this effect, all assays of nitrogenase activity in Azotobacter crude extracts were carried out with a constant protein concentration of 3.2 mg/ml. As reported in this work, the specific activity of crude extract nitrogenase preparations is defined as the nanomoles of ethylene produced per minute per milligram of protein for an assay with a protein concentration of 3.2 mg/ml.

For preparations of isolated component I, the specific activity was determined by measuring the nanomoles of ehtylene produced per minute per milligram of component I protein in the presence of an excess of component II. In practice, the presence of an excess of component II

was verified by measuring the specific activity of component I for a range of several low concentrations of component I. For purified preparations of component I, we would typically run assays using between 20 and 200 micrograms of component I protein. If the measured specific activity of component I was independent of the component I concentration, an excess of component II was presumed to be present.

In the following paragraphs, the sequence of events occuring during the nitrogenase assay will be described. Typically, the first step was the preparation of a fresh, 0.1 M solution of sodium dithionite. ATPg (0.2 ml per flask) was then added to the required number of calibrated assay flasks. Distilled water was then added, as necessary, so that the final liquid volume of the assay mixture would be 1.0 ml. After being sealed with septum stopppers, the flasks were subjected to 10 cycles of evacuation and filling with oxygen free argon gas. Sodium dithionite solution (0.2 ml per flask) was then injected into each flask followed by the injection of 0.5 ml of acetylene.

Reactions were started in one of two ways, depending on the type of nitrogenase preparation being assayed. For crude extract assays, the prescribed volume of extract (containing 3.2 mg of crude protein) was injected with a small syringe. For assays of isolated nitrogenase components, the desired amount of component I was injected, and the reaction was started by the addition of component II. This procedure minimized any error caused by the possible contamination of the component II preparation with trace amounts of component I. Component I preparations were usually completely free of component II. After the addition of enzyme components to the assay flask, the pressure inside the flask was lowered to atmospheric pressure by briefly piercing the septum

with a hypodermic needle. At the desired time, the reaction was terminated by the injection of 0.1 ml of a 30% (w/v) solution of trichloroacetic acid.

D. Measurement of Ethylene Production

Ethylene produced during the nitrogenase assay was determined by gas chromatography. We employed a 100 cm long, 1/8 " od aluminum column containing Poropak T. The column was operated at 100 C with helium as the carrier gas. An air-hydrogen flame ionization detector was used for ethylene detection.

The output of the flame ionization detector was calibrated by measuring the response of the detector to the injection of various volumes of an air-ethylene mixture of known ethylene concentration. A dilute air-ethylene mixture was prepared by injecting 3.5 ml of a 10% ethylene - 90% argon standard mixture into a septum stoppered 60 ml bottle of known dead volume. The 60 ml bottle contained glass balls to facilitate the mixing of the gases by shaking. The mole fraction of ethylene in a typical dilute standard was 0.005. A sample calculation of the mole fraction of ethylene in the dilute standard is given in appendix I of this chapter.

Samples of the dilute ethylene standard, ranging in volume from 5 to 50 microliters, were injected by means of a gas tight syringe. The ethylene peak heights were plotted as a function of the number of nanomoles of ethylene injected. The output of the detector was found to be linear for injection containing between 2 and 9 nanomoles of ethylene.

The volumes of the gas samples taken from the assay flasks were adjusted so that the ethylene peak heights obtained fell within the range

spanned by the peak heights of the injected standards. The number of nanomoles of ethylene injected was determined from the calibration curve. The specific activity of the nitrogenase was calculated with the following formula.

$$\text{SPECIFIC ACTIVITY} = \frac{N_{inj}(V_d - V_l)}{V_{inj} * C_p * V_p * t_a}$$

N_{inj} = nanomoles C_2H_4 injected into the gas chromatograph

V_d = stoppered dead volume of the assay flask(ml)

V_l = liquid volume of the assay mixture (ml)

V_{inj} = volume of the gas sample injected into the gas chromatograph(ml)

C_p = protein concentration of the sample being assayed(mg/ml)

V_p = volume of the protein sample used in the assay(ml)

t_a = time elapsed during the assay reaction(min)

References

1. V.K. Shah, L.C. Davis and W.J. Brill; Biochem. Biophys. Acta(1972) 256, 498 - 511.

2. W.A. Bulen, R.C. Burns and J.R. LeComte; Proc. Nat'l. Acad. Sci. - USA(1965)53, 532 - 536.

3. A.G. Gornall, C.J. Barawill and M.M. David; J. Biol. Chem.(1949)177, 751 - 756.

Appendix I

Calculations for Dilution of Ethylene

The 10 % ethylene - 90 % argon mixture was dispensed from a water displacement bulb with h_w mm of hydrostatic head. To calculate the number of nanomoles of ethylene injected per microliter of dilute standard, the following formulae were used.

Total pressure in the water displacement bulb : $P_t = P_a + h_w/13.54$

Pressure of dry gas in the bulb : $P_g = P_t - P_w$

Mole fraction of C_2H_4 in the bulb : $X_b = 0.10(P_g/P_t)$

Mole fraction of C_2H_4 in the standard bottle : $X_s = \frac{V_i X_b}{V_i + V_b}$

Moles of ethylene injected per microliter of diluted standard :

$$n = \frac{(P_a/760)X_s * 10^{-6}}{0.08205 * T_r}$$

P_t = Total pressure inside the gas displacement bulb (mm Hg)

P_a = atmospheric pressure (mm Hg)

h_w = Height of water column above gas in water displacement bulb (mm)

P_w = Vapor pressure of water at T_r K

X_b = Mole fraction of C_2H_4 in the water displacement bulb

X_s = Mole fraction of C_2H_4 in the diluted standard

V_i = Volume of 10 % C_2H_4 injected into dilute standard bottle (ml)

V_b = Dead volume of the bottle used for making dilute standard(ml)

T_r = Temperature of the room (K)

TECHNICAL INFORMATION DEPARTMENT
LAWRENCE BERKELEY LABORATORY
UNIVERSITY OF CALIFORNIA
BERKELEY, CALIFORNIA 94720